Directed Transport of Superparamagnetic Microbeads

Using Periodic Magnetically Textured Substrates

by

Minae Ouk

B. S., Pohang University of Science and Technology (2009)

M.S., Pohang University of Science and Technology (2011)

Submitted to the Department of Materials Science and Engineering

in partial fulfillment of the requirements for the degree of

Doctor of Philosophy in Materials Science and Engineering
at the
MASSACHUSETTS INSTITUTE OF TECHNOLOGY

June 2017

Signature redacted

Author.....

Department of Materials Science and Engineering

May 17, 2017

Signature redacted

Certified by..... .....

Geoffrey S. D. Beach

Class of 58 Associate Professor of Materials Science and Engineering

Thesis Supervisor

Signature redacted

Accepted by..... ....

Donald R. Sadoway

Chair, Department Committee on Graduate Studies

Directed Transport of Superparamagnetic Microbeads Using Periodic Magnetically Textured Substrates

by

Minae Ouk

Submitted to the Department of Materials Science and Engineering
on May 17th, 2017, in partial fulfillment of
the requirements for the degree of
Doctor of Philosophy in Materials Science and Engineering

Abstract

Superparamagnetic microbeads (SPBs) have been widely used to capture and manipulate biological entities in a fluid environment. Chip-based magnetic actuation provides a means to transport SPBs in lab-on-a-chip technologies. This is usually accomplished using the stray magnetic field from patterned magnetic micro structures or domain walls in magnetic nanowires. Recently, many studies have focused on sub-micron sized antidot array of magnetic materials because non-magnetic holes affect the micromagnetic properties of film. In this work, a method is presented for directed transport of SPBs on magnetic antidot patterned substrates by applying a rotating elliptical magnetic field. We find a critical frequency for transport beyond which the bead dynamics transition from stepwise locomotion to local oscillation. We also find that the out-of-plane (H_{OOP}) and in-plane (H_{IP}) field magnitudes play crucial roles in triggering bead movements. Namely, we find threshold values in H_{OOP} and H_{IP} that depend on bead size which can be used to independently and remotely to address specific bead populations in a multi-bead mixture. In addition, these behaviors are explained in terms of the dynamic potential energy landscapes computed from micromagnetic simulations of the substrate magnetization configuration. Furthermore, we show that large-area magnetic patterns suitable for particle transport and sorting can be fabricated through a self-assembly lithography technique, which provides a simple, cost-effective means to integrate magnetic actuation into microfluidic systems. Finally, we observed the transport of bead motion on antidot arrays of multilayered structures with perpendicular magnetic anisotropy (PMA), and found that the dynamics of SPBs on a PMA substrate are much faster than on a substrate with in-plane magnetic anisotropy (IMA). Our findings provide new insights into the enhanced transport of SPBs using PMA substrates and offer flexibility in device applications using the transportation or sorting of magnetic particles.

Thesis Supervisor: Geoffrey S. D. Beach

Title: Class of'58 Career Development Associate Professor

Acknowledgements

Of all parts of this thesis, writing this section is the hardest and most exciting part for me because it makes me recall everything since I came to Boston. Through this, I would like to thank all the people who have been here for me during my Ph.D. programs. As you know, the Ph.D. program was challenging, including demanding course work and the solving of problems in a creative and scientific way. In addition, studying at MIT has been a matter of survival for me at every step, and an emotional test. I definitely could not have succeeded in life at MIT without significant help from the following people.

First, I would like to appreciate my advisor, Professor Geoffrey Beach. He is a great advisor and I respect him as a teacher and person. When I was in trouble and I wanted to give up, he always understood my situation and cheered me up with his wisdom. I sincerely appreciate that he did not give up on me and guided me with patience. In addition, he listened to and answered all of my questions and gave a lot of guidance. He always made me excited about the research and showed me his enthusiasm as a researcher. Therefore, I wholeheartedly thank Prof. Geoffrey Beach for supporting me, working with me, and for many discussions.

I also would like to thank my other thesis committee professors, Professor Caroline Ross and Professor Alfredo Alexander-Katz. To Professor Caroline Ross, I learned the fundamental knowledge of magnetism through your classes. Furthermore, every committee meeting, you advised, taught, and gave me the right direction to move forward. I sincerely thank you so much for your time, suggestions, and enthusiasm for my research. To Professor Alfredo Alexander-Katz, I thank you for all your guidance for modeling and studying the simulation. Before I met Professor

Katz, I did not know MATLAB at all and struggled moving forward. You taught me in a collegial way and inspired me with your patience. I extremely appreciate your time, advice, and guidance.

To my family in Korea, I am such a lucky girl to have my great father, mother and sister. They have always believed in my choices and supported me. Even though I could not live together with my family after graduating from high school, they have been my best support and motivation to overcome the difficulties of at MIT. I sincerely thank you all for visiting Boston to cheer me up and help me when I was stressed. My family members always said to me "You are still my proud and lovely daughter and it does not matter whether you receive the Ph. D degree or not", and this long-lasting love and belief helped calm me down.

As for the Beach group members, I found the most amazing and nicest people I have ever met. Satoru, Liz, Uwe, and Seong-hoon, taught me about our lab facilities and helped me develop experiments. In addition, I also would like to offer thanks to the other members of the Beach Lab: Kohei, Felix, Can, Parnika, Sarah, Lucas, Max, AJ, Ivan, Mantao, and Sasha. Due to these wonderful labmates, I was able to learn and obtain a great deal of knowledge and ideas from discussions with you about my research, and I sincerely thank you for all your help in experiments. Beyond the research, you all made my time at MIT special and enjoyable.

Finally, I especially thank my friends (Namjoo, Siwon, Jiyoung, Kyoung-won, Sarah, So-young, Shin young, Ji-yeon, Jeong-yun, Kyung-hee, Jessie, Sangwon, Yongjoo, E.K, Intak, Byungjin, Eugene, Jong-won, Dong-wook) in Boston and (Miri, Ja-yu, Myeong-won, Ul-won, Ji-seon, friends of 2 bunban) in Korea. I will never forget any of my friends and every moment in my Ph.D. journey.

Contents

List of Figures

List of Frequently Used Symbols

α	Damping parameter
B_r	Residual induction
B_s	Saturation induction
Co	Cobalt
DW	Domain wall
d	Diameter of the SPBs
FACS	Fluorescence-activated cell-sorting
f	rotational frequency
f_c	Critical frequency
H_c	Coercivity
H_{eff}	total effective field
H_{IP}	Out-of-plane field
H_{OOP}	In-plane field
hcp	hexagonal-close-packed
HMDS	hexamethyldisilzane
K	uniaxial magnetic anisotropy constant
K_{eff}	Effective anisotropy constant
γ	Gyromagnetic ratio
M	Volumetric magnetization
MFM	Magnetic force microscope

MS	magnetostatic energy
M_s	Saturation magnetization
M_r/M_s	Squareness
ncp	monolayers and non-close-packed
OOMMF	Object-oriented micro-magnetic framework
PDMS	Polydimethylisiloxane
p	distance from center to center or periodicity
PMA	Perpendicular magnetic anisotropy
RIE	Reactive ion etching
SEM	Scanning electron microscope
SPB	Superparamagnetic bead
SPBs	Superparamagnetic beads
T_N	Neel temperature
T_B	Blocking temperature
τ_m	Measurement time
v	velocity of SPBs
V_m	volume of the SPBs or particle
VSM	Vibrating sample magnetometer

Chapter 1

Introduction

In this chapter, we motivate the importance of studying the interaction between superparamagnetic beads (SPBs) and periodic magnetic patterns for the dynamics of SPBs. Then, we briefly review the outline of the thesis.

1.1 Motivation

Micrometer- or nanometer- sized devices for medical or biological applications have been widely studied during recent decades. The goal of most such research is to create fast, cheap, sensitive, and high-throughput platforms, and these are called "lab-on-a-chip" technologies in analysis systems.

The key technologies of lab-on-a-chip are transporting biological species across the surface of the chip, which can be controlled by simple or remote methods. Surface-functionalized micrometer- or nanometer- sized beads are popular ways to transport biological species. Taking advantage of the small diameter of the beads, options for surface modification, and actuation modes. In fluidic environments, beads with biological matter can be transported, controlled, and manipulated. Therefore, techniques based on beads open the possibility of future biological applications such as drug delivery, hyperthermia, and MRI enhancement, which can be based on acoustofluidics,[1-8] optical images,[9-15] hydrodynamics,[16-21] thermophoresis,[22] electrophoresis,[23-26] dielectrophoresis,[27-31] and magnetic force.[32-46]

Magnetic systems inducing bead motion have many advantages. Magnetic particles or entities can be manipulated using discrete permanent magnets or electromagnets, independent of normal microfluidic or biological processes.[47-48] Furthermore, such magnetic systems do not need complex experimental components such as micro channels, electrical connections, pumps for fluid flow, reservoir chambers.[49] Localized heating is known to cause problems in lab-on-a-chip devices, but magnetic fields do not degrade biological entities and are thermally stabilized,[50-51] unlike electric fields.[52-53] Furthermore, magnetically activated cell-sorting can be possible simultaneously, offering high throughput, while fluorescence-activated cell-sorting (FACS) which is a sequential process[43].

In recent decades, nano- or microsized SPBs with functionalized surfaces have been widely applied in biological analysis applications using transport, switching, mixing, separation, and detection. Initial on-chip bead manipulation studies were based on bulky permanent magnets in fluidic microchannels[54-59]. The simplicity of this system is attractive, but the formation of SPB aggregation leads to attenuated optical signals and mechanically damages the biological cells. Electromagnets that are located in microchannel have also been used for magnetic manipulation. In these structures, the magnetic field gradient usually produce 10^4-10^5 Tm^{-1} in a local regime, which sufficiently supports the transport of SPBs. Several designs, including current-carrying wires[60-62], high aspect ratio trenches[63-64], and several arrays of coiled wire[65] have been developed to precisely control SPBs. However, these electromagnets within microchannel have limitations in terms of the complexity of fabrication, a nonlinear position dependence of the force profile, and heating problems from the large number of electromagnets.

We focus on the manipulation of SPBs on micro-magnets by rotating magnetic fields. Several mechanisms cause bead transport: demagnetization of a soft magnetic substrate, domain

wall magnetophoretic transport, and nonlinear magnetophoresis. In the first, the SPBs are transported on de-magnetizable structures such as $Ni_{0.8}Fe_{0.2}$[66]. By applying a rotating magnetic field in the *xy* plane, the soft micro-magnets are easily demagnetized and the magnetizations of micro-magnet elements are changed along each direction of the magnetic field. The SPBs follow the net magnetization of the magnetic structure and are transported along the perimeter of the micro-magnet elements such as ellipses[66-68], connected disks or half-disks[69-73], triangles[49,74], and other complex configurations[75]. In the case of symmetric elements, such as disks, H_z is required to move the SPBs from one element to another; otherwise, the SPBs exhibit a closed orbit around the element.

In the second mechanism, using the stray field from the domain walls in thin films has been used to control the movement of SPBs. For example, in a thin film of $Y_{2.5}Bi_{0.5}Fe_{5-q}Ga_qO_{12}$ [76-79], magnetic domains are configured in a stripe-pattern with periodicity λ, and the travelling distance of SPBs on this film is λ for a rotational period. In continuous films, applying a high-frequency magnetic field with pulses can create "bubble" domains[78, 80-81], which trap the SPBs. The transport of SPBs is controlled through the magnitude of the normal field component H_z. Furthermore, the transport of beads on patterned zigzag nanowire has been widely studied with head-head (HH) and tail-tail (TT) domains at the vertices of the wire[82-87]. The domain walls with SPBs were shifted by applying H_{xy} and H_z magnetic fields, the latter of which controls the depth of the potential well. The geometry of domain wall conduits also includes ring, square, or rectilinear conduits, where the SPBs can be smoothly transported using an H_{xy} field[33,34,84-85,88-90].

The final mechanism for SPB transport is based on nonlinear magnetophoresis using hard micro-magnet arrays. A traveling magnetic field wave, which results from the superposition of an out-of-plane rotating field and stray field from an array of circular micro-magnets, transports the

SPBs[36-37, 91-92]. The velocity of SPBs increases linearly with the frequency of the rotating field until a critical frequency (ω_c), beyond which the velocity rapidly drop-off and the SPBs locally oscillate. Using the dependency on the ω_c, multiplex separation is possible for a heterogeneous sample. However, the separation efficiency is limited by the sharpness in the transition from "mobile" to "immobile" beads, which is influenced by the ratio of the diameter of SPBs and the periodicity of patterns.

In this thesis, for the first time, the dynamics of SPB transport on antidot arrays is fully investigated and characterized. Whereas previous studies have focused on the critical frequency to sort the SPBs, we explore the dynamics of SPBs and elucidate the interaction between the SPBs and various magnetic patterns. Through several micro-magnet structures with different magnetic anisotropy and geometry, we show different behaviors of SPB transport. Thus, we not only demonstrate the controlling parameters such as the critical frequency as well as the threshold behavior in a magnetic field, but also show magnetic potential distribution to play a key role to understand the dynamics of SPBs. Finally, with this knowledge, we design a multilayer structure with which we are able to enhance the dynamics and flexibility of SPB transport.

1.2 Thesis outline

Given the advantages of micro-magnetic lab-on-a-chip technologies, the aim of this thesis is to develop several parameters to precisely control SPB transport and establish micro-magnetic arrays to enhance the dynamics of SPBs, including capture, transport, and sorting. Accordingly, the thesis is organized as follows:

- Chapter 2 discusses the physical phenomena and fundamental concepts needed to support this inquiry: magnetic energy, magnetic anisotropy, domain walls, and superparamagnetism.

- Chapter 3 explains the simulation and fabrication methods that are used in this thesis.

- Chapter 4 demonstrates that the dynamics of the SPBs can be controlled by the critical frequency as well as the threshold behavior in magnetic fields. These controlling parameters depend on the patterns of the magnetic configurations or lattice geometry.

- Chapter 5 reveals that bead sorting based on these controlling parameters can be achieved throughout the entire range of micro-magnet arrays. We introduce self-assembly methods, which are simple and cheap ways to produce small-scale micro-magnet arrays.

- Chapter 6 demonstrates the enhanced dynamics of SPB motions on the perpendicular magnetic anisotropy substrate and the widened scope of the capability of magnetic fields to transport SPBs. We also explain the different transport of SPBs on various lattice geometries through simulation results.

- Chapter 7 summarizes the findings in this thesis and discusses prospects for the future.

Chapter 2

Background

In this chapter, we discuss the fundamental phenomena relevant to developing a magnetic lab-on-a-chip. First, we describe the details of the magnetic concept, including magnetic anisotropy and superparamagnetic beads. After that, we will discuss magnetotransport, which will become important in later chapters for understanding the mechanism of bead transport.

2.1 Basic concepts

2.1.1 M-H curves

When a magnetic field of strength **H** is applied to a material, the response of the material is called magnetic induction **B**. All the individual atomic moments in the materials will contribute to the response, and the relation between **B** and **H** is proportional to the material properties. Generally, the equation relating **B** and **H** is given by:

$$\boldsymbol{B} = \mu_0(\mathbf{H} + \mathbf{M}) \tag{1}$$

where μ_0 is the permeability of free space, and **M** is magnetization, defined as the magnetic moment per unit volume **M**= m/V, where m is the magnetic moment on a volume V of the material.

Furthermore, the magnetic properties of materials are defined not only by the magnetization, but also by the magnetic susceptibility, which varies with the applied magnetic field. The magnetic susceptibility is the ratio of **M** to **H**, where the magnetization induced in a material by **H**[93]:

$$\chi = \frac{\boldsymbol{M}}{\boldsymbol{H}} \tag{2}$$

where χ is dimensionless and both **M** and **H** are expressed in Am^{-1}. Most materials can be classified either as paramagnets, for which χ falls in the range 10^{-6}-10^{-1}, or diamagnets, where χ is in the range -10^{-6} to -10^{-3}. However, some materials exhibit ordered magnetic states without applying a field; these materials are classified as ferromagnets, ferrimagnets, or antiferromagnets. The coupling interaction between the electrons within the materials leads to spontaneous magnetization and exhibits different ordering based on the nature of the coupling interaction. The susceptibility in ordered material depends on temperature as well as on **H**. Therefore, each material exhibits the characteristic sigmoidal shape of the **M-H** curves when a large value of **H** is applied. In ferromagnet and ferrimagnet materials, the **M-H** curves show hysteresis, which is an irreversible magnetization process due to the pinning of magnetic domain walls at grain boundaries or impurities as well as to intrinsic properties such as the crystalline magnetic anisotropy.

Figure 2-1 describes the typical hysteresis loop for the ferri- or ferromagnet, plotted **B** versus **H**. The loop started at the original, unmagnetized state, and **B** follows the curve from 0 to $\mathbf{B_s}$, which is the saturation induction. Here, we note that although the magnetization is constant after saturation, **B** continually increases due to $\mathbf{B} = \mu_0(\mathbf{H} + \mathbf{M})$. When **H** is reduced to zero after saturation, **B** reduces from $\mathbf{B_s}$ to $\mathbf{B_r}$ (remanence induction), and the reversal field required to reduce **B** to zero is called the coercivity $\boldsymbol{H_c}$.

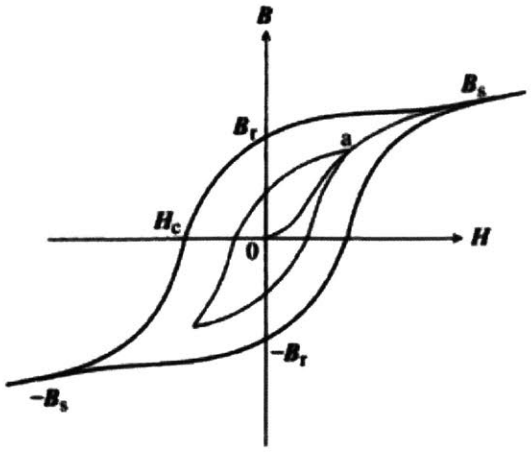

Figure 2-1 Hysteresis loop for ferrimagnet or ferrromagnet. From Nicola A. Spaldin, *Magnetic Materials: Fundamentals and Device Applications*, (Cambridge University Press, 2003)

2.1.2 Magnetic energy

In this section we discuss several magnetic energy terms used in micro-magnetics, which describe magnetic behavior at sub-micrometer length scales. To determine the spatial distribution of the magnetization **M** at equilibrium, the magnetic energy, including exchange, anisotropy, Zeeman, and magnetostatic energy, should be minimized.

The exchange energy is based on the quantum-mechanical exchange interaction and is defined as[94]:

$$E_{ex} = A\left(\frac{\partial\theta}{\partial x}\right)^2 \tag{3}$$

where A $= s^2 a^2 \mathcal{J}_{ij} N_v'/2$ is called the exchange stiffness constant, a is lattice constant, $\mathcal{J}_{ij}$ is exchange integral, s^2 is the square of spin, and N_v' is the number of nearest-neighbor atoms per unit volume and a is the lattice parameter. This energy increases with increasing angular

divergence $\frac{\partial\theta}{\partial x}$ and exchange stiffness A. Therefore, exchange energy tends to keep adjacent magnetic moments aligned in parallel or antiparallel, producing antiferromagnetism, ferrimagnetism, and ferromagnetism. For example, it is responsible for ferromagnetic behavior, where the magnetization retains a parallel direction at saturation.

Anisotropy energy represents the directionality dependence for spins to align along a certain direction. Considering the magnetocrystalline anisotropy in the uniaxial case, this is given as[94]:

$$u_a = \sum_n K_{un} sin^{2n}\theta \tag{4}$$

where u_a is the uniaxial crystal anisotropy energy density, K_{un} is the uniaxial anisotropy constant, and θ is the angle between the spin and the preferred direction.

The Zeeman energy is due to the misalignment of the magnetization in an applied field, and is described as[94]:

$$u_H = -\mu_0 M_s \cdot H_0 = -\mu_0 M_s H_0 cos\theta \tag{5}$$

where θ is the angle between the magnetization **M** and field **H**. This energy decreases as the angle θ decreases.

Finally, the magnetostatic energy is created by the magnetic sample itself and arises mainly from having a discontinuity in the normal component of magnetization across an interface. The energy results from the interaction between the spin and the dipolar demagnetization field, which is the field inside the sample. It points along the opposite direction to the magnetization. Therefore, the magnetostatic energy is an anisotropic energy that depends strongly on the shape of the samples. The magnetostatic energy is defined as[94]:

$$u_{ms} = -\mu_0 M \cdot H_i = -\mu_0 M_s H_i cos\theta \quad (6)$$

where M_s is the saturation magnetization of the material, and the internal field $H_i = H_{appl}+H_d$ is a function of the externally applied field H_{appl} and the dipolar demagnetizing field H_d. Therefore, the demagnetization field contributes to decreasing the magnetostatic energy. In addition, as the angle θ between the direction of magnetization and the direction of internal field increases, the magnetostatic energy also increases.

Here, we note that the exchange and magnetostatic energy contribute in opposite ways, where the exchange energy favors parallel spin alignments, and the magnetostatic energy prefer antiparallel alignment. Therefore, the extent l over which energy dominates is characterized by the exchange length, and it varies with the type of domain wall[95]. For hard materials with large crystalline anisotropy, the typical domain wall is the Bloch type. In that case the width of the Bloch wall is $\delta_B = \pi\sqrt{A/K_u}$, where A is the exchange constant in J/m and K_u is the uniaxial anisotropy constant in J/m^3. The magnetocrystalline exchange length l is defined as $\sqrt{A/K_u}$ in the hard materials; while in very thin films, composed of magnetically soft materials, A Neel wall is the typical structure. The width of these walls is around $3\sqrt{A/K_d}$, where $K_d = \mu_0 M_s^2/2$ and the magnetostatic exchange length is:

$$l_{ex} = \sqrt{2A/(\mu_0 M_s^2)} \quad (7)$$

In this case, the exchange interaction is dominant when $l < l_{ex}$ while the magnetostatic interaction is dominant when $l > l_{ex}$.

2.1.3 Magnetic anisotropy

Magnetic anisotropy is the preference for the magnetization to lie in a certain direction in the samples. Magnetic anisotropy has several origins including shape anisotropy, magnetocrystalline anisotropy, magnetoelastic anisotropy, and exchange anisotropy.

Magnetocrystalline anisotropy is a force which hold the magnetization in certain crystallographic directions in a crystal[96]. The crystal anisotropy energy in a cubic lattice, which is the energy needed to align magnetization along a non-easy direction, can be expressed as:

$$E = K_0 + K_1(\alpha_1^2\alpha_2^2 + \alpha_2^2\alpha_3^2 + \alpha_3^2\alpha_1^2) + K_2(\alpha_1^2\alpha_2^2\alpha_3^2) + \cdots \quad (8)$$

where K_0, K_1, $K2$,.. are the constants for particular materials and $\alpha_1, \alpha_2, \alpha_3$ are the cosines of the angles between M_s and crystal axes. Usually K_0 is ignored because it is not changed by the angle, and the values of both K_1 and K_2 determine the direction of easy and hard magnetization. For hexagonal crystals, all directions in the basal planes are hard axes and the magnetocrystalline anisotropy energy depends on only a single angle, θ, between the M_s vector and the c axis. In this case, the anisotropy can be described as:

$$E = K_0' + K_1'cos^2\theta + K_2'cos^4\theta + \cdots = K_0 + K_1sin^2\theta + K_2sin^4\theta + \cdots \quad (9)$$

The physical origin of magnetocrystalline anisotropy is spin-orbit coupling. When the external field tries to reorient the spin of an electron, then the orbit of that electron also tends to be reoriented. However, the orbit is also strongly coupled to the lattice, so energy is required to overcome the resistance. This energy can be measured by several methods, including torque curves, torsion pendulum, magnetization curves, and magnetic resonance.

The shape anisotropy is dependent upon the shape of the sample. As mentioned in Section 2.1.2, the demagnetizing field along a short axis is stronger than along a long axis. When a field is applied along a short axis, the same field is produced inside the specimen. Therefore, the shape itself can be a source of magnetic anisotropy. Considering a prolate spheroid with semi-major axis c and semi-minor axes a of equal length, as shown in Figure 2-2, the magnetostatic energy is defined as[96]:

$$E_{ms} = \frac{1}{2}[(Mcos\theta)^2 N_c + (Msin\theta)^2 N_a] \tag{10}$$

where N_c and N_a are demagnetizing coefficients along c and a, respectively. Substituting $cos^2\theta = 1 - sin^2\theta$, then the above equation is expressed as:

$$E_{ms} = \frac{1}{2}M^2 N_c + \frac{1}{2}(N_a - N_c)M^2 sin^2\theta \tag{11}$$

In this magnetostatic energy expression, it has the same form as uniaxial crystal anisotropy energy, an angle-dependent term, and the long axis of the sample plays the same role as the easy axis of the crystal. Thus, the shape-anisotropy constant K_s is given by:

$$K_s = \frac{1}{2}(N_a - N_c)M^2 \tag{12}$$

The magnetic moment is easily aligned along the c-axis and is hardly aligned with any axis normal to c. For the spherical shape, the shape anisotropy disappears (K_s=0) because c equals a and $N_a = N_c$.

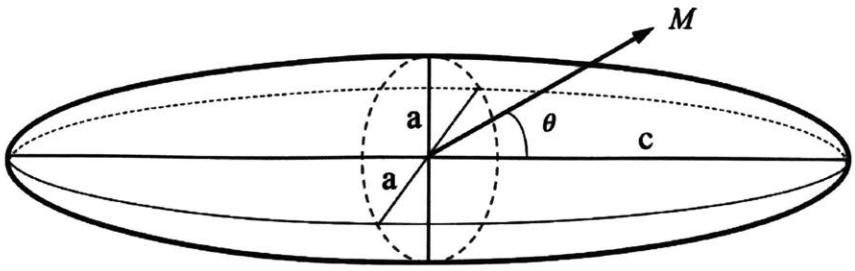

Figure 2-2 Prolate ellipsoid. From B. D. Cullity and C. D. Graham, *Introduction to Magnetic Materials,* (Institute of Electrical and Electronics Engineers) (1991)

The magnetoelastic energy is based on the magneto-elastic effect, which comes from spin-orbit interactions. The moment of spin is coupled with the lattice through orbital electrons. If the lattice is changed by strain, then the distance between the magnetic moments is also altered. Therefore, the interaction energies are changed and it produces magneto-elastic anisotropy. This is correlated to the phenomenon where the permeability or susceptibility of a material is changed when applying a stress on the material. Generally, without a stress M_s is controlled by magnetocrystalline anisotropy as characterized by the first anisotropy constant K_1. However, when a stress is applied, the direction of M_s is controlled by both K_1 and σ. Therefore, the energy in a cubic crystal, which depends on the direction of M_s, is defined as:

$$E = K_1(\alpha_1^2\alpha_2^2 + \alpha_2^2\alpha_3^2 + \alpha_3^2\alpha_1^2) - \frac{3}{2}\lambda_{100}\sigma(\alpha_1^2\gamma_1^2 + \alpha_2^2\gamma_2^2 + \alpha_3^2\gamma_3^2) \qquad (13)$$

$$- 3\lambda_{111}\sigma(\alpha_1\alpha_2\gamma_1\gamma_2 + \alpha_2\alpha_3\gamma_1\gamma_2 + \alpha_2\alpha_3\gamma_2\gamma_3 + \alpha_3\alpha_1\gamma_3\gamma_1)$$

where $\alpha_1, \alpha_2, \alpha_3$ are the direction cosines of M_s and $\gamma_1, \gamma_2, \gamma_3$ are the direction cosines of the stress σ. The first term of the equation is the magnetocrystalline anisotropy and next two terms are called the magnetoelastic energy. The final direction of M_s is that which minimize E and the direction is determined by various parameters such as $K_1, \lambda_{100}, \lambda_{111}$, and σ for any given stress

direction $\gamma_1, \gamma_2, \gamma_3$. In the elastically isotropic materials with isotropic magnetistrictions (λ_{100}= $\lambda_{111} = \lambda_{si}$), the magnetoelastic energy is:

$$E_{me} = -\frac{3}{2}\lambda_{si}\sigma cos^2\theta = \frac{3}{2}\lambda_{si}\sigma sin^2\theta \quad (14)$$

where θ is the angle between M_s and σ.

Finally, exchange anisotropy is observed at the interface between an antiferromagnetic material and a ferromagnetic material, where an exchange coupling is magnified. The typical features of exchange anisotropy are a shifted loop and high-field rotational hysteresis, and these are observed in multilayer structures and alloys. For example, when a strong field is applied to Co-CoO particles at 20°C (the Néel temperature, T_N, of CoO is about 20°C) the cobalt is magnetically saturated but the oxide is paramagnetic. However, the spins of the first layer of Co ions in the oxide are forced to be parallel to the adjacent cobalt atom due to the positive exchange force between the spins of adjacent Co atoms. When the particle is cooled below T_N with a field, the antiferromagnetic ordering is caused in the oxide, and the spin arrangement still persists at the interface. If the field is applied in the opposite direction, then the spin in the Co will reverse, and the spins of the oxide are forced to reverse due to the exchange coupling at the interface. However, this rotation is resisted by the crystal anisotropy of the antiferromagnet, so partial rotations of a few spins appear at the interface. This anisotropy usually displays unidirectional anisotropy, so the anisotropy energy is proportional to the first power of the cosine rather than the square of the cosine[96]:

$$E = -Kcos\theta$$

where K is the anisotropy constant and θ is the angle between M_s and the direction of the cooling field. Thus, the requirements for establishment of exchange anisotropy are field-cooling through T_N, contact between ferromagnetic and antiferromagnetic materials, and strong crystal anisotropy in the antiferromagnet.

2.1.4 Magnetic Domain walls

The concept of a magnetic domain introduced by Pierre-Ernest Weiss in 1906.[97] It were first experimentally observed in silicon-iron single crystal was by H. J. Williams, R. M. Bozorth, and W. Shockley in 1949. [98] Since this observation, domain theory is used to describe many magnetization processes. A domain indicates the interface in which the spontaneous magnetization has different directions, so the magnetizations are changed from one easy crystallographic direction to between domains[99]. This effect can be understood from an energetic perspective. In Figure 2-3 (a), the free magnetic poles at the edge of the sample are relatively strong, resulting in a large magnetostatic energy. By introducing the 180° DW in Figure 2-3 (b), the magnetization of each domain points in different direction, and the magnetostatic energy is reduced. Although introducing DWs costs energy due to the exchange interaction, their presence is energetically favored in many magnetic systems.

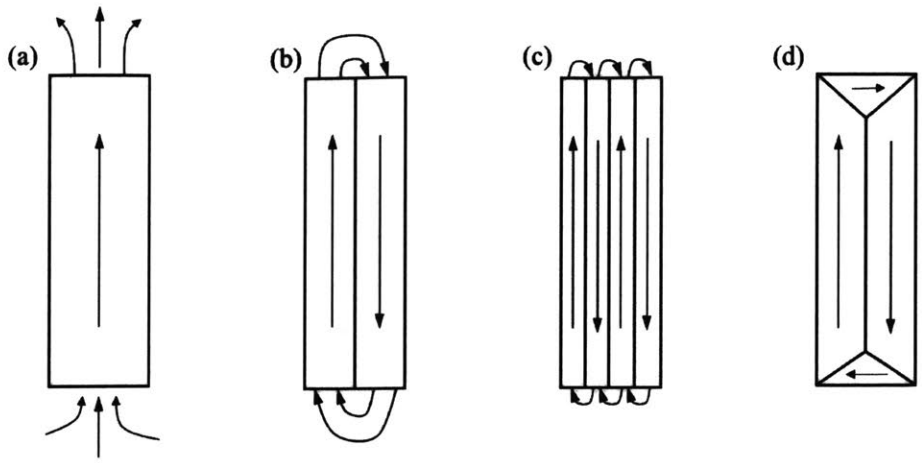

Figure 2-3 Magnetostatic energy and domain formation (a) magnetostatic (MS) energy of the single domain state, (b) Introduction of 180° domain walls to reduce MS energy, but increasing the wall energy, (c) smaller MS energy, but higher wall energy, (d) 90° closure domains eliminate MS energy, but cause elastic energy due to the strain incompatibility and increasing the anisotropy energy. From O'Handley, R.C. Modern magnetic materials: principles and applications. (John Wiley & Sons, Inc., 2000).

In a microscale structure, wide DWs become energetically unfavorable, as they serve as a transition area between different magnetizations. The internal structure of DWs are generally dependent on the size, structure and material parameters of the sample. However, there are two competing energy terms which are involved in spin orientations in a DW: anisotropy energy and exchange energy. As shown in the Figure 2-4, where the spin orientation in the thin film and the term from magnetostatic energy is neglected, the exchange energy prefers a parallel alignment of spin, which minimizes the angle difference between the spins. On the other hand, the anisotropy energy prefers an alignment of magnetization along an easy axis such as x axis, minimizing the number of spins pointing along an unfavorable hard axis. Therefore, the exchange energy prefers gradually changing the spin direction in DWs over a large length scale, whereas the anisotropy energy tends to reduce the DW width to minimize the number of spins which align along the hard axis. The competition between these two energy terms is expressed as[94]:

$$\sigma_{ex} + \sigma_{ani} = JS^2\theta^2 + \sum_{i-1}^{N} Ksin^2\theta d\theta \tag{15}$$

where J is the exchange anisotropy constant, S is the electron spin, N is the number of spins within the DW, and θ is the angle between the nearest neighbor spins, K is anisotropy constant. Considering the simple DW case, the above equation can be written as[94]:

$$\sigma_{ex} + \sigma_{ani} \approx JS^2 \frac{\pi^2}{Na^2} + K_u Na \tag{16}$$

where a is the atomic constant, angle approximately $\theta_{ij} \approx \pi/N$, and integral approximation for simplicity. The above equation has dependency on N, which is directly correlated to the width of the DW. It is minimized for $N_0 = (JS^2\pi^2/K_u a^3)^{1/2}$ and the width of the DW is N_0 a $\approx \pi(A/K_u)^{1/2}$, where A is the exchange stiffness constant A = JS^2/a. For example, the thickness of a DW in soft materials with small anisotropy is approximately 0.2 μm, whereas the thickness of a DW in hard materials with high-anisotropy is approximately 10 nm.

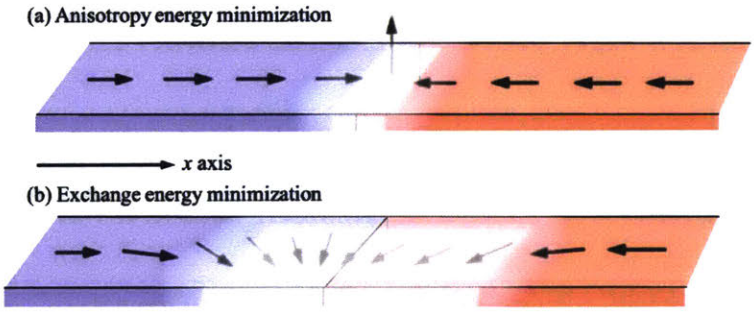

Figure 2-4 Spin orientations in a magnetic domain wall.

The most common type of 180° DW is a Bloch wall, where the magnetization rotates in the plane parallel to the plane of the DW. The other DW type is a Néel wall, where the magnetization rotates in the plane perpendicular to the plane of the DW. The DW energy densities for these DWs have different due to the thickness of the thin film. The Bloch wall energy increases with decreasing film thickness because of increasing magnetostatic energy at the charged surface. However, the Néel wall energy density decreases with decreasing film thickness because the amount of surface is also reduced, and the Néel wall is usually stable in magnetic thin films below 50 or 60 nm thickness. In this thesis, all the in-plane magnetic anisotropy samples (IMA) exhibit several kinds of DW structures due to the antidot patterns. Furthermore, the remnant magnet configurations have dependency on the symmetry of the pattern, the periodicity of pattern, and the diameter of the hole, as shown in Figure 4-6.

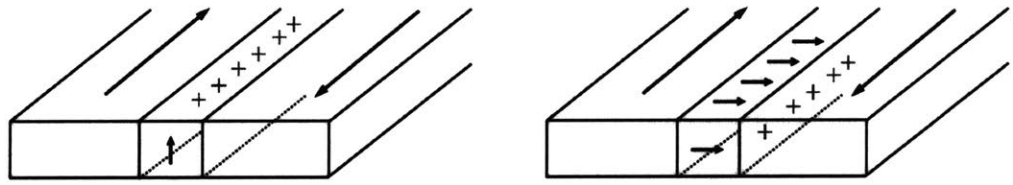

(a) Bloch wall **(b) Neel wall**

Figure 2-5 Two different types of domain wall: (a) Bloch wall, with charged surfaces on the external surfaces of the sample and (b) Neel wall with charged surfaces internal to the sample. From O'Handley, R.C. Modern magnetic materials: principles and applications. (John Wiley & Sons, Inc., 2000).

2.1.5 Perpendicular magnetic anisotropy

The presence of perpendicular magnetic anisotropy (PMA) is a complicated phenomenon because magnetostatic potential energy generally favors an in-plane anisotropy (IMA) according to the conventional theory of magnetic thin films. As mentioned in Section 2.1.3 magnetic anisotropy, the magnetization of a thin film prefers the direction that can reduce the demagnetization fields. If the magnetization of a thin film is magnetized along the z axis (out-of-plane), then the magnetic free poles generate a large demagnetization field, which is unfavorable. Therefore, to prevent a large demagnetization field, the magnetization of a thin film tends to align in the plane of the material. However, with the introduction of new concepts such as spin-orbit interaction, the easy axis of a thin film can be parallel to the z-axis when an ultra-thin ferromagnetic layer is embedded between nonmagnetic materials such as Pt and Pd[100-103] or a capping oxide such as MgO[104] or Gd_2O_x[105].

PMA can be explained by a strong interfacial interaction, and it can be described by an effective anisotropy constant[106-107] in Co/Pt multilayers:

$$K_{eff} = \frac{2K_s}{t_{Co}} + K_v \tag{17}$$

where t_{Co} is the thickness of an individual Co layer, K_s is the anisotropy originating from the interface per unit area, $K_v = K_c - 0.5\mu_0 M_s^2$ is the volume contribution of Co, including magnetocrystalline, magnetoelastic anisotropies, and a negative shape anisotropy term. Thus, the anisotropy of materials is determined through the competition between the magnetostatic energy minimization and energy reduction by the spin-orbit coupling. By decreasing the thickness of Co

layer, the effective anisotropy changes from negative to positive, indicating a transition from in-plane anisotropy ($K_{eff} < 0$) to out-of-plane anisotropy ($K_{eff} > 0$)[108-113].

The materials with PMA have a great deal of advantages compared to the material with IMA. First, the average anisotropy energy of PMA materials is much larger than that of in-plane materials. As shown in Section 2.1.3, the width of a domain wall is determined by two competing energies: the exchange energy and the anisotropy energy. When increasing the anisotropy energy, the width of a DW becomes narrower, so DWs in PMA materials are narrower than in IMA materials. For example, the width of DWs in a PMA material is around 1~10 nm; while that of DWs in an in-plane material is approximately 100nm[94]. Furthermore, thermal instability, which results in the curling of magnetization and is frequently observed at the edge of in-plane materials, is not exhibited in PMA materials[114-115]. Consequently, these structures have been widely studied and have attracted a great deal of interest in high density magnetic recording research.[116]

2.2 Superparamagnetic beads

Lab-on-a-chip or biomedical applications based on microfluidic systems generally use magnetic nano- or microparticles which can be easily manipulated using a permanent magnet or electromagnets, independent from normal microfluidic or biological processes[117-119]. The size of these magnetic particles varies from several microns in diameter down to tens of nanometers[51]. Superparamagnetic behavior is dependent on the size of particle, such that larger microscale magnetic particles cannot exhibit superparamagnetism. However, micro-sized particles can be designed to have superparamagnetism through composition. Generally, these beads or particles consist of many separated small, superparamagnetic grains of iron oxide (magnetite Fe_3O_4 or maghemite γ–Fe_2O_3), embedded in a polymer matrix such as polystyrene[120]. Recently, three types of embedding for the paramagnetic micro-sized beads have been reported by Thanh[121]: "fruitcake" (the nanoparticles are uniformly distributed in the matrix), "orange peel" (the nanoparticles are located on the surface of the bead), and "plum cake" (the nanoparticles are concentered in the center of matrix). Figure 2-6 shows these three types of micro-sized superparamagnetic beads. The matrix also serves as a separator medium to reduce inter-particle interaction and prevents the loss of superparamagnetism. The surface of superparamagnetic beads is coated to stabilize the beads in solution and render them non-toxic and biocompatible. For example, superparamagnetic particle used in biomedical applications should be water-dispersible. Thus they usually feature a hydrophilic surface coating such as a carboxylate-functionalized group.

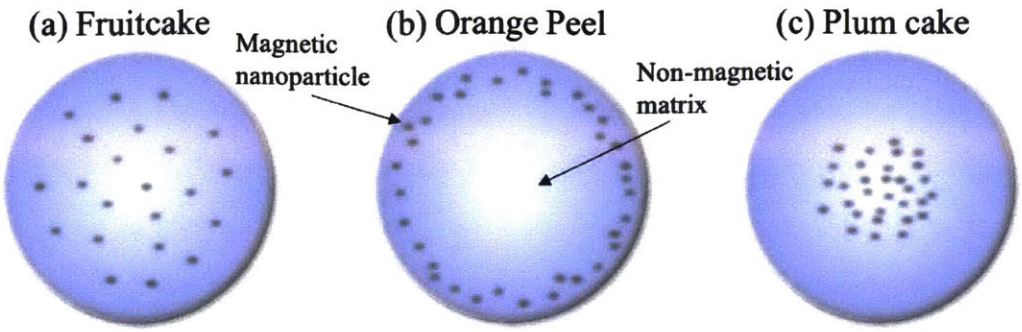

Figure 2-6 Several types of superparamagnetic microbead. From Ruffert, C. Magnetic bead-magic bullet, Micromachines, 7, 21 (2016)

Nowadays, a variety of magnetic beads are used for different applications and they are commercially available: Dynabeads® magnetic beads provided by Invitrogen, BcMag™ by Bioclone Inc., ProMag™ and BioMag® from Bangslabs, SupraMag™ by Polymicrosheres Inc., TurboBeads® by Turbobeads Lic., and SPHERO™ Polystyrene Magnetic Particles by Spherotech. These superparamagnetic beads are used in binding, purification, and magnetic separation of biomolecules such as proteins, cells, DNA fragments, and antibodies, because the size of beads are comparable to those of cells (10-100 μm), proteins (5-50 nm) and small bacteria (20-450 nm). In addition, these superparamagnetic beads which can be manipulated by a magnetic field do not maintain their magnetization and decompose into particles after removing the magnetic field. As mentioned before, unlike electrical manipulation, the magnetic interaction rarely affects the sensitive parameters biological applications such as pH, ionic concentration, and temperature[122]. Furthermore, biological systems usually have little magnetic susceptibility, which results both in high selectivity and non-interference of magnetic fields. Therefore, superparamagnetic beads have potential for use in immunoassays, cell manipulation and cellular-specific targeting, DNA

extraction[123], magnetic resonance imaging[124], targeted medication[125], and hyperthermia therapies[51,126].

Given the advantages of superparamagnetic beads, the beads are widely studied and used in lab-on-a-chip applications. In the following section, we discuss what the superparamagnetism is and several forces that act on magnetic particles.

2.2.1 Superparamagnetism

Superparamagnetism is observed in small ferromagnetic particles on the order of tens of nanometers or less due to fundamental size-effects. In nano-particles, reduced energy from a multi-domain configuration is no longer favorable, so the small particles generally consist of single domain structure with magnetization reversal occurring via coherent spin rotation rather than through domain expansion via domain wall propagation.

The typical radius below which a spherical nano-particle will be single domain is given by[94,127]:

$$R_{sd} \approx \frac{6\sqrt{AK_u}}{\mu_0 M_s^2} \tag{18}$$

where A, the exchange stiffness, is a measure for the critical temperature for magnetic ordering of the material, K is the magnetic anisotropy of the particle, μ_0 is the permeability of free space, and M_s is the saturation magnetization. For most magnetic materials, the size limit for superparamagnetism is in the range of 10-100nm.

Since the first research done by Néel[128], Brown[129], and Aharoni[130] on uniaxial magnetic nanoparticles, superparamagnetic relaxation process has been well studied. Generally, a particle with uniaxial anisotropy is designed as a prolated spheroid with the easy axis of magnetization along the major axis. As shown in Figure 2-7, the magnetic anisotropy energy is given by[127]:

$$E_{ani}(\alpha) = -KVcos^2\alpha \tag{19}$$

where α is the angle between the direction of magnetization $\vec{M}$and the easy axis, V is the volume of the particle, and K is the uniaxial magnetic anisotropy constant. Figure 2-7 (b) represents the magnetic anisotropy energy as a function of the angle, α, where two minima of energy are located at $\alpha = 0$ and π, separated by an energy barrier KV. Without an external field, the magnetic moment of a particle has equal probability to arrange along either direction of the easy axis. Reversal between the two minima can be achieved when the thermal energy is larger than energy barrier ($k_BT > KV$). According to the Neel-Brown theory[128-129], the relaxation time τ of the net magnetization of the particle under an activation law is:

$$\tau = \tau_0 \exp\left(\frac{\Delta E}{k_B T}\right) \tag{20}$$

where ΔE is the energy barrier to moment reversal, and k_BT is the thermal energy. For the non-interacting particles, the pre-exponential factor τ_0 is of the order 10^{-10}-10^{-12}s and only weakly dependent on the temperature. For the energy barrier ΔE, this term is correlated to the magnetocrystalline anisotropy, shape anisotropy, strain anisotropy, and exchange anisotropy.

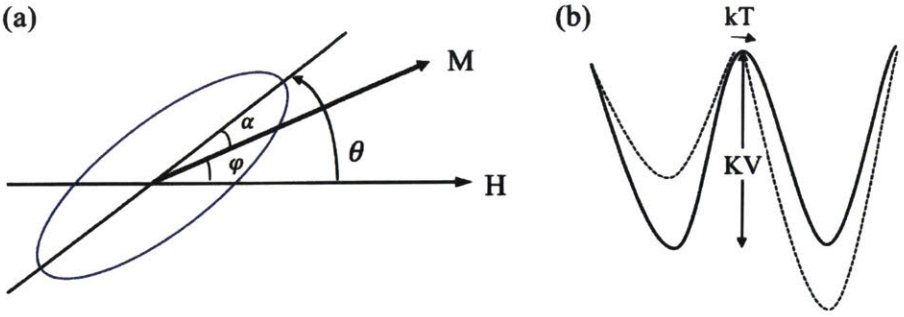

Figure 2-7 (a) Schematic of a prolate spheroid depicting a nanoparticle with uniaxial magnetic anisotropy in the presence of an external magnetic field $\vec{H}$ at an angle θ relative to the direction of the anisotropy axis. Angles α, φ give the orientation the magnetization of the particle, $\vec{M}$, relative to the anisotropy axis and the magnetic field, respectively. (b) Magnetic potential energy as a function of angle α, in the absence of an applied field, solid line, and in the presence of an applied field along the anisotropy axis, dash line. The minima occur at $\alpha = 0, \pi$. From Papaefthymiou, G. C. (2009). Nanoparticle magnetism. *Nano Today*, 4(5), 438–447. https://doi.org/10.1016/j.nantod.2009.08.006

Thermally activated flipping of the net moment direction can be observed when ΔE is comparable to $k_B T$. For example, at room temperature and for the small particles, the ΔE of moment reversal is equivalent to the thermal energy so the time-averaged magnetization of the particle is measured as zero. Therefore, the barrier ΔE, which is proportional to the particle anisotropy and volume, is an important factor to develop the superparamagnetism. In addition, the observation of superparamagnetism is also dependent on the measurement time τ_m of the experimental technique. As shown in the Figure 2-8, if the relaxation time is much larger than the measurement time ($\tau \ll \tau_m$), then the flipping is fast relative to the experimental time and the time-average moment of particle is measured as zero. This state is the superparamagnetic state. If the relaxation time is much smaller than measurement time ($\tau \gg \tau_m$), however, then reversal is slow and a well-defined state can be observed. This is called a 'blocked' state of system. The blocking temperature (T_B) is defined as the middle point between the two states ($\tau = \tau_m$).

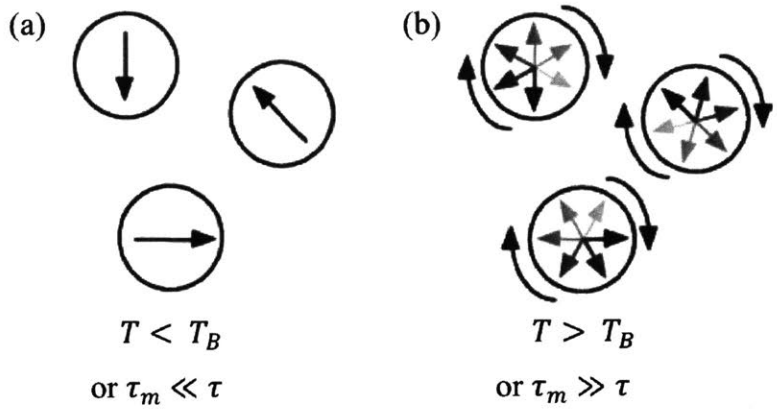

Figure 2-8 The circles depict three magnetic nanoparticles, and the arrows represent the net magnetization direction in those particles. (a) The measurement time τ_m is much smaller than the relaxation time. A well-defined state can be observed (quasi-static state). (b) The measurement time τ_m is much larger than the relaxation time, then a time-averaged net moment of zero will be observed (superparamagnetic state). From Pankhurst, Q. a, Connolly, J., Jones, S. K., & Dobson, J. (2003). Applications of magnetic nanoparticles in biomedicine. Journal of Physics D: Applied Physics, 36(13), R167–R181. https://doi.org/10.1088/0022-3727/36/13/201

2.2.2 Force on a magnetic particle

In order to understand how a magnetic field can transport and manipulate magnetic beads, it is important to quantify the magnetic field gradient, supporting the transport of the beads. While a uniform magnetic force only exerts a torque on the beads, a field gradient can transport the beads. From the consideration of a moment in a field $\boldsymbol{B}$, then the magnetic potential energy is defined as:

$$U = -\boldsymbol{m} \cdot \boldsymbol{B} \tag{21}$$

and the magnetic force is:

$$F = -\nabla U \tag{22}$$

The magnetic force acting on single beads, using a point-like magnetic dipole $\boldsymbol{m}$, is[131,132]:

$$F_m = \nabla(\boldsymbol{m} \cdot \boldsymbol{B}) \approx (\boldsymbol{m} \cdot \nabla)\mathrm{B} \tag{23}$$

where the second part of the above equation is based on the magnetization $\boldsymbol{m}$ of the particle not varying in space ($\nabla \cdot \boldsymbol{m} = 0$).

In the case of magnetic particles suspended in a weakly diamagnetic medium such as water, the total moment of the particle can be written $\mathbf{m}=V_m\boldsymbol{M}$ (where V_m is the volume of the particle and $\boldsymbol{M}$ is its volumetric magnetization.) The effective susceptibility of the particle is $\Delta\chi = \chi_m - \chi_w$, where $\chi_m$is the susceptibility of the magnetic particle, and χ_w is the susceptibility of water. Thus,

$$\mathbf{H} = \frac{\boldsymbol{B}}{\mu_0} \tag{24}$$

where μ_0 is the permeability of free space.

$$\mathrm{M} = V_m\mathrm{M} = V_m \chi\boldsymbol{H} \tag{25}$$

Substituting these expressions and rewrite the expression for the force on a magnetic dipole in a magnetic field gradient gives:

$$F_m = \frac{V\chi}{\mu_0}(\boldsymbol{B} \cdot \nabla)\mathrm{B} \tag{26}$$

If we consider the magnetic particles that are constrained to move in the x direction, the x component of the force is defined as:

$$F_{m,x} = \frac{V\chi}{\mu_0}\left(B_x\frac{\partial}{\partial x} + B_y\frac{\partial}{\partial y} + B_z\frac{\partial}{\partial \mathrm{z}}\right)B_x \tag{27}$$

Thus, both the magnitude of the magnetic field and the field gradient need to be large to have a strong magnetic actuation force.

2.2.3 Stokes drag force in viscous medium

In many applications, magnetic particles are separated in a liquid solution by Brownian fluctuation. Therefore, to transport the magnetic beads in a fluid it is necessary to consider the force exerted on the beads from the fluid. The inertial force and viscous force on the beads can be characterized by the Reynolds numbers, which is defined as[133]:

$$R_e = \frac{\rho v L}{\mu} \tag{28}$$

where ρ is the density of the fluid, v is a characteristic velocity of the fluid with respect to the object, L is a characteristic linear dimension, and μ is the dynamic viscosity of the fluid. There are two types of flow: laminar and turbulent. Laminar flow occurs at low Reynolds numbers where viscous forces are dominant. While turbulent flows occurs at high Reynolds numbers where at high Reynolds numbers.

The hydrodynamic drag force, which is the result of the velocity difference between the magnetic particle and the liquid, is given by Stokes law[134]:

$$F_d = 6\pi\eta r\Delta \mathrm{v} \tag{29}$$

where η is the viscosity of the medium surrounding the beads, r is the radius of bead, and Δv is the difference between the magnetic particle and the liquid. From the Eq. (26) and Eq. (29), the maximum flow rate of the particle in a surrounding static liquid is[47]:

$$\Delta v = \frac{2r^2\chi(\boldsymbol{B}\cdot\nabla)\boldsymbol{B}}{9\mu_0\eta} \equiv \frac{1}{\mu_0}\xi(\boldsymbol{B}\cdot\nabla)\mathbf{B} \tag{30}$$

with

$$\xi \equiv \frac{2r^2\chi}{9\eta} = \frac{V\chi}{6\pi r\eta} \tag{31}$$

being the "magnetophoretic mobility" of the particles, which describe how magnetically manipulable the particle is.

2.2.4 Other forces on a magnetic particle

Other forces acting on the beads are electrostatic forces including van der Waals attraction and electrostatic repulsion, which lead to bead-bead interactions. These forces can be modified through surface coating. In addition, the DLVO interaction, which describe the aggregation of aqueous dispersions quantitatively, between the charged surface of beads and a liquid medium must also be considered, and the hydrophobic or hydrophilic characteristics of the bead can affect the dynamics of beads[135-137]. However, these forces are complicated, and it is hard to represent these forces as a general way in our model. Thus, these forces will not be considered in our simulation models, but they can be potential source of variation between simulation and experimental results.

2.2.5 Suprastructure formation

For the selective transport or separation of beads, agglomeration of the beads is not desired. The concentration of beads is usually kept low to prevent agglomeration and increase interbead distance. At high concentration, the beads tend to form supraparticle structures[47] as described in Figure 2-9. Without an external magnetic field, the net magnetization of superparamagnetic beads is zero, and there is no magnetic interaction. By applying a magnetic field, a torque τ acts on the magnetic moment vectors $\vec{m}$ of the beads:

$$\tau = \vec{m} \times \vec{B} \tag{32}$$

Due to the torque τ, the magnetic moments are aligned which leads to the development of a stray field. If the magnetic field is homogeneous, then the beads seldom assemble each other. However, if the interbead distance is small enough, the inhomogeneous stray fields lead to attractive forces between the beads. Thus, the attractive force results in an alignment of particles along the lines of the magnetic field, called a chain. This chain structure can be rotated when a magnetic field is rotated in–plane. In addition, rotating the field in the *xz* plane can manipulate the shape and motion of chain structures.[138] When increasing the frequency of the rotating fields, the lag between the angular moment of the chain and the magnetic field increases, so the beads can no longer align along a chain axis. Finally, the chain collapses and cluster structures are formed as shown in Figure 2-9. Even though the magnetic configuration of each bead is not known specifically, calculations show that the magnetic domains aligned antiparallel to each other[139].

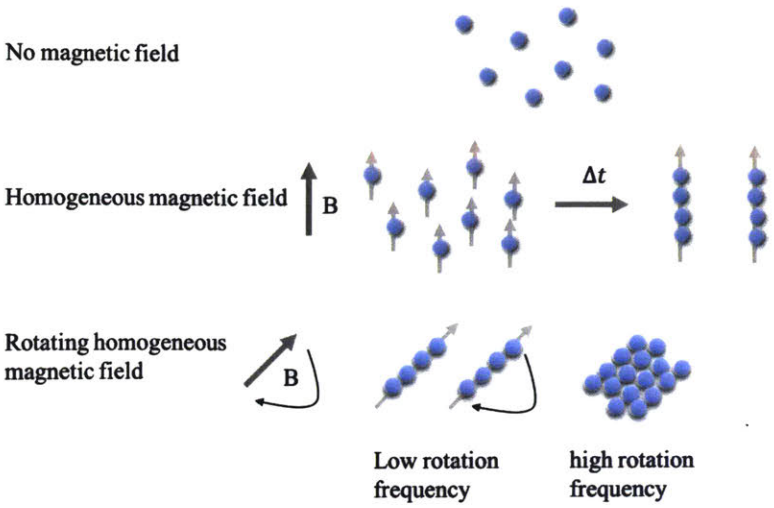

Figure 2-9 The formation of suprastructures of superparamagnetic beads. Without an external magnetic field, the net magnetization is zero. Under an external and homogeneous magnetic field, the moments of the beads are aligned. If the bead concentration is sufficiently high, then the beads form 1D agglomerates (chains) due to the inhomogeneous stray field of each bead. At a high frequency of rotating field, the chains collapse into 2D cluster structure. Eickeuberg B. Superparamagnetic bead as self-assembling matter for microfluidic applications. Bielefeld; Bielefeid university (2014).

To describe the behavior of a chain under the influence of a rotating magnetic field. The Mason number, or the ratio of viscous to magnetic forces, is useful. The Mason number is given as[140]:

$$Mn = \frac{16\eta\omega}{\mu_0 \chi^2 H^2} \tag{33}$$

where η is the viscosity of the liquid, ω is the angular velocity of the field, μ_0 is the vacuum permeability and χ is the magnetic susceptibility. Generally, the average length of chain structures decreases with an increasing Mason number, where viscous force dominates over the magnetic force. The proportionality between the chain length L and the Mason number is expressed as:

$$L \propto \frac{1}{\sqrt{Mn}} \tag{34}$$

At a certain value of the Mason number, the chain starts to form an S-like configuration. If the Mason number further increases, then the chain is divided into shorter chain segments or into a two-dimensional cluster.

Chapter 3

Simulation and experimental methods

To understand and describe the transport phenomena of Superparamagnetic beads (SPBs) and the effect of periodic patterns, we conduct both simulation and experimental procedures, making use of standard methods. Here we discuss the details of these procedures.

3.1 Micro-magnetic simulation of bead-magnetic pattern interaction

The dynamics of SPBs on the periodic antidot arrays will be affected by the magnetostatic potential energy (see Eq. (21)), which is coming from the magnetically textured of the antidot arrays and a rotating elliptical magnetic field. The magnetic force, which is defined as the negative gradient of the magnetostatic potential energy (c.f. Eq. (22)), is a driving the superparamagnetic beads. We quantitatively describe the interaction between the SPBs and the antidot pattern on the basis of the magnetostatic potential energy landscape and the magnetic force. Through these characteristics, we understand the mechanism of the SPB transport and explain the dynamics of SPBs.

Most previous studies have been calculated the magnetic field gradient and binding force between SPBs and magnetically textured patterns that are based on domain wall structure. These calculations over-simplify the bead dynamics. For instance, they ignore the shape and volume of the beads and also erroneously treat them as ferromagnetic particles[141-142], even though they regard the hydrodynamic force. Recently, the SPB movements on a two-dimensional array have been

analyzed by several researchers based on the point poles with positive and negative charges. However, other simulations still suffer in the scope of the data collected due to a long calculation time on the order of a month due to the micro-scale.

We have calculated the magnetostatic energy and binding forces between SPBs and periodic patterns through a well-developed calculation method that is flexible and highly efficient. Moreover, several parameters such as the bead radius, periodicities of the pattern, lattice symmetries, and relaxed magnetization configuration can be easily modified in this calculation method. For analyzing the experimental results, we calculated the stray field from the edge of the hole over a large volume of space above the pattern, leading to quantify the actual magnetic energy landscape in which SPBs move. Furthermore, we consider the beads as superparamagnetic beads by using real material parameters.

We calculated the magnetostatic potential energy and binding force through three steps of simulation: DW configuration through micro-magnetic simulation, the integration of stray fields, and the calculation of the magnetostatic potential energy of SPBs.

In the first step, object-oriented micro-magnetic framework (OOMMF)[143] and Mumax[144] are used to find the relaxed magnetization configuration after saturating the film along ϕ with respect to the x-axis (principal direction) in samples with varying geometry and dimensions. In OOMMF and Mumax, the magnetization dynamics is described by the Landau-Lifshitz-Gilbert equation of motion:

$$\frac{1}{\gamma}\frac{dm}{dt} = -\frac{1}{1+\alpha^2}\left(m\times H_{eff}\right) - \frac{\alpha}{1+\alpha^2}m\times\left(m\times H_{eff}\right) \tag{35}$$

where $\gamma$is the gyromagnetic ratio, $m = M/M_s$ is the normalized magnetization vector, α is the Gilbert damping parameter, and $H_{\text{eff}}$is the total effective field, including the exchange, anisotropy,

magnetostatic and external magnetic fields. Thus, OOMMF and Mumax determined the relaxed domain wall configuration from the initial given configuration. Input scripts included a system geometry (such as the number of cells, periodic boundary condition, size of the box or the size of grid), initial magnetization, material parameters, running time, or running options such as minimizing the total energy.

For the antidot arrays with in-plane anisotropy, the initial condition is that all magnetic moment align along $\theta = 0°$ and $\theta = 45°$ with respect to the *x*-axis. For the antidot arrays with perpendicular magnetic anisotropy, we fixed the resulting magnetizations to be aligned along the *z*-axis. In the micromagnetic simulation, the systems were divided into $4 \times 4 \times 40$ nm^3 cells, where the cell high is equal to film thickness to reduce the number of cells and thus calculation time. The cell dimensions in the *xy* plane is slightly smaller than the exchange length of Co (~5nm). Material parameters consistent with bulk Co were used: saturation magnetization $M_s = 1.4 \times 10^6$ Am^{-1}, damping constant = 0.1, and exchange stiffness constant $A = 3 \times 10^{-11}$ Jm^{-1} [145]. For a Co/Pt multilayer structure, to simplify the simulation process, we considered the film structure as a continuous 5 nm of Co layer instead of the Co/Pt multilayer.

DW structures were used as an input file to compute the stray field **B**(**r**) as a function of position **r**. The calculation of the stray field based on a point dipole integration approximation[146], wherein each space cell *i* above the patterns has a field, B_i, expressed as

$$B_i = \sum_j \frac{\mu_0}{4\pi r^3} [3(m_j \cdot \hat{r_{ij}})\hat{r_{ij}} - m_j] \qquad (36)$$

where m_j is the magnetic moment of a pattern cell *j*, r_{ij} is the distance between the space cell *i* and the cell of pattern *j*, and $\hat{r_{ij}}$ is the unit vector along the line that is connected between cell *i* and *j*. Stray fields were calculated for spaces above the magnetic antidot arrays, using a unit cell size of

$40\times40\times40$ nm^3. The calculated spaces are large enough to accommodate beads with diameter up to 8 μm. This calculation step is the most computationally intensive, so we used the periodic boundary condition and the Amazon Web Service (AWS)[147].

After calculation for the integration of stray field, the magnetostatic potential energy of SPBs was approximated by integrating the dipolar energy density $-\boldsymbol{M}\cdot\boldsymbol{B}$ over the bead volume. We assumed that the SPBs had a radius R at a vertical height (h) from the top of the magnetic pattern. In this step, we assumed that the bead magnetization $\mathbf{M} = \chi\boldsymbol{B}$, and the volume susceptibility χ was considered as 800 kAm^{-1}T^{-1}, suitable for commercial SPBs[136]. In our calculation, we assumed that the SPBs are located just on the magnetic pattern surface due to the strong pulling force along the z. Thus, h can be set as 0, and the diameter of SPBs is from 2.8 μm to 7.8 μm.

3.2 Sample fabrication

The magnetic antidot pattern was prepared through several lithography steps including a standard optical lithography or a microsphere lithography, followed by sputter deposition, and lift-off on a Si (100) wafer with native oxide. The shape of the antidots was chosen to be circular to ensure that the holes themselves did not contribute to the anisotropy of the antidot array. All the wafer was coated with a 70-80nm thick protective SiO_2 layer through RF sputtering deposition. Thus, the SiO_2 was used to prevent electrical shorting and SPBs from sticking on the surface of the samples.

3.2.1 Microsphere lithography

Polystyrene microspheres can form a self-assembled periodic array on a floating surface that can be used to pattern the substrate with the desired geometry. By using these properties, the monolayer colloidal sphere templates can be made easily with simple methods[148-155].

There are two templates in microsphere self-assembly: hexagonal-close-packed (hcp) monolayers and non-close-packed (ncp) layers. Because the hcp structure is a thermodynamically stable arrangement of monodisperse spheres, the most frequently templates in self-assembly are hcp layers. To obtain the templates, there are various interfacial self-assembly strategies: drop-coating, dip-coating, spin-coating, electrophoretic deposition, self-assembly at the gas/liquid interface, and floating-transferring technique. Nagoyama and co-workers[155] observed the randomly dispersed polystyrene spheres moving into hcp arrangements when they dropped a dilute

nanosphere suspension onto the flat surface in Figure 3-1 (a). In the method, the process is dependent on an evaporation rate and an attractive capillary force. They also developed another self-assembly method such as withdrawing a substrate during a dip-coating procedure, as shown in Figure 3-1 (b).

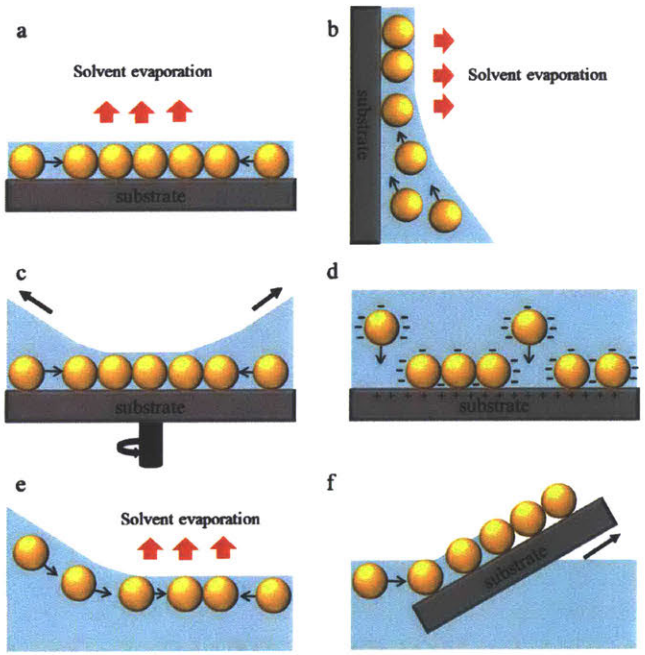

Figure 3-1 Microsphere lithography strategies (a) drop-coating; (b) dip-coating; (c) spin-coating; (d) electrophoretic deposition; (e) self-assembly at the gas/liquid interface; (f) floating-transferring technique From X. Ye, L. Qi, Two-dimensionally patterned nanostructures based on monolayer colloidal crystals: Controllable fabrication, assembly, and applications, *Nano Today*. 6 (2011) 608–631.

Furthermore, in the spin-coating strategy (Figure 3-1 (c)), the solvent flows across a substrate at a high rate and the colloidal spheres are assembled into an hcp monolayer on the substrate. The thickness of the hcp patterns is mostly affected by the speed of a coater, the concentration of the colloidal suspension, and the wetting of the substrate. Because the process is rapid and does not need complex and expensive equipment, it is good for mass production.

In electrophoretic deposition, as shown in Figure 3-1 (d), the suspension is confined between two electrodes, and the spheres move to the electrode, making the hcp patterns when an electric field is applied. In the deposition, the array of spheres rapidly self-assembles and is easily manipulated since electrophoretic movement accelerates the speed of the beads and the growth rates on the electrodes.

In addition, in the self-assembly at the gas/liquid interface (Figure 3-1 (e)), the colloidal suspension is spread onto the liquid surface and the spheres self-assemble, making highly ordered hcp patterns after evaporation of the solvent. Using this method, the resultant floating hcp monolayers can be readily transferred onto the substrate by a lift-off technique as shown in Figure 3-1 (f). The process is more desirable than others owing to the potential of making a large area of hcp pattern with high quality.

In the thesis, the floating-transferring technique has been used to create monolayer ordered arrays of polystyrene microspheres as a lithography template. The polystyrene particles with 1 μm diameter are in 10wt% aqueous solution that was diluted by an equal amount of ethanol. A Si wafer was cleaned with base bath cleaning, and afterwards the substrate was kept in 10% sodium dodecyl sulfate for 24 hours to modify the substrate to be hydrophilic. Diluted polystyrene solution was dropped and spread on the Si wafer. After that step, the wafer was slowly immersed in a glass vessel that was filled with DI water, and the polystyrene particles started to disperse on the gas/liquid interface (Figure 3-2 (a)). The sodium dodecyl sulfate solution was dipped into the water surface to aid and accelerate the self-assembly of polystyrene beads. As described in Figure 3-2 (b), the microspheres assemble spontaneously with each other, and such a monolayer was lifted off using the Si wafer (Figure 3-2 (c)).

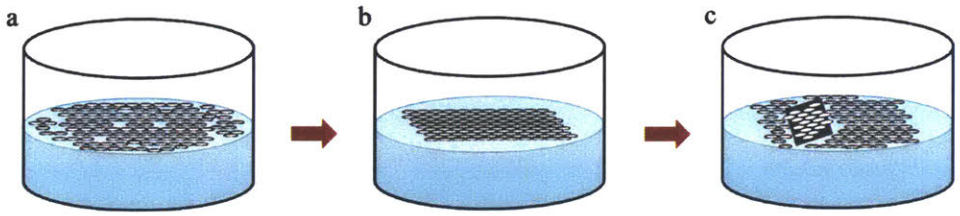

Figure 3-2 The process of the self-assembly of polystyrene particles

The self-assembly of polystyrene particles by the floating-transferring technique is shown in Figure 3-3. The hcp layers of polystyrene beads are represented in Figure 3-3. The largest area that could be produced from the method is around 0.6 cm^2. In some places, they show a perfect close-packed arrangement, but there are still some defects like missing or mismatched boundaries.

Figure 3-3 The SEM images of the 2D polystyrene patterns

The ordered monolayer of polystyrene beads can be used as a mask to deposit a thin magnetic film using magnetotron sputtering. Thus, the array of polystyrenes acts as a shadow mask to allow for pattern formation on the substrate surface. Before depositing the thin-film overlayers, reactive ion etching (RIE) can be used to tailor various spacing sizes and shapes. Figure 3-4 shows SEM images of self-assembled polystyrene arrays after they were etched in oxygen at DC powers

of 90 W, 120 W, and 150 W for the indicated time. The morphology of the beads remains spherical, and the hcp patterns remain intact during etching. However, the spacing between the spheres can be tuned in the following way. For example, the diameter of polystyrene beads is 0.925 μm, 0.854 μm, 0.775 μm, and 0.709 μm. for the etching times 2 min 30 secs, 3 min 45 secs, 5 min, and 6 min, respectively, when the RIE power is 120 W. Therefore, the size of bead and the spacing between the beads can be controlled by the etching times and the power level.

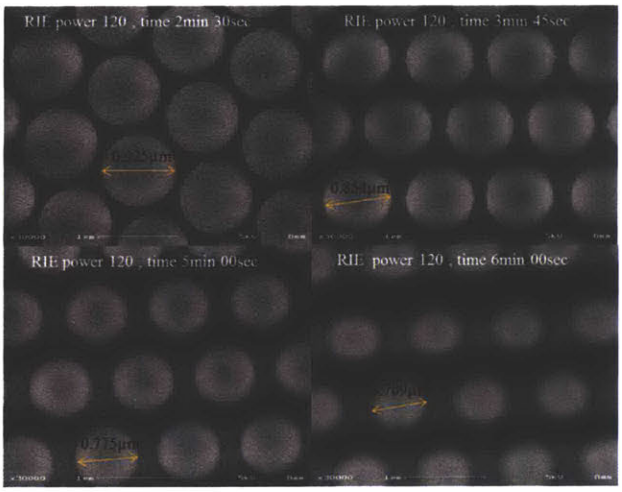

Figure 3-4 SEM images of the polystyrene bead etched by oxygen along with each etching time

3.2.2 Optical lithography

For uniform structures a higher level of resolution can be achieved by photolithographic techniques such as optical lithography. A polymeric mask is created directly on a Si wafer by exposure of a photosensitive polymer resist to light. The light-exposed area of the photoresist changes to a special chemical structure that permits a developer to dissolve. The exposed wafer is

soaked in the developer for some time. This process converts the latent pattern to a visible pattern, because the developer dissolves the exposed areas on the wafer.

The Si wafer is heated at 180 °C for 8 minutes to drive off any moisture or organic contamination. To encourage adhesion of the photoresist to the wafer, hexamethyldisilazane (HMDS) is applied by using spin coating, wherein the substrate is rotated at high speed to spread the material regularly. The wafer is put on a hot plate to dry the HMDS at 115°C for 1 minute. Then, the wafer is covered with photoresist again, using a spin coater. The spin coater typically runs around 400 rpm for 60 seconds, and the uniformly coated wafer is again baked on the hot plate to drive off excess photoresist. After baking the wafer with the photoresist, it is exposed to intense UV light for ~3.7 seconds that comes through the patterned mask, which is a chrome mask with patterned holes that allow UV to shine through. Finally, the resist-coated substrate is developed in MF-CD 26 solution for ~30 seconds and rinsed in deionized water and dried with nitrogen.

3.2.3 Sputter deposition

Sputter deposition is a popular deposition process whereby particles are ejected from a target material and moved to a wafer. All antidot array were patterned onto thermally–oxidized Si (100) wafers, and metallic layer and surface passivation layers were grown by a 4-target DC/RF magnetron sputter operating at a base pressure of $\sim 10^{-7}$ Torr. 40nm thick Co layer was deposited by DC magnetron sputtering at room temperature at an Ar pressure of 3.0 mTorr. Various Ta layers and Pt layers were deposited, which acts as a seed layer, in rotation mode using a DC power supply at 0.05-0.2 A and 310-470 V. For the SiO_2 deposition, an RF power supply was used at 200 W in

stationary mode. Before the deposition, we were waiting about 2-3 minutes as a pre-sputtering process to clear surface contamination. The general argon pressure was 2-3 mTorr and the thickness of deposited layers was controlled by the deposition time and the rate, which is calculated based on thick calibration films. For the thickness measurement, X-ray reflectivity or ellipsometry were used to obtain metallic film and SiO_2 film thicknesses, respectively.

3.2.4 Lift-off

A standard lift-off technique is used in microfabrication using photolithography. In this process, the photoresist is removed from the substrate, leaving only the deposited material in the desired pattern. The wafer, the mixture of the target materials and the photoresist, is soaked in the acetone for ~1minute, followed by rinsing in acetone and isopropanol.

3.3 Sample characterization

In this section, we discuss the various tools, methods in detail, experimental setups to observe and analyze the SPB motions.

3.3.1 Scanning electron microscope

The scanning electron microscope (SEM) is a type of electron microscope that provides images of a sample by using a focused beam of electrons. Through the SEM, we know the topographic and compositional information of the sample surface. The Zeiss 982 SEM was used to characterize the structure of samples with both in-lens and secondary electron detectors at 2keV.

3.3.2 Superparamagnetic beads (SPBs)

Bead motion experiments were performed using commercially available SPB microbeads with several diameters: Dynabeads M-270 Carboxylic Acid with 2.8 μm diameter from Life Technologies, carboxyl magnetic 4.3 μm beads from Spherotech Inc., and COOH modified beads with 5.8 μm diameter from Bangs Laboratories. These beads are referred to as 2.8 μm, 4.3 μm, and 5.8 μm, respectively, throughout this thesis. In addition, diluted bead suspensions with DI water, where the concentration was down to 2×10^5 beads/mL were used in each experiment.

Before starting experiments with the SPBs, we measure the hysteresis loops of each bead batch with a Vibrating sample magnetometer (VSM). The coercivity of the SPBs obtained from

their hysteresis loops is 0.02 Oe, 2.5 Oe, and 4 Oe for 2.8 μm, 4.3 μm, and 5.8 μm, respectively. Even though the SPBs are not perfectly superparamagnetic behaviors, the general strengths of a rotating fields are much larger than the coercivity of the SPBs. Thus, we assumed that the SPBs can be considered as the superparamagnetic beads.

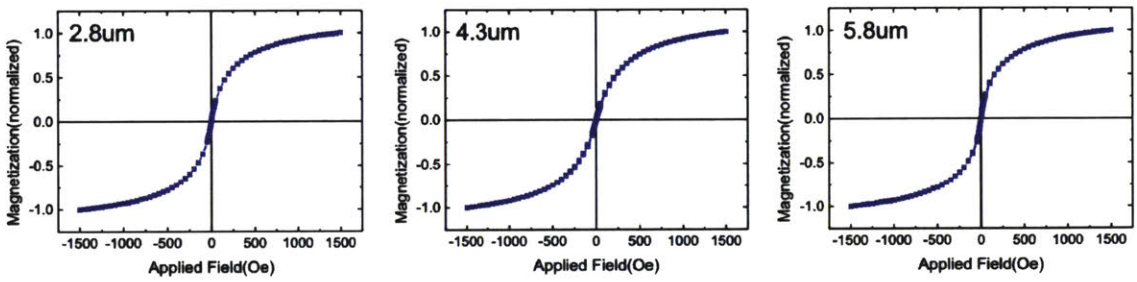

Figure 3-5 Hysteresis loop of each superparamagnetic beads: 2.8 μm, 4.3 μm, and 5.8 μm.

3.3.3 Sample preparation for bead motion experiments

The antidot patterns from lithography process or microsphere lithography were used as to transport the SPBs. As shown in Figure 3-6, dilute bead suspension was placed in a polydimethylsiloxane (PDMS) well on the wafer, and then sealed with a microscope cover slip. These samples were placed on a customized electromagnet that was composed of an out-of-plane field air coil and an in-plane field quadrupole magnet (Section 3.3.4). Before starting experiments, we applied a large H_{IP} to saturate the film magnetization and along a direction in the field-rotation plane, hence initializing the domain pattern. A rotating field was then applied and the bead trajectories were tracked in real time using a camera affixed to the microscope.

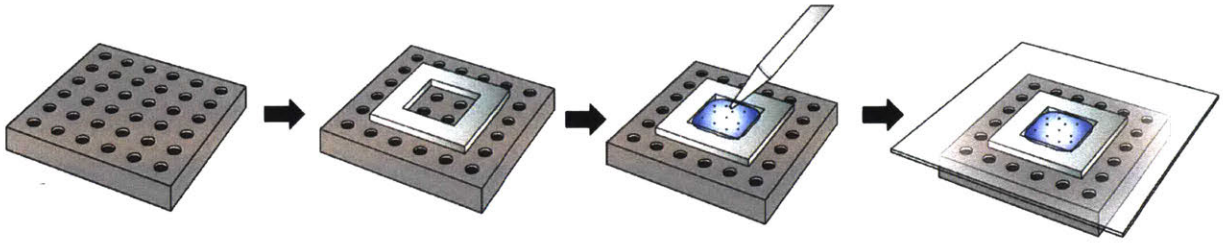

Figure 3-6 Sample preparation with suspension of magnetic beads

3.3.4 Customized electromagnet

In order to transport the SPBs, a rotating magnetic field in the *xz* plane was necessary. Thus, designing customized electromagnets were designed to provide a large and homogeneous rotating field with high bandwidth, with both in-plane and out-of-plane field direction. A large strength of the magnetic field is required to apply a magnetic field up to the coercivity of the samples, which is around 300 Oe. The homogeneity of a magnetic field is also important to ensure that the SPB transport is due to the superposition of the rotating field and stray field from the edge of the pattern. The customized electromagnet was composed of an out-of-plane field air coil and an in-plane quadrupole magnet as shown in Figure 3-7. The geometry of the customized magnet for the in-plane field allows the CCD camera to access the sample while the samples are located in the region of homogeneous field. The quadrupole magnet has two pairs, and each pair is driven by its own current channel. To generate a rotating magnetic field in *xz* plane, one channel of the in-plane magnet and the other channel connected to the out-of-plane field coil that are driven by sinusoidal current waveforms with 90° phase difference.

According to the Rapoport et al.[156], the quadrupole magnet is based on the iron powder cores from Micrometals (powder mix-26) to prevent losses at high frequencies. The magnet,

powered by two different power amplifiers (Crown DC-300A series) can generate in-plane fields of up to ~500 Oe and out-of-plane field of up to ~ 400 Oe. Furthermore, the magnet has a relatively high field-to-current ration of ~ 40 Oe A^{-1} and 28 Oe A^{-1} for in-plane magnet and out-of-plane field electromagnet, respectively. Due to these high ratios between field and current, we can apply rotating out-of-plane elliptical magnetic fields without overheating, which is one of serious problems in biological applications.

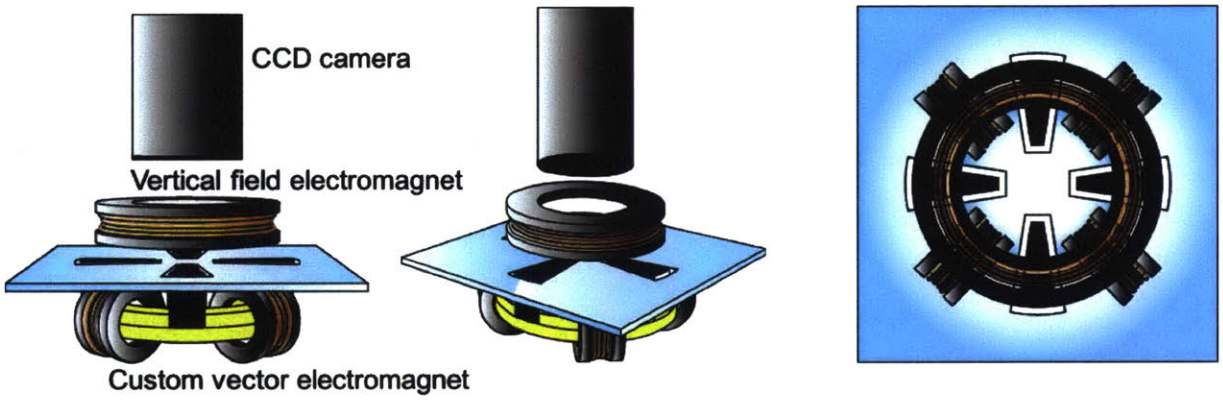

Figure 3-7 Vector electromagnet assembly Customized vector electromagnet with magnetic base and poles. Vertical field electromagnet integrated with optical imaging capability. Stage for sample mounting are indicated.

3.3.5 Optical observation in real time

SPB movement experiments are conducted by the rotating field in *xz*-plane through a programmed setup. During field rotation, the information related to the current amplitude, wave form, and frequency was delivered to the two channels of electromagnets: in-plane magnet and out-of-plane field electromagnet. Using the customized LabVIEW program, the specific field

information was supplied to bluebox and the dynamic response of the bead was observed using a home-built microscope integrated into the electromagnet stage setup. A CCD camera, which is fitted to a long working distance imaging microscope objective (Mitutoyo 10X M Plan APO), are used to track the bead trajectories in real time. The velocity of SPB movement were analyzed using a customized LabVIEW program with a pattern matching tool.

Chapter 4

Microbead transport on antidot arrays with in-plane anisotropy

In Section 2.2, we introduced the concept of superparamagnetic beads, which are subject to magnetic force when they are in a homogeneous magnetic field. Here, we discuss the transport of the SPBs based on a periodic micro-magnet array with a rotating magnetic field. We analyzed the transport behaviors on the antidot pattern, in which the magnetic moments are aligned in-plane and there is a highly localized stray field from the rims of holes.

The dynamics of the Superparamagnetic beads (SPB) transport using a rotating field in the *xz*-plane on the periodic micro-array is studied with analytical modeling and varying experiments. We first carefully investigate the relation between the velocity of SPBs and the frequency f of the rotating field. This relation is analyzed by the critical frequency phenomenon, which was previously reported by Yellen *et al.*[36]. We also examine the effect of applied fields on SPB motions to find new controlling parameters for SPB transport.

Finally, micro-magnetic simulations are used to explain and understand the experimental behaviors. We calculate the magnetostatic potential energy and magnetic interaction force from these experimental measurements, and figure out the origin of different behaviors according to the remanent magnetization, the diameter of beads, and symmetry of patterns. In chapters 5 and 6, we report additional experimental results that support the applicability of our findings to other a variety of geometric patterns.

4.1 Critical frequency behavior

As mentioned in the motivation, the transport of SPBs is on the basis of nonlinear magnetophoresis, which is the use of micropatterned magnetic substrates that lead to a periodic local stray field profile that can be modulated using an external magnetic drive field. In addition, the velocity of SPBs has a dependency on the rotational frequency f of the magnetic field. Yellen *et al.* previously reported that the SPBs' velocity linearly increased with f up to the critical frequency f_c, while the velocity of SPBs decreases above f_c[36].

We experimentally characterized the dynamics of SPB transport through an aqueous medium using a rotating magnetic field in the xz plane. The overall geometry of the transport of SPBs on the periodic square antidot patterns is illustrated in Figure 4-1. The blue arrow represents the amplitude of the out-of-plane field (H_{OOP}) and the red arrow shows the amplitude of the in-plane field (H_{IP}). The rotating field is elliptical in shape, and θ is defined as the angle with respect to the lattice principle axis.

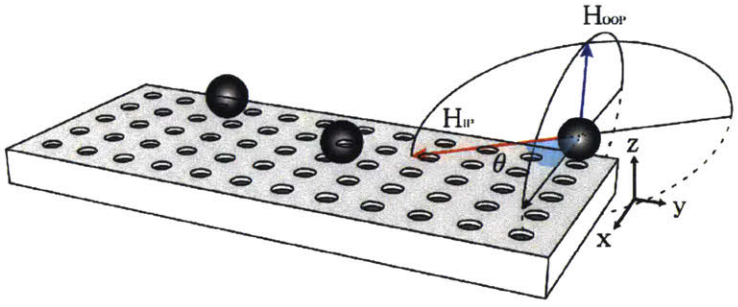

Figure 4-1 Schematic of the superparmagnetic bead motion experiments. The blue arrow represents the amplitude of the out-of-plane field H_{OOP} and the red arrow shows the amplitude of the in-plane field H_{IP}. The θ is the angle between the H_{IP} components and the x-axis.

Antidot arrays of 40 nm Co with 5 μm periodicity and 2.2 μm periodic holes were fabricated on a Si (100) wafer by a standard optical lithography (Section 3.2.2), sputter deposition (Section 3.2.3), and liftoff (Section 3.2.4). Before starting bead motion experiments, we applied a high H_{IP} (~300 Oe), to saturate the antidot film magnetization and along a direction in the field-rotation plane, hence initializing the domain patterns. Afterwards a dilute suspension of 2.8 μm diameter SPBs was placed on the wafer surface, as described in Section 3.3.3.

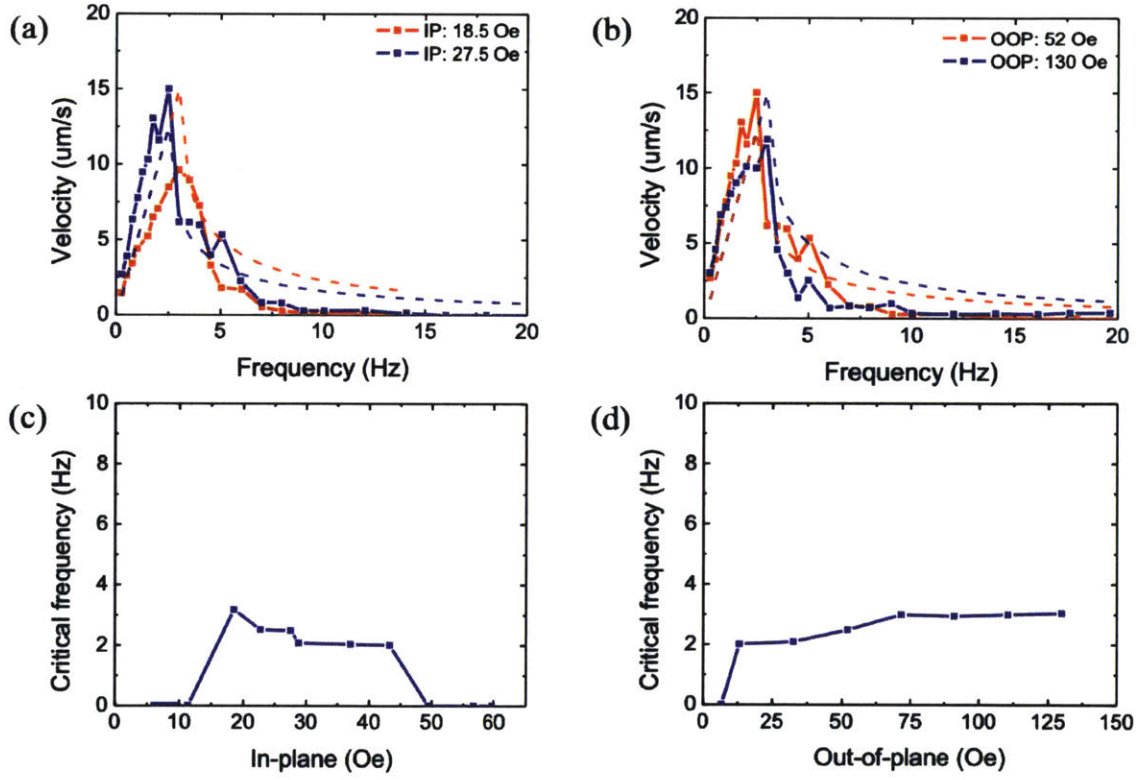

Figure 4-2 Velocity as a function of frequency for SPB diameter of 2.8 μm at (a) H_{OOP} = 52 Oe and H_{IP} = 18.5 Oe, 27.5 Oe. (b) H_{OOP} = 52 Oe, 130 Oe and H_{IP} = 27.5 Oe. The dashed lines represent the analytical model calculations for the 2.8 μm superparamagnetic beads. (c) Critical frequency as a function of H_{IP} at fixed H_{OOP} = 52 Oe (d) Critical frequency as a function of H_{OOP} at H_{IP} = 27.5 Oe with 2.8 μm diameter of SPBs.

Figure 4-2 (a) and (b) show the average velocity v of SPBs as a function of f for bead diameter d = 2.8 μm on the square lattice sample. With the field rotating in the xz plane. f varies from 0 Hz to 20 Hz at H_{OOP} = 40.5 Oe and H_{IP} = 27.5 Oe. Though the motion was more or less uniform for all beads in each experiment, surface adhesion causes a small fraction of beads to remain immobile; hence, we only consider measurement for those that have continuously moved for 10 sec. Fig. 2(a) shows v versus f at a fixed H_{OOP} and two different H_{IP} values, while Fig. 2(b) shows v versus f at fixed H_{IP} and two different H_{OOP} values. The results show similar behavior, with a linear increase of v with f up to a critical frequency f_c, followed by a drop off, as also reported previously in periodically-patterned substrates[36]. In addition, the linear behavior in v depends on the symmetry of pattern and the size of beads, and we will discuss this in Section 4.6 and 4.7, respectively.

Next, we analyzed the relationship between v and f, using a magnetophoretic transport model introduced previously[35-36,157]. The basic concept is that the rotating field causes a periodic rotation of the induced magnetization in the SPB, leading to a periodic potential landscape due to the magnetostatic interaction between the particles and the field gradients generated by the underlying substrate. In this model, the bead jumps from hole to hole along the pattern up to a critical frequency, beyond which the hydrodynamic drag begins to dominate and the bead position tends to oscillate in a local spatially-oscillating potential well rather than jumping form one well to the next. The average velocity in this model can be described analytically by[36]:

$$v = \begin{cases} \omega \frac{p}{2\pi} & for\ \omega \leq \omega_c \\ \left(\omega - \sqrt{\omega^2 - \omega_c^2}\right) \frac{p}{2\pi} & for\ \omega > \omega_c \end{cases} \tag{37}$$

where p is a center-to-center distance between adjacent magnetic features (holes), and $\omega_c = 2\pi f_c$ is related to the ratio of magnetic force to viscous drag.

We fitted the experimental data with Eq. (37) (dashed curves) showing that this model describes the bead transport well. In addition, the slope of the linear region is 5.5 μm for 2.8 μm SPBs, and these values are very similar to the predicted slope of 5 μm that is obtained from the p in Eq. (37).

Figures 2 (c) and (d) show the dependence of f_c on H_{IP} for fixed H_{OOP} (Fig. 2(c)) and on H_{OOP} for fixed H_{IP} (Fig. 2(d)), for beads with $d = 2.8$ μm. It is found that there is a sharp threshold for the amplitude of both field components, below which the beads are immobile, and above which the beads can be transported. Interestingly, f_c is independent of field amplitude above this threshold. However, there exists an upper threshold in H_{IP}, which occurs near the coercive field of the patterned film. This observation suggests that when H_{IP} exceeds this threshold, both the induced bead magnetization and the film magnetization (and resulting free pole configurations near the antidots) reverse sign together, so that the potential energy minima remain fixed in position rather than translating stepwise from one antidot edge to the next.

4.2 Critical threshold of magnetic field

In the section, we examine the effect of applied fields on SPB motions, because we might anticipate that there may also be other factors that can control the dynamics and could be utilized in multiplexed sorting operations. Figures 4-3 map out the field parameter space in which bead motion is observed, using a rotating field frequency of 1 Hz, which is below f_c, and varying the in-plane and out-of-plane field components. Results are shown for the transport of (a) 2.8 μm and (b) 4.3 μm SPBs. A blue circle indicates that most of the SPBs could be transported in each magnetic field combination, whereas a red cross indicates that the beads oscillate back and forth locally rather than exhibiting stepwise translation. Through this behavior, in order to transport the SPBs, we need to apply a quite strong magnetic field, of greater strength than the threshold values for both H_{IP} and H_{OOP}, and enough to overcome the friction forces, such as hydrodynamic force.

In addition, there exists an upper threshold in H_{IP} at 50 Oe. This is in contrast to H_{OOP}, which shows no upper threshold up to 140 Oe. The upper threshold in H_{IP} occurs near the coercive field of the patterned film, which is measured as 56 Oe through Vibrating sample magnetometer (VSM) measurement. This observation suggests that when H_{IP} exceeds this threshold, both the induced bead magnetization and the film magnetization (and resulting free pole configurations near the antidots) reverse sign together, so that the potential energy minima remain fixed in position rather than translating stepwise from one antidot edge to the next.

Unlike f_c, the working range (as represented the blue dot area) or the threshold values for both H_{IP} and H_{OOP} depend on the angle of H_{IP} and the size of the SPBs, and can also be used as the controlling parameters for the transport of the SPBs. We will discuss the details in Sections 4.5

and 4.7, respectively and we follow up with SPB sorting results that are based on the threshold values in the magnetic fields in Section 4.8.

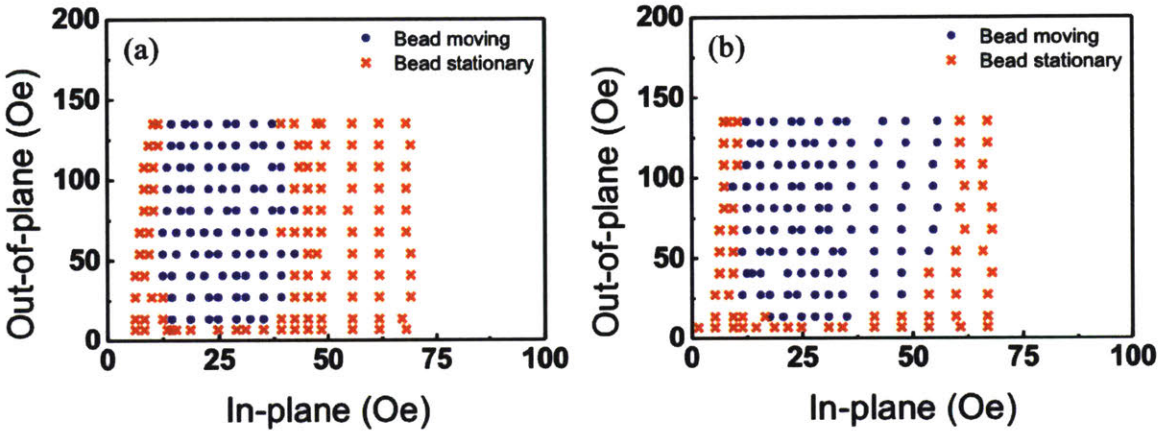

Figure 4-3 Critical threshold of H_{IP} and H_{OOP} for both (a) 2.8 μm SPBs and (b) 4.3 μm SPBs on the square antidot arrays that are magnetized along $\theta = 0$ °. The blue dot means that we can observe the bead transport and the red cross means that SPBs just oscillated back and forth.

4.3 Origin of the threshold behavior in the magnetic field

In Section 4.2, we showed that there are ranges of the capability to transport the SPBs. In this section, to understand the transport phenomena in more detail, we performed micromagnetic simulations of the magnetization patterns, and computed magnetostatic potential landscapes and magnetic interaction force, defined as the negative gradient of the magnetostatic potential energy.

In Figure 4-3, the antidot arrays cannot be used for bead motion beyond a maximum working field of H_{IP} (~50 Oe), corresponding approximately to the coercive fields of the respective systems. This can be explained by the magnetophoretic transport theory, which says that the minimum position of the potential energy landscape cannot be changed by applying the rotating field that exceeds H_c. Therefore, in the entire field from threshold H_{IP} up to H_c of each sample, the SPB motions are observed on the antidot arrays with in-plane magnetic anisotropy.

Figure 4-4 (a) shows the relaxed magnetization configuration and the energy surface for 4.3 μm SPBs on the antidot array, without the external rotating magnetic field. The energy surfaces landscapes are changed by applying the external magnetic field, so we calculated magnetostatic potential based on real experimental field parameters. In Figure 4-4 (b), we describe external field rotation angle θ for each computed magnetostatic potential landscapes.

Figure 4-4 (c) and (d) represent several cross-sections of potential wells for 4.3 μm SPBs on the square lattice at two different magnetic field conditions: the red cross and the blue dot in Figures 4-3 (b). The SPBs are located at the minimum position of the potential well, where the magnetic force vanishes and hence the bead is at an equilibrium position. The trajectory of the two minimum positions different behavior. In Figure 4-4 (c), the minimum position is slowly moving

to the right, but the position is hard to determine between 180° to 215° and it is divergent. This phenomenon is different from that in Figure 4-5 (d), in which the positions continuously move to the right. These graphs clearly show two different types of bead movements: transportation and oscillation. In addition, the magnetostatic potential well in Figure 4-4 (c) is shallow and it is insufficient to support the transport of SPBs when the magnetic field is below the threshold value. Otherwise, the magnetostatic potential well is deep and can provide the large magnetic force needed to move SPBs in the magnetic field that is described in Figure 4-4 (d). Thus, these graphs show why there are thresholds in the magnetic field.

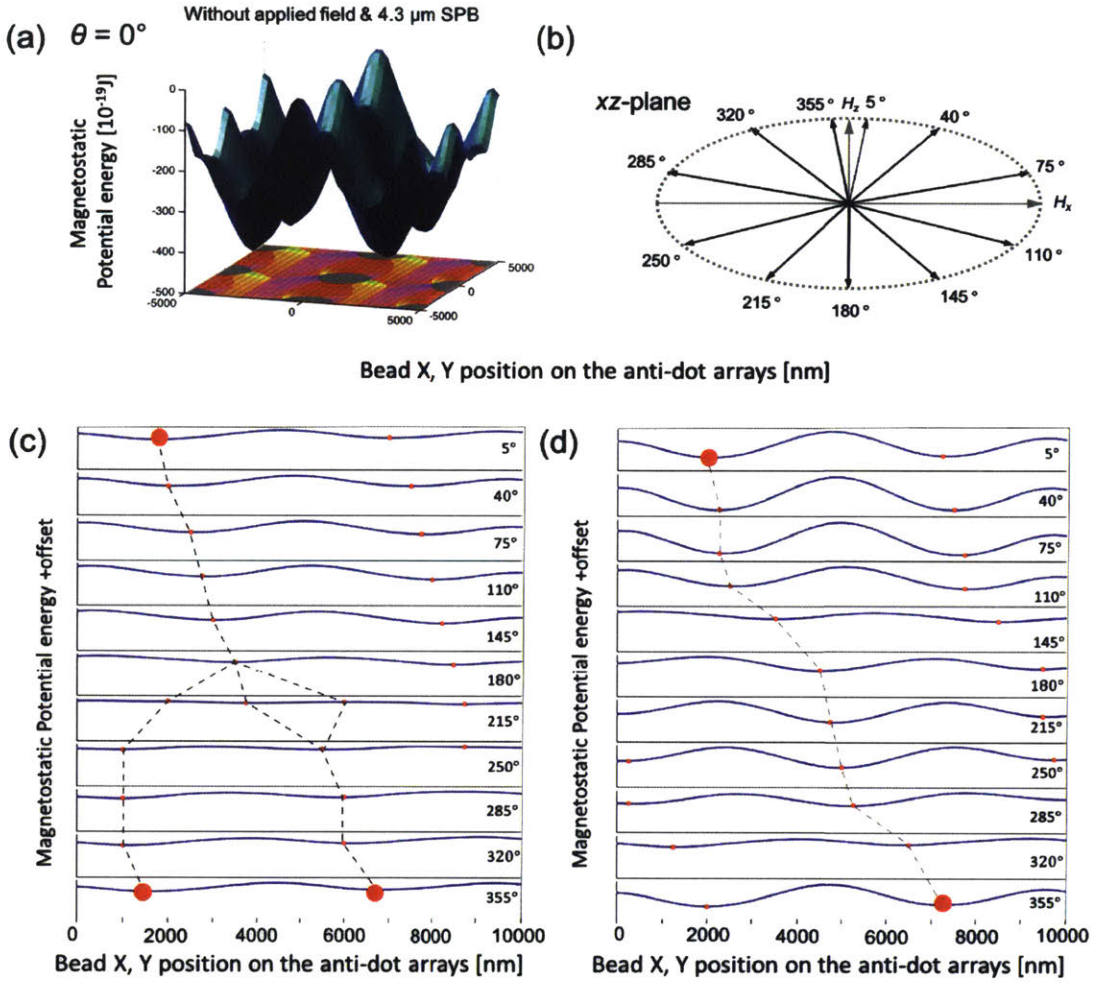

Figure 4-4 (a) The relaxed micromagnetically-computed magnetization configuration and magnetostatic potential well for θ = 0 °. (b) The rotating field in *xz* plane with each angle θ of a rotational period. The cross-sections of potential wells for 4.3 μm SPBs and minimum position (red circle) tracking at two different magnetic fields (c) below threshold (red cross) and (d) above threshold (blue dot) in Figure 4-3.

4.4 Magnetic anisotropy

We obtain the hysteresis loops of each symmetry sample using a vibrating sample magnetometer (VSM). For the square antidot array, the remanent magnetizations, which are represented as squareness M_r/M_s, have different values between 0.7 to 0.85. The square array has a fourfold anisotropy with the easy axes along the diagonal direction and the hard axes along the edge of the unit cell. By changing the lattice geometry from square to hexagonal, the fourfold symmetry is changed to six-fold symmetry. The easy axes are along the line connecting the centers of holes. The hard axes and the easy axes occur alternately every 30° for the hexagonal antidot arrays.

4.4.1 Remanent magnetic configuration

The remanent magnetization states were obtained after removal of a saturation field along the edge of the unit cell and diagonal direction, namely, $\theta = 0°$ and 45° for the square arrays and 0° for the hexagonal array. Even though we used the periodic boundary conditions, we consider the central area of the calculation regime. The simplified illustrations for the domains inside square and hexagonal unit cells are also shown in Figure 4-5.

For the square lattice, both the remanent states have periodic domain configurations and the directions of magnetization align along the rims of holes. The spin configuration is different from the blade domains, which are usually observed in the vicinity of holes[158]. These spin configurations of the square antidot arrays are the results of the minimization of the magnetostatic energy as well as the interaction between the holes. As shown in Figure 4-5 (a) and (d), the domain

configurations are roughly divided into three domains: One in which the spins point along the x-axis and two domains with diagonal spin orientations. When the field was applied along the 45° axis, the remanent spin configurations are divided into five domains, as shown in Figure 4-5 (b) and (e). Two domains with spins pointing along the x-axis and y-axis are formed to reduce the demagnetization energy from the edge of the holes. The 45° domains are nucleated due to the decrease in the associated magnetostatic energy. These configurations are similarly observed in other studies of micro-scale square antidot arrays[159-161].

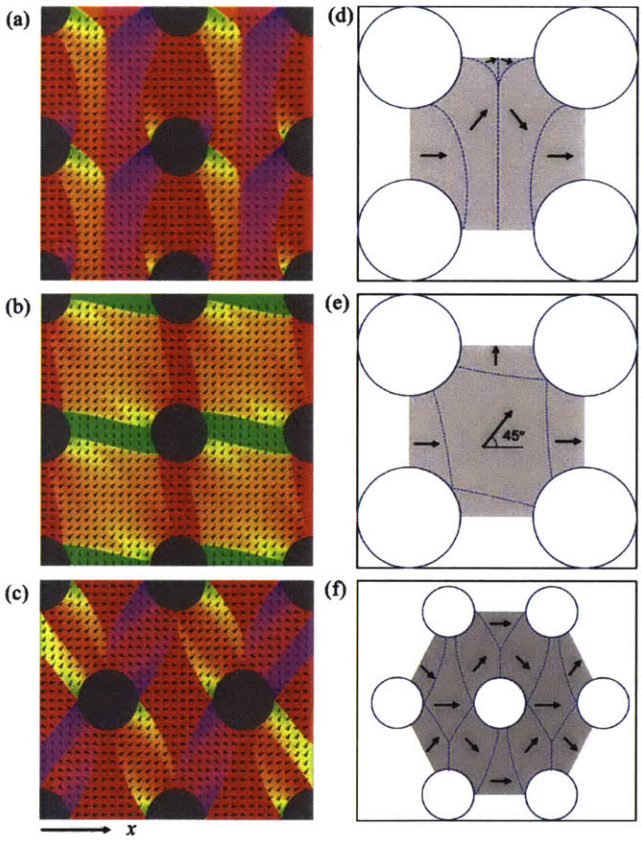

Figure 4-5 The remanent spin states in a unit cell captured from the micro-magnetic simulation and sketches of the domain wall distributions. (a) and (d) show the square array with a saturation field along 0°. (b) and (e) shows the square array with a saturation field along 45°. (c) and (f) show the hexagonal array with a saturation field along 0°.

The remanent spin state of the hexagonal array from the simulation result is shown in Figure 4-5 (c) and (f). The unit cell is divided into five microscopic domains, and the average spin configurations are aligned along the x-axis, which is the preferred direction of magnetization. Furthermore, the domains are classified as two groups. One group are those which have $\pm 30°$ to the x-axis. These domains are a result of shape anisotropy, which is imposed by the two nearest neighbor holes. Domains in the other group are magnetized along the x-axis, and the domains are usually observed to be the central regime among the four nearest neighbor holes. Even though those spin configurations cause a high demagnetization field, they remain and keep the 0° spin states. This phenomenon can be understood as reducing exchange energy, which is much larger than increase of the anisotropy energy. A similar phenomenon was observed by Wang[159] and the exact opposite result was found from the study on micro-size antidot arrays[162]. The discrepancy can be derived from the remanent domain configuration, which is directly correlated to the size of hole, periodicity, and packing fraction of the holes.

The domain structures are shown by the MFM images in Figure 4-6, which were taken at the remanent state after saturation along the easy axis direction. We acquired several images by varying the direction of the tip motion. As expected through the simulation, the MFM images display well-defined domain structures, which are periodic and connect each nearest neighbor hole. These results are properly fitted to the simulation results, which are shown in Figures 4-5 (b) and (c).

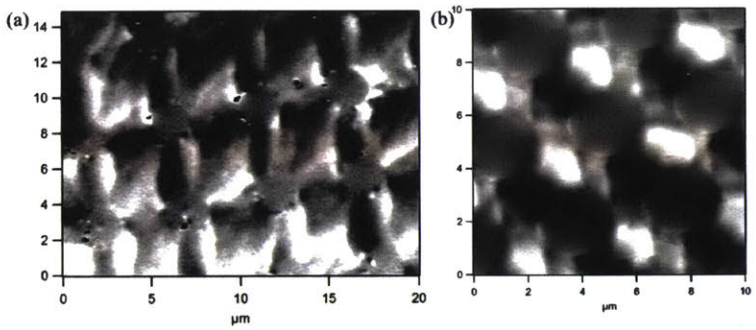

Figure 4-6 MFM images of the domain wall structure (a) on the square array (b) on the hexagonal array taken at the remanent state after saturation along the continuous easy axis.

4.5 Angle dependency along the direction of magnetization

Through the Sections 4.1 and 4.2, we showed that the f_c and threshold values in both H_{IP} and H_{OOP} can be controlling parameters for the SPB transport. In addition, the SPB sorting mechanism was demonstrated by the threshold value in H_{OOP}. In this section, these parameters have different values according to the remanent magnetization of periodic antidot arrays.

The square antidot array has different magnetization states when the substrate is magnetized along the edge of the unit cell and diagonal direction, namely $\theta = 0°$ and 45° (Section 4.4.1). The different relaxed magnetization configurations contribute distinct potential energy distributions.

The relaxed magnetization configuration after saturating the film along $\theta = 0°$ and $\theta = 45°$ with respect to the x-axis (principal direction) are represented in Figure 4-7 (a) and (b) respectively Figure 4-7 (a) and (b) also show the energy surface for 4.3 μm SPBs on the antidot array, without applying a magnetic field, for both the $\theta = 0°$ and $\theta = 45°$ cases, respectively. The direction θ of H_{IP} causes different remnant magnetic states, and the different states have a significant influence on the magnetostatic potential energy landscape. In the $\theta = 0°$ case, the potential wells are much deeper than in the $\theta = 45°$ cases, and the magnetic force in the $\theta = 0°$ case is likewise expected to be greater than in the $\theta = 45°$ case. In the $\theta = 0°$ case, the deep potential well can provide the large magnetic force needed to move SPBs and thus the beads can transport at the low magnetic field combination. The results clearly indicate that thresholds of H_{IP} and H_{OOP} are related to the magnetic force, and explain why both thresholds for the $\theta = 0°$ case are lower than for the $\theta = 45°$ case.

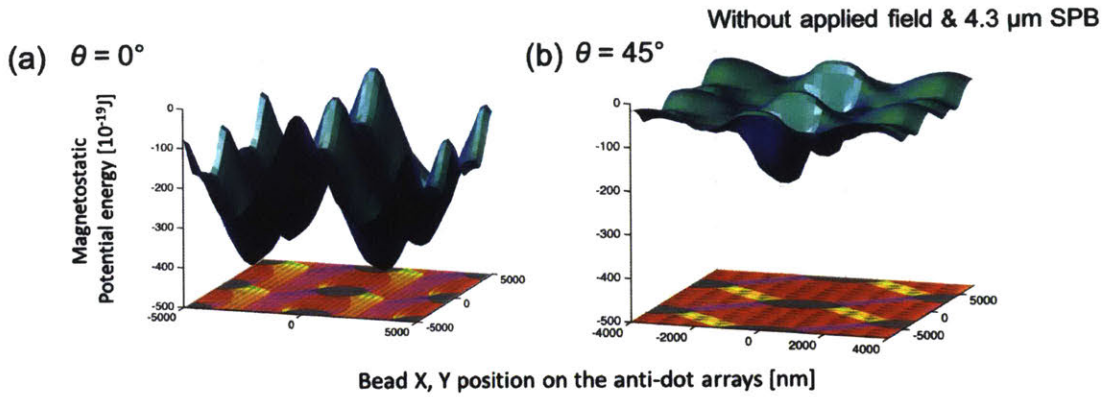

Figure 4-7 The relaxed micromagnetically-computed magnetization configuration and magnetostatic potential energy landscape for (a) θ = 0 ° (magnetized along the edge of unit cell) and (b) θ = 45° (magnetized along the diagonal direction).

Figure 4-8 (a) shows the SEM image of the Co antidot array with the average hole diameter of 2.2 μm and the periodicity (p) of the magnetic array scaled as 5 μm. The θ is the magnetization direction of the substrates in the θ = 45° and θ = 0° cases. Figure 4-8 (b) describes the linear behaviors in v of 4.3 μm, which depends on the angle of the magnetization direction of the substrates θ = 0° and θ = 45°. At H_{OOP} = 13.5 Oe and H_{IP} = 11.8 Oe, the behaviors of v in the linear regime have similar slopes of 4.65 and 5.66 for θ = 0° and θ = 45°, respectively. However, the f_c of the θ = 45° case is much lower than that of the θ = 0° case even though the experimental parameters such as substrate, the size of the SPBs, and the strength of magnetic field are the same. The opposite trend is observed at H_{OOP} = 13.5 Oe, H_{IP} = 17.8 Oe, where f_c of the θ = 45° case is much higher than that of the θ = 0° case. Therefore, the f_c can be greatly affected by the combination of the magnetic fields, and each case has an optimized magnetic field range.

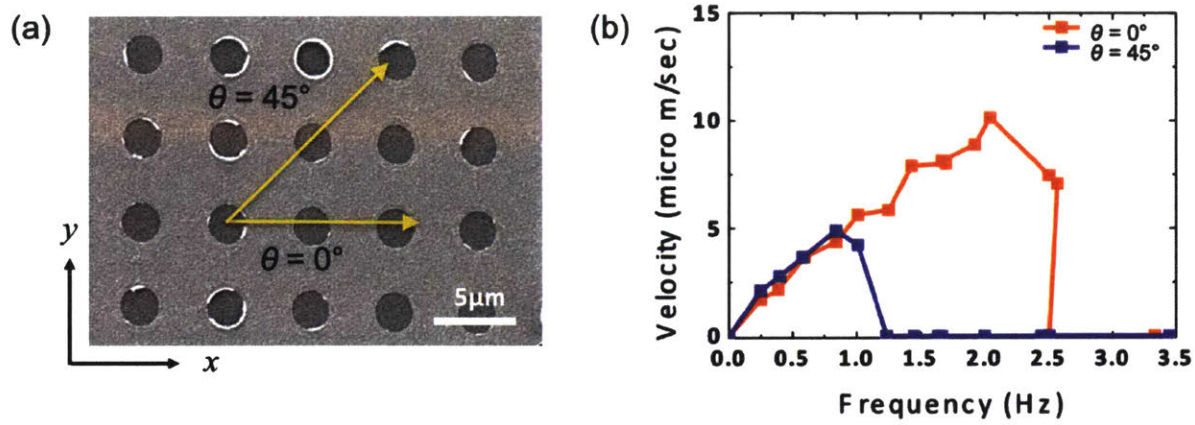

Figure 4-8 (a) Scanning electron micrograph images for Co antidot arrays. The average diameter of the periodic antidot array is 2.2μm and the periodicity of the pattern is 5μm. The θ is the angle between the H_{IP} component and the *x*-axis. (b) Velocity as a function of frequency at SPB diameter of 4.3 μm at H_{OOP} =13.5 Oe and H_{IP} = 11.8 Oe.

Figure 4-9 clearly shows both working ranges for the SPB motions as a function of applying the magnetic field components (H_{IP} as well as H_{OOP}) on the square antidot array at 1 Hz. As previously mentioned, the blue dot indicates that 90% of the SPBs are transported in each magnetic field combination, whereas the red cross indicates that SPBs are just oscillated back and forth. In both cases, the maximum values of H_{IP} for the SPBs transport are observed around 50 Oe, which is consistent with the H_c of the sample (as 50 Oe) via VSM measurement. However, the minimum magnetic fields in both H_{IP} and H_{OOP} that are needed to cause are much higher when the substrate is magnetized along the diagonal direction. This phenomenon can be explained by the magnetostatic potential well, in which the θ = 45° case has a shallower energy landscape. Underlying substrate, which was magnetized along θ = 45°, generated lower field gradient for travelling of SPBs, thus we need to apply more extra field to observe bead motions. Therefore, the threshold values in H_{IP} and H_{OOP} in the θ = 45° case are greater than those in the θ = 0° case.

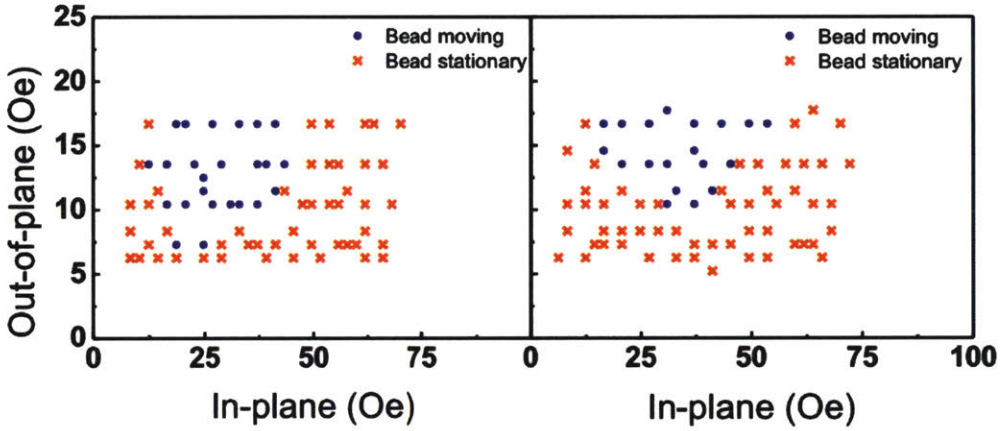

Figure 4-9 Critical thresholds of both H_{IP} and H_{OOP} for both $\theta = 0$ °(left) and $\theta = 45$°(right). The blue dot means that we can observe the bead transport and the red cross means that SPBs just oscillate back and forth.

4.6 Dynamics of beads depends on the diameter of bead

In Section 4.5, we describe the dynamics of SPBs depends on the direction of film magnetization, which is related to the micro-magnetic structures. In this section, we describe these dependencies of f_c and threshold values along with the size of SPBs.

Figure 4-10 represent the average-velocity v of SPBs as a function of the external driving f for bead diameters d= 2.8 μm and 4.3 μm on the square lattice sample. We applied f from 0 Hz to 20 Hz at fixed H_{OOP} = 52 Oe and H_{IP} = 18.5 Oe. The overall shapes of these plots are qualitatively similar; however, the drop-off in v above f_c is much less pronounced for the larger bead, whose diameter approaches the antidot lattice spacing, suggesting that another transport mechanism exists at higher frequencies, such as bead rolling. The f_c of each SPBs is 3.0 Hz and 2.5 Hz for 2.8 μm SPBs on square symmetry and 4.3 μm SPBs on square symmetry, respectively. Therefore, f_c has only a slight dependence on these parameters within the examined range.

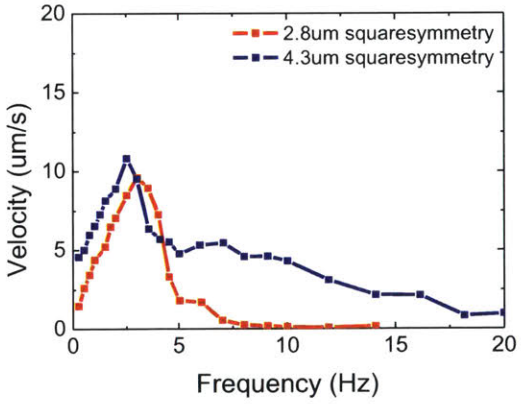

Figure 4-10 Velocity as a function of frequency at SPB diameter of 2.8 μm and 4.3 μm at H_{OOP} =52 Oe and H_{IP} = 18.5 Oe on the square antidot array.

Although f_c is rather weakly dependent on bead size, both H_{IP} and H_{OOP} represent the dependency along the size of SPBs. Figure 4-11 shows the working ranges for the transport of 2.8 μm SPBs and 4.3 μm of SPBs as a function of magnetic field components both on the square antidot arrays at 1 Hz. The dominant contribution to the very different critical field values is attributed to the bead size difference (possibly in conjunction with a different volume susceptibility due to different magnetic loading used by different manufacturers for theses bead varieties used). When comparing Figure 4-11 (a) and (b), the transport of 4.3 μm SPBs are generally observed in a wider range of applied fields.

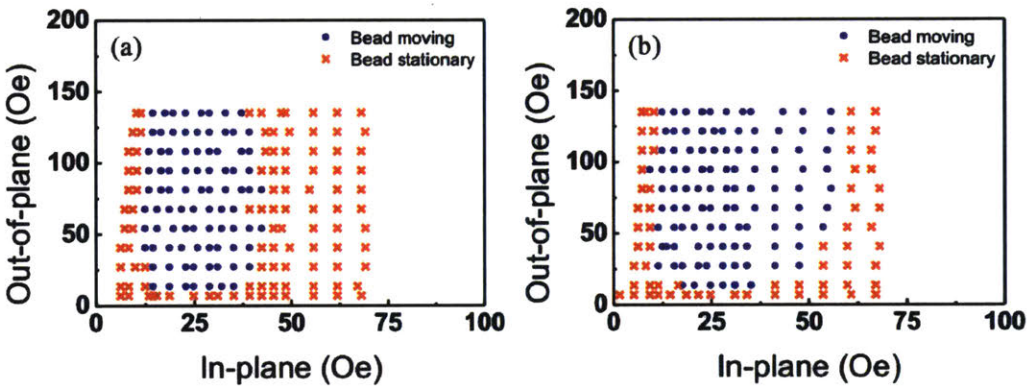

Figure 4-11 Critical threshold of both H_{IP} and H_{OOP} for both (a) 2.8 μm and (b) 4.3 μm on the square antidot array this is magnetized along $\theta = 0$ °

As previously represented, each different size of SPBs shows its own threshold values in both H_{IP} and H_{OOP}. To examine the d dependence on threshold, we calculated the magnetostatic potential energy landscapes for various d in Figure 4-12. The differences in potential energy shapes originated from the dissimilar magnetostatic interactions related to the diameter of SPBs. The depth of magnetostatic potential become deeper as the diameter d of SPBs increases, and the magnetic force acting on beads gradually strengthens with bead volume. Therefore, the local field

gradient and magnetic force for larger beads are greater than that for small beads at the same experimental procedure. Furthermore, this behavior agrees well with our threshold experimental results in which threshold in H_{IP} for 4.3 μm is lower than that for 2.8 μm in Figure 4-11.

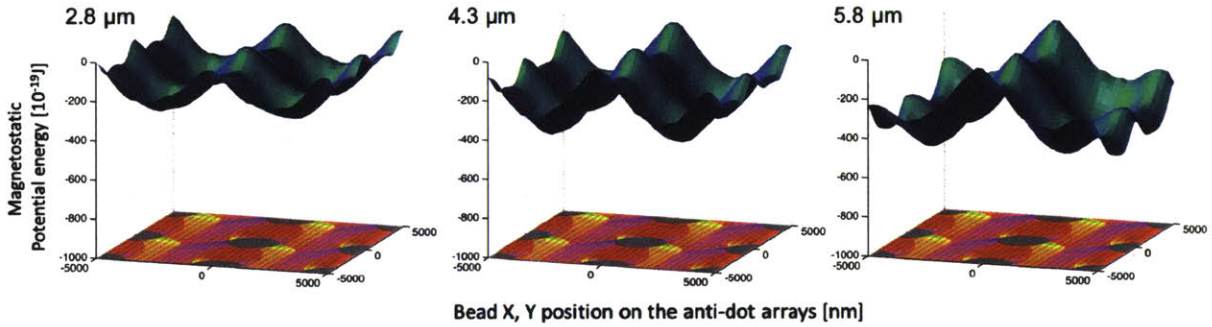

Figure 4-12 The relaxed magnetization configuration and magnetostatic potential energy landscape for 2.8 μm, 4.3 μm, and 5.8 μm SPBs

4.7 Distinct behavior of beads along with lattice geometry

In Section 4.5 and Section 4.6, we show that controlling parameters such as the f_c and threshold in both H_{IP} and H_{OOP} have dependency on the direction of magnetization and on the diameter of SPBs. Even though 2.8 μm and 4.3 μm SPBs have different surface coating and magnetic loading from different manufacturers, the dynamics of SPBs are significantly different behaviors along the size of SPBs. In addition, the relaxed micromagnetically-computed magnetization configurations are different along with the symmetry of antidot pattern (in Section 4.4), which leads to a significant influence on the magnetostatic potential energy landscape.

Given this dependency on the relaxed magnetic configuration, we suggested that the symmetry of antidot pattern can also modify the dynamics of SPBs even if the antidot arrays have same dimension parameter $\beta = d/2p$ (where d is diameter of beads and p is the center-to-center distance between adjacent magnetic features). Figure 4-10 represent v of SPBs as a function of f for $d = 2.8$ μm on the square antidot array and on the hexagonal antidot array. f is various from 0 Hz to 15 Hz at fixed $H_{OOP} = 6.5$ Oe and $H_{IP} = 19$ Oe. The maximum v and f_c of each case is 11.1 μm/s at 3.5 Hz and 9.2 μm/s at 2 Hz for the square array and the hexagonal array, respectively. Generally, the v of SPBs on the hexagonal array is slightly lower than that on the square array, including the maximum v at the same experimental circumstance.

However, the two curves are qualitatively similar, even though the relaxed magnetization configurations are significantly different. Thus, the dynamics of SPBs can slightly affected by the difference in remnanet magnetization configuration, whereas the periodic arrays with PMA have

quite different trajectory of the SPB movement. Nevertheless, the f_c is varying along with the symmetry of patterns and the properties can be used for the SPB sorting.

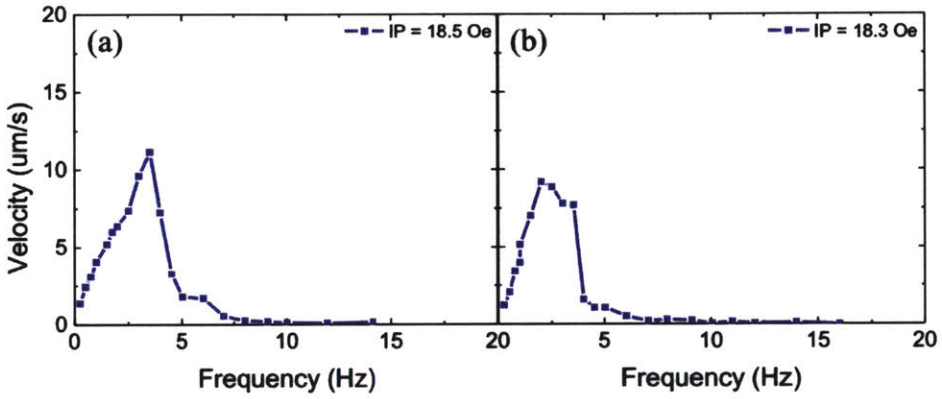

Figure 4-13 Velocity as a function of frequency at SPB diameter of 2.8 μm at H_{OOP} = 6.5 Oe and H_{IP} = 18.5 Oe and 18.3 Oe (a) on square lattice and (b) on hexagonal lattice.

Unlike the critical frequency, the dependency along the symmetry of array was observed in the threshold values in both H_{IP} and H_{OOP} as shown in Figure 4-11. Figure 4-11 represents the working ranges for the transport of 2.8 μm SPBs as a function of magnetic field components: H_{IP} and H_{OOP} on (a) the square antidot array and (b) the hexagonal antidot array at 1 Hz which is below f_c. Compared to Figure 4-11 (a) and (b), the transport of 2.8 μm SPBs on the square antidot array are generally observed in a wider range of applied fields. The SPB transport on the square antidot array has lower threshold values both in H_{IP} and H_{OOP}. In addition, as discussed in Section 4.2, both cases have a maximum working field of H_{IP}, which is corresponding approximately to the H_c of the substrate. Thus, dynamics of SPBs on the square antidot array are more easily observed than

on the hexagonal antidot array, which is the reason why we mainly conducted research with antidot arrays with square symmetry.

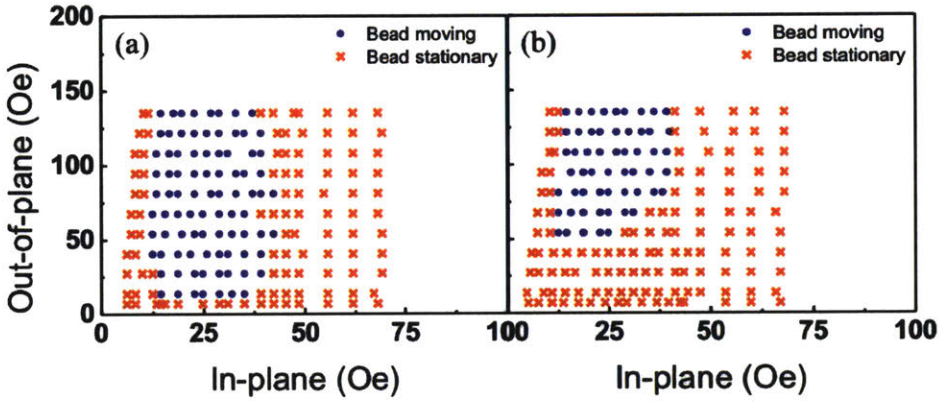

Figure 4-14 Critical threshold of both H_{IP} and H_{OOP} with 2.8 μm for both (a) square lattice antidot array that is magnetized along θ = 0 ° direction. (b) hexagonal antidot array that is magnetized along θ = 0 ° direction. The blue dot and the red cross show the bead moving and bead stationary, respectively.

4.8 Bead separation

Bead separation is a typical bioanalytical technique, and the demand for new higher efficiency technologies is greatly increasing. Nano- and micro-sized SPBs with functionalized surfaces are widely used to separate and detect biological entities from complex samples in bioanalytical systems[115, 119].

The antidot arrays provide a means for separating in a large volume and the separation can be achieved by various channels such as the f_c and threshold both in H_{IP} and H_{OOP}. In the previous section, we find that the f_c and the field, H_{OOP} as well as H_{IP}, play crucial roles in triggering bead movements. Thus, in this section, the threshold values in H_{OOP} and H_{IP}, below which the beads cannot move, can be used in bead separation as controlling parameters.

Based on the observation that the critical field thresholds depend on bead size, one can use this phenomenon as a means to sort multi-bead mixtures of monodisperse beads with different sizes using an appropriately chosen rotating field. Figure 4-15 shows sequential snapshots taken every 2 seconds on the square antidot array shown in the case of a rotating field applied in the *xz* plane. Here, a mixture of 2.8 μm and 4.3 μm diameter SPBs was placed on the substrate, and the field amplitudes were chosen to be intermediate between the transport thresholds for these two bead sizes. The frequency of the driving field is about 1 Hz, and it is below the f_c of both sizes of SPBs. When the magnetic field is applied at a specific value that is higher than the threshold H_{IP} for 4.3 μm (circles) and lower than that for 2.8 μm. Thus, we can see that 4.3 μm SPBs are transported, whereas SPBs 2.8 μm simply oscillated back and forth. This demonstrates that the SPBs can be sorted through their own threshold values in the magnetic field.

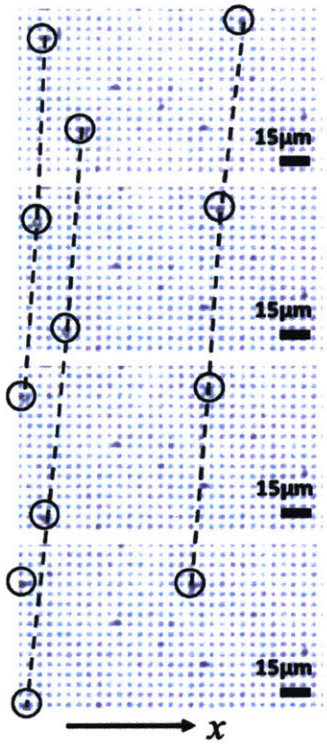

Figure 4-15 Optical microscopy images showing a series of SPB movement snapshots taken every 2 seconds with 2.8 μm beads indicated as small black dots and 4.3 μm beads as circles when the field (H_{IP} = 12 Oe and H_{OOP} = 27 Oe) is rotating counterclockwise at 1 Hz.

4.9 Summary

In summary, we have studied the motion of fluid-suspended SPBs across a well-ordered magnetic structure consisting of periodical two-dimensional lattices of holes in a magnetic film. Our experiments have revealed critical frequencies and related threshold values in both H_{IP} and H_{OOP}. We determined that these thresholds are related to the depth of magnetostatic potential and find a dependence on bead size and substrate periodicity, and have explored these parameters experimentally and through modeling. Finally, we demonstrated that these parameters have different values according to the magnetized direction, the symmetry of pattern, and the diameter of the SPBs and that they can be used for the SPB separation in multi-bead populations. These findings suggest the feasibility of a new method for sorting magnetic objects.

Chapter 5

Micro-magnetic architectures based on the microsphere lithography

In Section 4, we discussed about the SPB transport on the antidot arrays with in-plane magnetic anisotropy. We found that a critical frequency and the fields H_{OOP} and H_{IP} play crucial roles in triggering bead movements, and the threshold values in H_{OOP} and H_{IP} is dominant of bead separation as controlling parameters. Furthermore, our experimental results, especially the origin of thresholds in a magnetic field, are well reproduced by the micro-magnetic simulation.

In this section, we perform an extended work done in previous chapter so that we focused on different antidot arrays for SPB transport measurement through a simple, cost-effective method. First, similar to previous work, our controlling parameters such as f_c and threshold values in H_{OOP} and H_{IP} can be also applied to the entire ratio of Superparamagnetic beads (SPBs) to patterns. Second, we clarified the different sizes of the SPBs through a simple sorting mechanism based on the threshold values in a magnetic field.

5.1 Critical frequency

Figure 5-1 represents the depth of the magnetostatic potential well as a function of the ratio of diameter to periodicity (d/p), obtained from the micro-magnetic simulations. At low ratio

regime, where the period of the antidot array is larger than the diameter of SPBs, the magnetic force acting on the SPBs gradually strengthens as the diameter of SPBs increases up to a maximum, and then decreases with further increase in d/p. This can be understood in the limits: at small bead diameter, the magnetic potential decreases rapidly with bead volume. However, as the bead diameter becomes much larger than the feature size on the substrate, stray fields from adjacent holes are integrated over the bead volume, "smearing" out the potential. The numerical results suggest the existence of an optimum ratio for d/p, in the present case corresponding to ~2.4.

The aforementioned f_c and the thresholds both in H_{IP} and H_{OOP} (Section 4), are related to the small ratio of d/p (d is the diameter of the SPBs and p is the distance from center to center). Through several experiments with various SPBs and other antidot patterns, we have also determined that there are f_c and threshold H_{IP} and H_{OOP} at the large ratio of d/p.

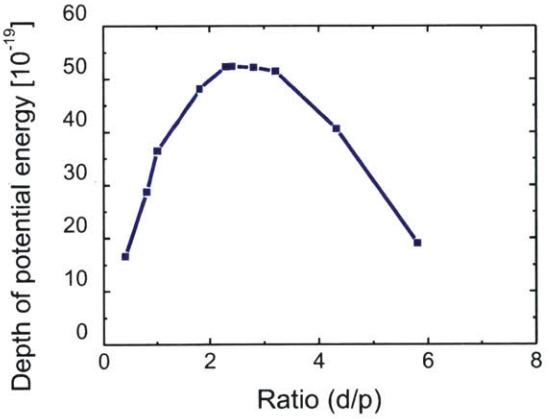

Figure 5-1 The depth of the magnetostatic potential well dependence on the ratio of the diameter and periodicity.

Figure 5-2 shows the v as a function of f for d 2.8 μm on a different antidot pattern where average hole diameter is 0.78 μm and p = 1 μm. f varies from 0 Hz to 10 Hz at H_{OOP}: 17 Oe and

H_{IP}: 55 Oe. The result shows qualitative similar as seen in Figure 4-2, and f_c presents around 1.75 Hz. The dashed line represents the time-averaged velocity defined by Eq. (37). However, the fitting is not well agreed with the experimental data, despite of similar slopes obtained from experimental and analytical results. By considering the trajectory of SPBs on the antidot pattern, the SPB transport does not hop or jump from one hole to another hole. Because the p of the antidot pattern is much smaller than that of the d of the SPBs, the SPB traveling is influenced by several holes on the patterns instead of just one hole. Based on this scenario, the experimental result is considered, combining the effect of holes on the pattern.

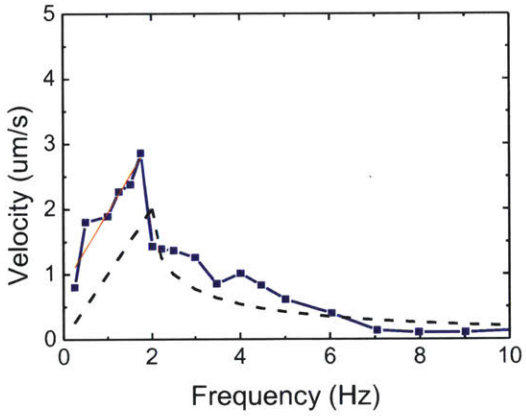

Figure 5-2 Velocity as a function of frequency with an SPB diameter of 2.8 μm at H_{OOP} =16.5 Oe and H_{IP} = 54 Oe.

5.2 Field threshold

We also examine the effect of applying a field on SPBs' motion in Figure 5-3 (a) and (b). Figure 5-3 shows the f_c as a function of (a) H_{IP} under H_{OOP} = 8, 10, 11 and 12 Oe and of (b) H_{OOP} under H_{IP} =48.4 Oe for d = 2.8μm. As shown in Figure 5-3 (a), f_c varies in the range from 20 Oe to ~ 80 Oe and is independent of the applied field, whereas this behavior was not observed with applied field H_{OOP} = 8 and 10 Oe. In Figure 5-3 (b) fc is also found to drastically enhance with H_{OOP}, indicating that the transport of SPBs can only be driven above certain H_{OOP} values. Therefore, these two figures are obvious evidence that each H_{OOP} and H_{IP} is the threshold values for triggering SPB movements, taking the values of H_{OOP} = 10 Oe and H_{IP} = 13 Oe. On the other hand, unlike field threshold, f_c is interestingly independent of field amplitude above the threshold.

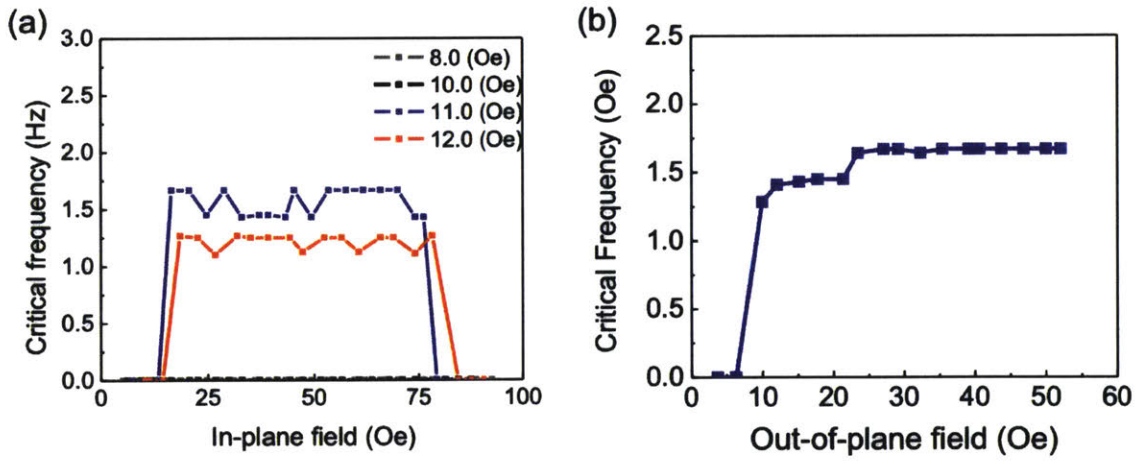

Figure 5-3 The critical frequency as a function of (a) in-plane field under out-of-plane field and (b) out-of-plane field under In-plane field with a 2.8μm SPB diameter.

5.3 Bead separation

As in the previous case, f_c and threshold values in both H_{OOP} and H_{IP} depend on the size of SPBs (d) (Section 4.1 4.2, and 4.7). To examine the d dependence on threshold, we carried out the same experiments with various d of SPBs.

First, the micro-magnetic simulation along the size of the SPBs shows the opposite trend to that described in Section 4.2 and 4.7. Figure 5-4 represents the relaxed magnetic configuration of a hexagonal anti-dot array and magnetostatic potential wells computed for several values of the ratio d/p of bead diameter to center-to-center spacing of the antidot lattice. Calculations are shown for d/p values of 0.4, 2.4, and 5.8. The shape of the potential well depends on the ratio, and the depth of potential well is shallow at both the low ratio and the high ratio limits. As the diameter of SPBs increases, the depth of the potential well is shallower and the SPB transport cannot be effectively supported by the stray field from an individual hole of the pattern. Therefore, the threshold values in both H_{IP} and H_{OOP} will be greater as the d of the SPBs increases. The discrepancy between experimental results and micro-magnetic simulations can be explained by the fact that, at large ratio of d/p, the superposition of traveling potential landscapes influences on the dynamic of SPBs, and other factors such as the surface coatings and magnetic materials of SPBs can also contribute to the behavior of SPB transport.

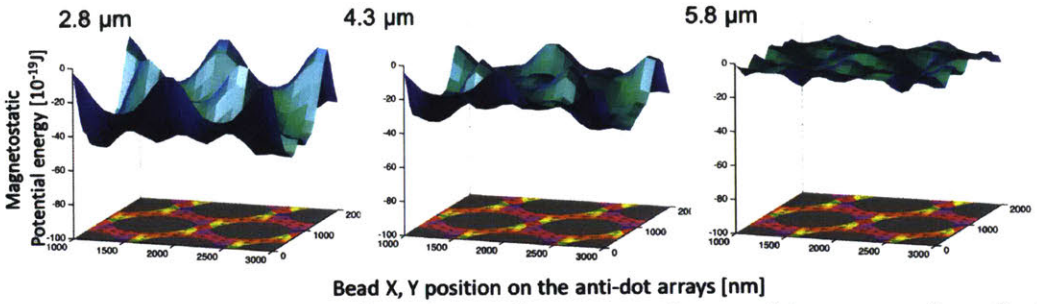

Figure 5-4 Relaxed magnetization configurations and magnetostatic potential energy surfaces for 2.8 μm, 4.3 μm, and 5.8 μm SPBs

Nevertheless, the distinct threshold of the H_{OOP} can be used as the controlling parameter for the transport of SPBs, and we showed that it could be applied to the SPBs' separation. Figure 5-5 (a) shows a scanning electron micrograph of a 40nm-thick Co layer patterned into a hexagonal antidot array with p = 1 μm and hole size of ~0.8 μm. This pattern was formed by microsphere lithography, where monolayer ordered arrays of polystyrene microspheres were used as a lithography template. The diameter of polystyrene particles is 1 μm and reactive ion etching was conducted to tailor spacing sizes before depositing the thin-film over layers.

Figure 5-5 shows that bead transport and size-based separation can be achieved reliably on this substrate, where we examine the rotating-field-driven motion of 2.8 μm and 5.8 μm beads. As anticipated from the simulations summarized in Figure 5-1, we find similar critical frequency and field behavior in the transport behaviors for the large d/p limit that is applicable for the experimental case examined here (Section 5.1). As in the previous Section 4.7, f_c and threshold values in both H_{OOP} and H_{IP} depend on the size of SPBs d. To examine the d dependence on the threshold, we performed similar experiments as above to identify the field thresholds and critical frequencies (Section 5.2). As shown in Figure 5-5 (b), f_c is located around 1.5 Hz and 2.5 Hz for 2.8 μm and 5.8 μm, respectively. In the case of H_{OOP}, the thresholds are found to be 11 Oe and 8

Oe for 2.8μm, and 5.8μm, respectively. Thus, the f_c as well as the threshold of the H_{OOP} can be used for selective transport of one subpopulation of SPBs. Figure 5-5 (c) shows snapshots during bead transport, in which size-based sorting on the microsphere lithograph-patterned substrate is achieved by tuning H_{OOP} to a value intermediate between the thresholds for the two bead sizes. As is evident in the images, the larger beads can be transported reliably along the x direction while the smaller beads remain stationary.

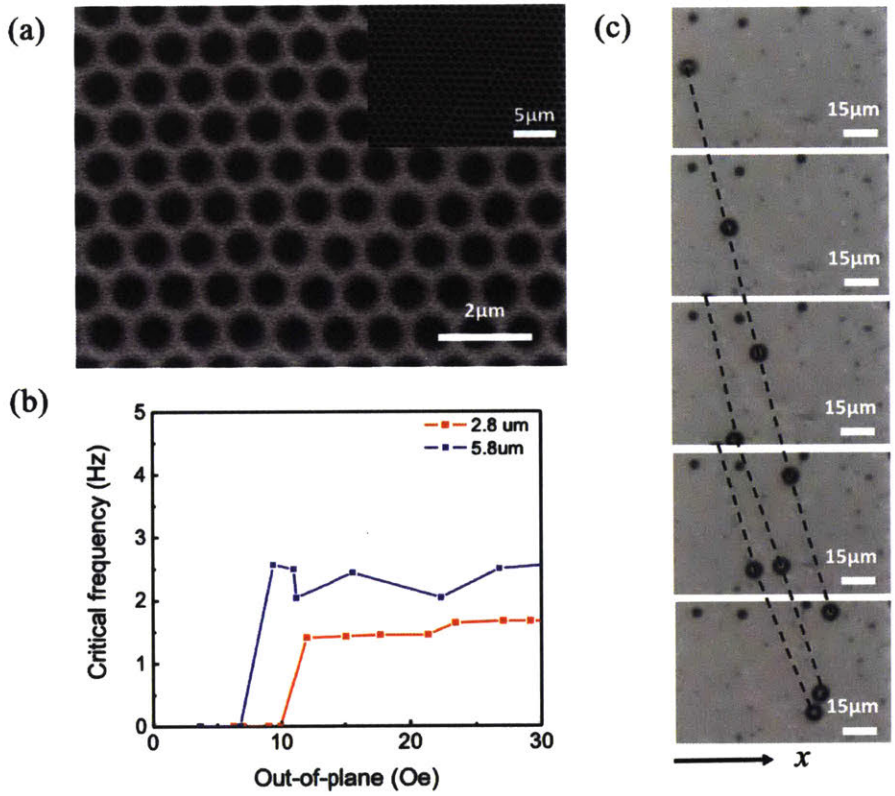

Figure 5-5 (a) Scanning electron micrograph for a Co anti-dot arrays fabricated through microsphere lithography. The average diameter of the periodic anti-dot array is ~0.8μm and periodicity of array was 1μm. (b) The critical frequency as a function of H_{OOP} at H_{IP} = 48.4 Oe with 2.8 μm and 5.8 μm of superparamagnetic beads. (c) Series of optical microscopy images of SPB movement showing snapshots acquired every 2 second with 2.8 μm beads and 5.8μm beads when the rotating magnetic field (H_{IP} = 48.4 Oe and H_{OOP} = 9 Oe) in the clock-wise direction at 1 Hz.

5.4 Summary

Through a simple patterning method such as floating transferring technique (Section 3.2.1), we produced well-ordered magnetic patterns. At a high ratio of d to p regime, we also demonstrated that controlling factors for the dynamics of SPBs such as f_c and thresholds in both H_{IP} and H_{OOP} are observed. Therefore, our findings apply to the entire range without consideration for d of SPBs and p of patterns. Finally, we show that these parameters have different values according to the diameter of SPBs and can be used for SPB sorting. Therefore, we show that a simple, inexpensive large-area patterning can be achieved using self-assembled microsphere lithography to prepare antidot arrays that can be used for bead transport and separation

Chapter 6

Microbead transport on antidot of Co/Pt multilayer substrates

In Section 4 and Section 5, the antidot magnetic patterns have had in-plane magnetic anisotropy. Therefore, we had to consider the relaxed DW configuration in experimental results and micro-magnetic simulations. As shown in Section 4.5 and Section 4.6, these DW configurations definitely affected the Superparamagnetic bead (SPB) transport.

In this section, we focus on developing a new structure to improve the dynamics of SPBs and consider a multilayer structure with perpendicular magnetic anisotropy (PMA). Through micro-magnetic simulation, we confirm that the SPBs can obtain a relatively high stray field from the magnetic antidot array with PMA. In addition, PMA material used here is in single domain state therefore the DW configurations do not need to be considered. The magnetic antidot array in a multilayer structure with PMA usually has a large H_c, which corresponds to the maximum magnetic fields for the SPB motions (Section 4.2).

We first discuss the optimization process of the multilayered structure with varying thicknesses of Co and Pt to obtain PMA, in order to use it for the SPB transport. Then, enhanced dynamics of SPBs on the antidot array with PMA are demonstrated through be more explicit here.. Numerical analytical modeling explains the dynamics of SPBs on each geometry of antidot patterns. Furthermore, we demonstrate that the large external field threshold values on PMA

substrates can provide broader working range in terms of magnetic fields to transport SPBs, thus increasing flexibility in device applications using the transport of magnetic particles.

6.1 Optimization of Co/Pt multilayer structure

The Co/Pt or Co/Pd multilayers have been widely studied since they were first observed.[101,102] The large spin-orbit coupling at the ferromagnetic-nonferromagnetic (FNF) interfaces lead to perpendicular magnetic anisotropy (PMA). The magnetization pointing out of the film plane in equilibrium lead to high stray fields on the surface of the PMA substrate. Moreover, patterning to the PMA substrates (i.e. shrinking the lateral size of each magnetic entity) results in increasing the coercivity (H_c). This can be understood from the fact that the small area reduces the chances of nucleation, making switching of the first domain difficult.[163] Thus, to enhance the transport of the SPBs, we optimized the Co/Pt multilayer structure to be in a single domain state in the absence of the external field and have a high H_c.

We first optimized the PMA in a single Co layer sandwiched between two Pt layers by varying the Co thickness. All metallic layer was deposited by a 4-target DC/RF magnetron sputtering (Section 3.2.3). Figure 6-1 represents several hysteresis loops of continuous films of Ta (4nm)/Pt (5nm)/Co (t)/Pt (5nm) with varying thicknesses of Co. Ta was deposited as a seed layer. Considering the squareness (M_r/M_s) and the large H_c, 1 nm of Co was the optimal thickness for developing a multilayer structure.

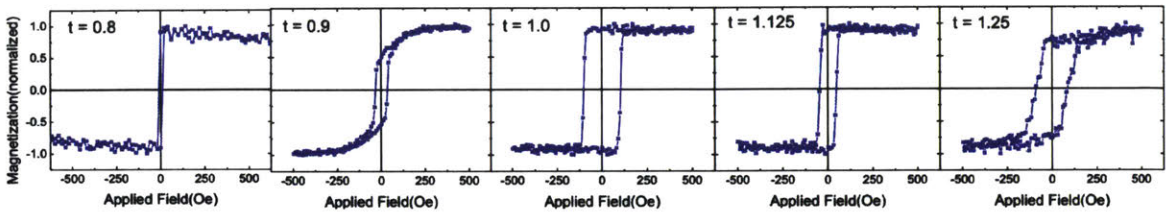

Figure 6-1 Hysteresis loop of continuous samples with Co (t nm)/Pt (5 nm)

The thickness of Co was fixed as 1 nm; then Pt thickness dependence was studied through the structures of the type Ta(3 nm)/Pt(5 nm)/[Co(1 nm)/Pt(t nm)]$_5$ multilayers. Several hysteresis loops are shown in Figure 6-2, and the H_c is generally larger in the multilayers than in single Co layer. The large H_c and high squareness can be observed between t = 5.5 nm and t = 6.5 nm. Therefore, antidot pattern arrays with the structure of Ta (3 nm)/Pt (5 nm)/[Co (1 nm)/Pt (4 nm – 6.5 nm)]$_5$ were prepared.

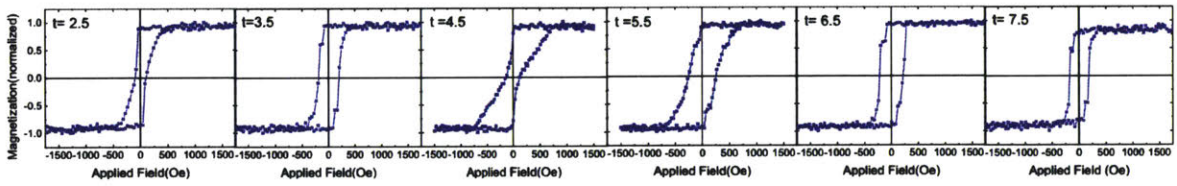

Figure 6-2 Hysteresis loops of continuous films with [Co (1 nm)/Pt (t nm)]$_5$

As shown in Figure 6-3, the optimized Pt thickness of the antidot array is slightly different from that in continuous film. The maximum H_c and high M_r/M_s (squareness) among several antidot patterns is observed at 4.5 nm of Pt. Therefore, we choose the coupled structures of the type Ta(3)/Pt(5)/[Co(1)/Pt(4.5)]$_x$ (for square lattice) and Ta(3)Pt(5)/[Co(1)/Pt(5)]$_x$ (hexagonal lattice) multilayers, where x is the stacking number (x=5) and thicknesses in brackets are in nm. Before

starting experiments, the hysteresis loops with an out-of-plane field sweep (H_{OOP}) that measured by a Vibrating sample magnetometer (VSM) show square loops with respect to the H_{OOP} direction, confirming that they exhibit PMA.

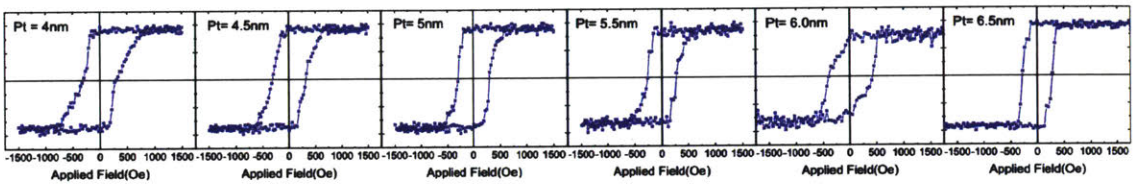

Figure 6-3 Hysteresis loops of antidot arrays with [Co (1 nm)/Pt (t nm)]$_5$

6.2 Enhanced dynamics of superparamagnetic beads

Through Sections 4.1 and 5.1, we demonstrated that SPBs can freely move on the antidot arrays by applying a rotating magnetic field. On these substrates, the maximum v, which depends on the f_c, is usually up to 15 μm/secs and it is much slower than that of SPB transport based on a flowing solution or a domain wall motion. Thus, to improve the dynamics of SPBs on the antidot arrays, we consider the multilayer structure with PMA.

In this section, we show the enhanced dynamics of SPBs on the antidot arrays and analyze the behavior of SPBs based on the micro-magnetic simulation and magnetophoretic transport modeling. Finally, we represent the different behaviors of SPB movement according to the symmetries of patterns.

6.2.1 Enhanced dynamics of SPBs on the antidot array with PMA

Figure 6-4 describe average velocity of SPBs v as a function of frequency at SPB diameter of 4.3 μm at H_{OOP} = 13. 5 Oe and H_{IP} = 8.3 Oe, 11.8 Oe, and 43. 2 Oe on two different square antidot arrays: with (a) PMA and (b) in-plane anisotropy. To make a comparison on an equal basis, we only consider measurements for the SPB motions that have continued for 10 seconds. As shown in Figure 6-4 (a), the v as a function of f represents a similar trend and has the f_c, which is illustrated in Sections 4.1 and 5.1. At low frequency, almost all SPBs are transported and the v of SPBs linearly increases up to f_c. However, when f is significantly above f_c, the SPBs are immobilized and they only move back and forth. The maximum v is observed when f reaches to the f_c at each magnetic field combination and the f_c varies along with the strength of the magnetic field. Note

that the overall f_c is higher on the antidot arrays with PMA. Therefore, the maximum v is generally higher than that on the magnetic antidot with in-plane anisotropy. For example, the v of SPBs on the multilayer with PMA is 18 μm/s at H_{OOP} = 13. 5 Oe and H_{IP} = 43.2 Oe, whereas the v of SPBs on the array with in-plane anisotropy is 5 μm/s. These results show that rapid dynamics of SPBs can be simply achieved on an antidot array with PMA, as expected from effective pole distribution.

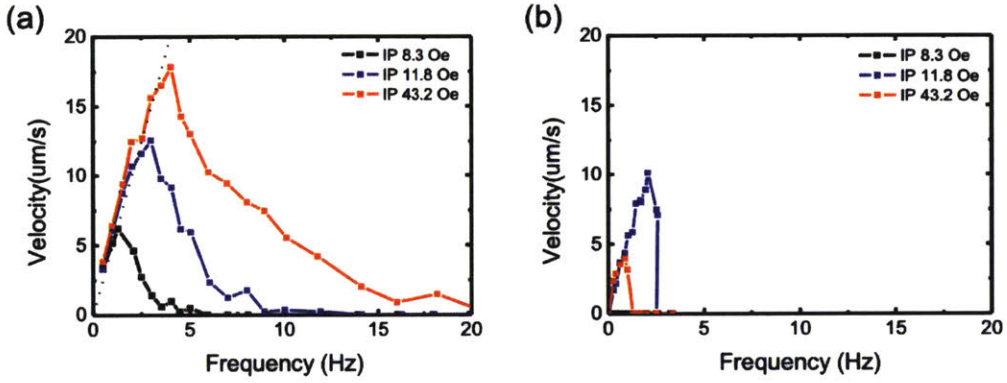

Figure 6-4 Velocity as a function of frequency at SPB diameter of 4.3 μm at H_{OOP} = 13. 5 Oe and H_{IP} = 8.3 Oe, 11.8 Oe, and 43.2 Oe on antidot array with (a) PMA and (b) in-plane magnetic anisotropy.

6.2.2 Distinct dynamics of SPBs along the symmetry of patterns

Next, we analyze the dynamics of SPBs that are different along the symmetry of patterns. Figure 6-5 shows the v of SPBs as a function of frequency f for diameter of 2.8 μm on (a) the square symmetry and (b) the hexagonal symmetry. We varied f from 0 Hz to 25 Hz at H_{OOP} = 40.5 Oe and H_{IP} = 28.8 Oe. In Figure 6-5, the f_c is approximately 4.0 Hz and 4.5 Hz for the square lattice and the hexagonal lattice, respectively. Interestingly, we observe that the maximum v of the square lattice is 1.5 times higher than that of the hexagonal lattice. In addition, the v of the hexagonal

lattice is generally smaller than for the square lattice, even if they have the same diameter and periodicity.

To understand this phenomenon, we calculated the relationship between v and f for each structure based on magnetophoretic transport modeling already discussed in Section 4.1. In Figure 6-5 the dashed curves show the calculated time-averaged velocity. The experimental data with Eq. (37) is fitted well to the dashed curve in both cases. The slope of the linear region are predicted to be 5 and 2.55 for the square lattice and the hexagonal lattice, respectively. For the square lattice, the slope of the linear region in the experimental data is 4.97, a value that is very similar to the slope of 5 predicted by Eq. (37). However, for the hexagonal lattice, the v diverges from the original theoretical slope of 5, and it is more pronounced for the linear region.

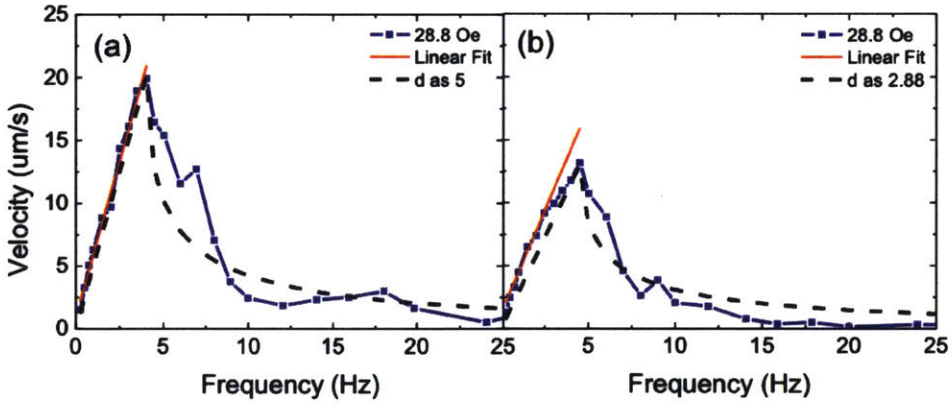

Figure 6-5 Velocity as a function of frequency at SPB diameter of 2.8 μm at H_{OOP} = 40.5 Oe and H_{IP} = 28.8 Oe on square lattice. The dashed or dotted lines are the simulated velocity for the 2.8 μm, based on an appropriate value for the critical frequency.

In order to understand the discrepancy of velocity between the square and hexagonal lattices, we have imaged the motion of SPBs between two points (A to A') by taking snapshots every 0.20 and 0.35 second on the square lattice and the hexagonal lattice, respectively. The f of

the rotating field is 1 Hz, below the f_c of both SPB transports. Figure 6-6 (a)-(e) and (f)-(j) represent 5 steps of the SPB movements when the SPBs are traveling to the nearest micro-magnet along the x direction. The SPBs' transport is observed as a hopping motion on the antidot array and they move slightly along the y-direction during the motion. The remarkable difference between the SPB motions on each lattice is that the movement of the SPBs are a triangular shape on the hexagonal lattice, as represented as A-B-A' in Figure 6-6 (f)-(j). Due to the zig-zag motion, the total traveling time on the hexagonal lattice is 1.4 seconds from A to A', while, for the same distance, it is 0.8 second on the square lattice. The v of the SPBs on the hexagonal lattice decreases by 40%, and the shape of the traveling potential wells on the hexagonal lattice is different from that on the square lattice. Considering the tracking of the SPBs' behavior on the hexagonal lattice, which is jumping from A to B as well as B to A' in Figure 6-6, the distance d can be chosen as around 2.88. The ratio of the experimentally determined v for the two lattices is 1.4/0.8 = 1.75 in Figure 6-6, showing a similar value to the predicted ratio of the time-averaged velocity as 5/2.88 = 1.73 predicted by Eq. (37). We conclude that the simplified calculation of the magnetophoretic transport can be applied for SPB transport on antidot arrays.

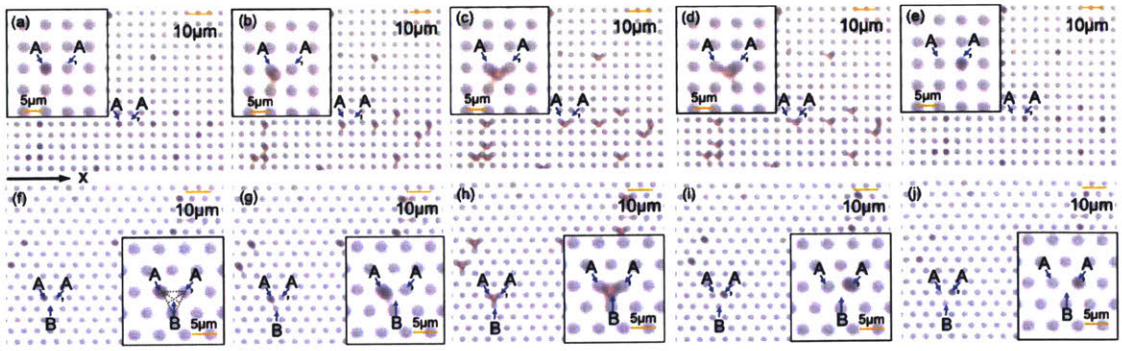

Figure 6-6 Two series of the bead movement snapshots for (a) every 0.20 second with 2.8 μm beads on square lattice and (b) every 0.35 second with 2.8 μm beads on hexagonal lattice.

6.3 Threshold behavior in the magnetic field analyzed through micro-magnetic simulation

In this section, we examine the effect of the applied fields on the SPB movements. The motions of the SPBs are strongly affected and switched on and off by the strength of an applied field. Figure 6-7 show the working ranges for the transport of 2.8 μm SPBs as a function of magnetic field components: H_{IP} and H_{OOP} on the square antidot array and the hexagonal antidot array at 1 Hz, respectively. As previously mentioned, we observe the SPB transport at the blue dots of magnetic field combinations, whereas the SPBs cannot move and simply oscillate back and forth at the red cross field combinations. Compared to the similar samples with in-plane anisotropy, the PMA samples have small threshold values in both H_{IP} and H_{OOP}.

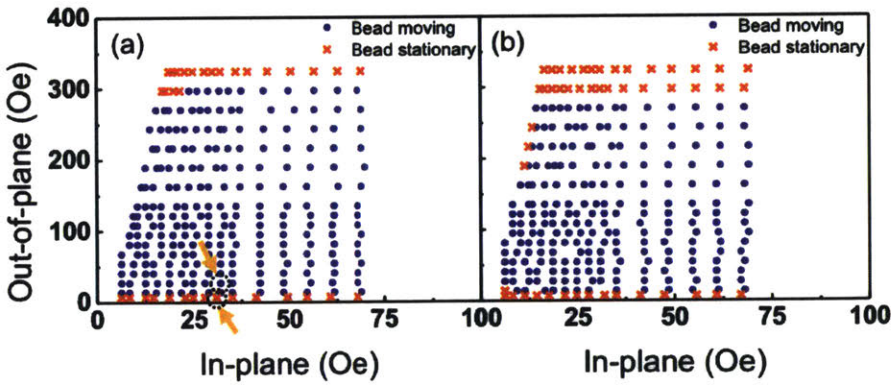

Figure 6-7 Critical threshold of both H_{IP} and H_{OOP} for both (a) square lattice (b) hexagonal lattice. The blue dot and the red cross show the moving bead and stationary bead, respectively.

In addition, the PMA samples generally have SPB movements in a wider range of applied fields. In Figure 6-7, both antidot arrays have a maximum working field of H_{OOP}, corresponding approximately to the coercive fields of the respective systems. The phenomenon can be illustrated by the traveling magnetic field wave. When the magnetic field is larger than the H_c of samples, the minimum position of the potential energy cannot be changed by applying a rotating field. Therefore, the SPB motions on the antidot arrays with PMA, which generally have a high H_c, are observed only in a relatively high magnetic field.

6.4 Numerical studies of threshold behavior in PMA systems

In this section, to find out the origin of the threshold at the lower magnetic field, we performed micro-magnetic simulations to determine magnetostatic potential energy and magnetic interaction force. Figure 6-8 (a) show the energy landscape for 2.8 μm SPBs on the square antidot array without applying a magnetic field. The minimum positions are observed on the rims of the holes on the square antidot array.

The elliptical rotating fields are represented in Figure 6-8 (b), and Figures 6-8 (c) and (d) represent several cross-sections of the magnetic potential energy for 2.8 μm SPBs on the square lattice at two different magnetic field conditions: the red cross and the blue dot in Figure 6-7 (a). The SPBs are attracted to the regions of maximum local magnetic field, where the magnetic potential energy is minimal. The tracking of the minimum regions in Figures 6-8 (c) and (d) describe different behavior for a period of the rotating field. As shown in Figure 6-8 (c), every 35° of the rotating field, the minimum regions are slowly moving to the A', but the position is moving back to A between 75° to 215°. Therefore, the SPBs move back and forth for a 360° rotating of the magnetic field, while the trajectory of the minimum region is different in Figure 6-8 (d), where the regions continuously move to the right. In Figure 6-8 (d), the SPBs can be transported from A to A' by a rotation of the magnetic fields. Thus, these results clearly explain two different behaviors of the SPBs: oscillation below the threshold field and transport above the threshold field. Furthermore, when comparing the depths of the potential wells to each other, the depth in Figure 6-8 (c) is shallower than that of Figure 6-8 (d). The magnetic force at Figure 6-8 (c) is smaller, and

the force is not sufficient to transport the SPBs. Following the discussion above, these results show the origins for the two different behaviors of the SPBs on the square antidot array.

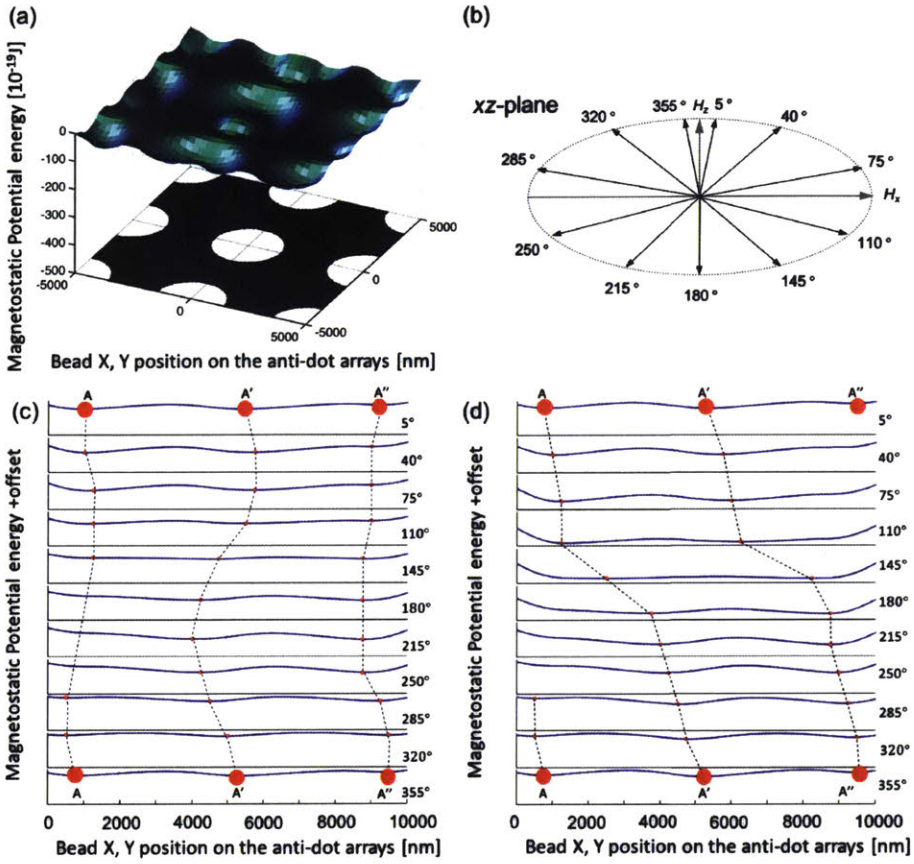

Figure 6-8 (a) The relaxed DW configuration and magnetostatic potential well for square lattice; (b) the rotating field in the xz-plane with each angle θ of a rotational period; (c) and (d) are the cross-section of potential wells for 2.8 μm SPBs and minimum position (red circle) tracking at two different magnetic fields (c) the red cross and (d) blue dot on the square lattice in Figure 6-7 (a).

Finally, we also calculated the magnetic potential energy of the hexagonal lattice for 2.8 μm at two different magnetic field combinations: (a) below and (b) above the threshold field. Figure 6-9 describes the sequential potential energy landscapes at the same angle intervals for a

rotation of the applying field. The yellow color indicates the minimum positions of potential energy landscapes. Comparing the upper row and the lower row, the minimum positions have different behavior when changing the angle of the rotating field. Figure 6-9 (a) describes the oscillation behavior of the SPBs, where the minimum positions slowly move to the right, but move back to the left after 145°. At around 145°, the SPBs can be located only around the rim of the hole, where the depths of minimum positions are the same as each other. On the other hand, Figure 6-9 (b) describes the zig-zag motion (A-B-A') of the SPB transport. When a field is rotating, the tracking of minimum positions can continuously proceed to the right. At around 145°, where the minimum position can be located everywhere except for the inside of the hole, the SPBs can be located, and freely move between the holes, including the B areas. Therefore, the SPBs can be continuously transported to the right, which is different from the above case. These simulation results together with the ones presented in Figure 6-9 (a) describe the origin for the threshold in the magnetic field, and explain the origin of SPB movements in a zig-zag manner.

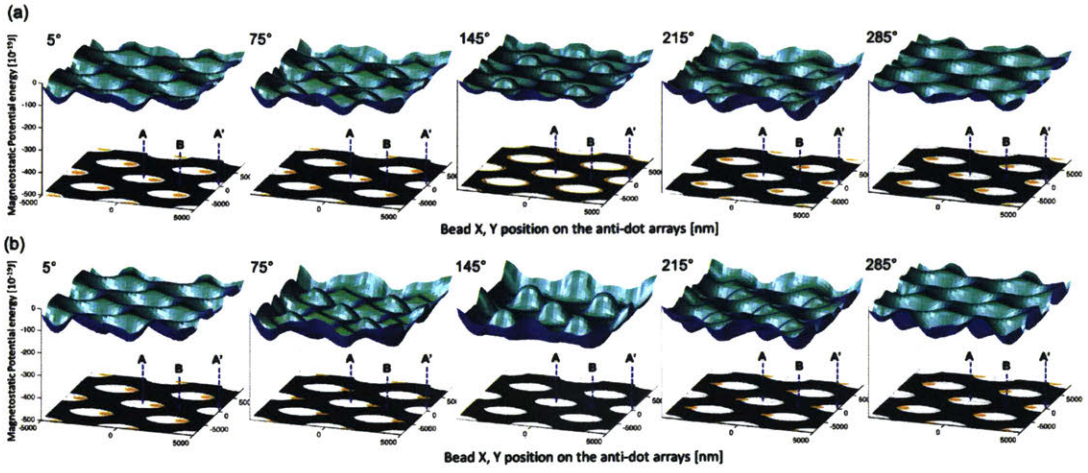

Figure 6-9 The relaxed DW configuration and magnetostatic potential well of the hexagonal lattice for every 70° of a rotational period (a) below the threshold value and (b) above the threshold value. The yellow regions indicate the minimum position of potential landscape.

6.5 Bead separation

Through Section 4.8 and Section 5.3, we demonstrated the SPB sorting that is based on the threshold of a magnetic field. Here, we show another SPB separation mechanism that is based on the fact that f_c varies along with the size of SPBs.

Figure 6-10 represents the sequential snapshots for every 1.5 seconds and shows the SPB sorting through their f_c values at H_{OOP} = 6.5 Oe and H_{IP} = 120 Oe. The suspension is a mixture of 2.8 μm and 5.8 μm SPBs and the yellow circles indicate the 2.8 μm SPBs in Figure 6-10. When the f = 3.5 Hz, a value is greater than the f_c of 5.8 μm SPBs ($f_{c(5.8\mu m)} \sim 2.5$ Hz), but lower than the f_c of 2.8 μm SPBs ($f_{c(2.8\mu m)} \sim 7.5$ Hz), the fast transport of 2.8 μm (indicated as yellow circles) is observed. However, 5.8 μm SPBs are moved back and forth. The combination of the magnetic field is above the threshold of H_{IP} and H_{OOP} for both sizes of SPBs. Thus, the f_c is used to separate one size of SPBs from the mixture of SPBs, and the sorting principle, which has also been demonstrated in literature[36,38], can be applied in a large volume.

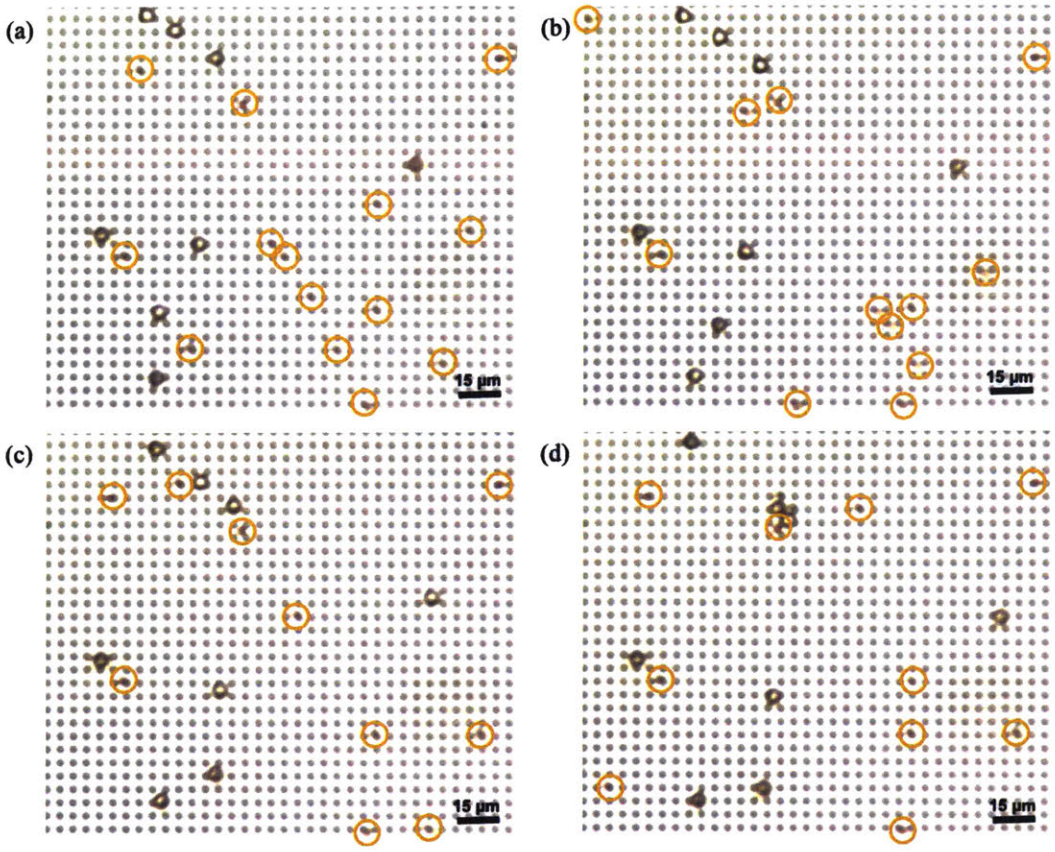

Figure 6-10 Optical microscopy images showing a series SPB movement snapshots for every 1.5 seconds with 2.8 µm SPBs indicated as smaller circles (marked as yellow) and 5.8 µm SPBs as larger ones.

6.6 Summary

Using a well-ordered antidot array with PMA, the dynamics of the SPBs can be controlled by crucial parameters such as threshold frequency *fc* as well as H_{IP} and H_{OOP}. We observed that the dynamics of the SPBs on PMA substrates become more effective than with in-plane anisotropy. In addition, PMA substrates have a larger working range in terms of magnetic fields to transport the SPBs. Finally, we showed the different SPB dynamics with square and hexagonal lattices due to the differences in the magnetic potential wells, as revealed by micro-magnetic simulations and modeling. These findings clearly demonstrate the enhanced dynamics of the SPBs on PMA substrates, and may be useful for designing the transport of magnetic particles for potential applications.

Chapter 7

Summary and future work

7.1 Summary

Through this research, we have presented the control and manipulation of the transport of SPBs on a variety of magnetic antidot arrays, which is useful for lab-on-a-chip applications and could also open up possibilities for new Superparamagnetic bead (SPB) sorting fields. We started with antidot arrays with in-plane anisotropy and developed the controlling factors for the dynamics of SPBs including f_c and threshold values in both H_{IP} and H_{OOP}. We determined that these thresholds in the magnetic field are related to the depth of the magnetostatic potential energy landscape and the magnetic force. In addition, these parameters have dependency on the magnetized direction, the symmetry of pattern, and the d of the SPBs. Thus, they can be used in sorting a mixture of SPBs that is composed of 2.8 μm and 4.2 μm SPBs.

In addition, when we considered the ratio between the d of the SPBs and the p of patterns, the f_c behavior and threshold values in the magnetic fields are also observed in antidot arrays, which are produced through microsphere lithography and where the p of the pattern is much smaller than the d of the SPBs. We were able to demonstrate the sorting of SPBs based on the H_{OOP} on an antidot array with 1 μm periodicity.

As we continued to explore the SPB dynamics, we found it could also be controlled by parameters such as f_c as well as H_{IP} and H_{OOP} on an antidot array with PMA, where the large stray

field can be easily obtained due to out-of-plane magnetization in equilibrium. We described how the dynamics of SPBs on PMA systems become more effective than on in-plane anisotropy, and it was observed in the widened scope of the rotating field. Finally, we showed that the symmetry of the antidot array largely definitely affected the SPB dynamics, and we described how the differences resulted from the magnetic potential well based on micro-magnetic simulation and modeling.

By harnessing the strong gradient field of the edge of holes, using various antidot structures, and carefully investigating SPB dynamics, we have successfully developed a well-ordered antidot structure integrating SPB transport and sorting. These findings show the feasibility of the enhanced dynamics of SPBs and provide flexibility for designing the transport of magnetic particles for on-chip applications.

7.2 Future work

The work of this thesis has demonstrated that the long-distance actuation of SPBs can be achieved on magnetic antidot arrays and that controlling parameters can be used in SPB sorting. In addition, the interaction between micro-magnetic arrays and SPBs creates an opportunity for a range of future applications. In this final section, we discuss ideas for future work that can follow as extensions of the work already done throughout this thesis.

7.2.1 Integration with biological entities

The major motivation of this thesis is related to the possibilities of lab-on-a-chip applications, which can able to be used in medical diagnostics and target delivery. We have presented the controlling parameters relying on the SPBs and periodic magnetic texture, and which can thus be applied in SPB sorting system. However, our demonstration of SPB operation has been limited and can be expanded as describe below.

In future work, we would like to integrate the SPBs with biological entities and describe the behaviors of controlling parameters such as f_c and threshold values in H_{IP} and H_{OOP}. For example, the biological substances are bound to the SPBs through appropriate affinity receptors, and these magnetophoretic behaviors of the SPB-microorganism complexes would be characterized by measuring the average velocity of the whole group of SPBs along with the driving f from 0 Hz to 20 Hz. In addition, the magnetic field ranges where the complexes can be transported are also different due to changes such as the effective hydrodynamic drag. Thus, threshold

behaviors of the SPB-microorganism complexes can be also be characterized by varying the magnetic field combinations at1Hz, and the results can be analyzed as a function of applying the magnetic field components H_{IP} and H_{OOP} on antidot arrays.

After these experiments, the mixture of the complexed SPBs and uncomplexed SPBs can be placed in an inlet well in a PDMS layout. We expect that the complexed SPBs have a lower f_c due to the larger hydrodynamic drag, and a wider range of magnetic field combinations for traveling because of larger magnetic forces on the SPBs. Thus, there will be two methods to separate the complexed SPBs from the mixture, which are based on the f_c and threshold values in the magnetic fields, respectively. As previously shown in Sections 4.8, 5.3, and 6.5, only one type of SPB can be transported when we apply values that are between the f_c or thresholds of each SPB.

7.2.2 Chain formation of SPBs

In recent years, the chain movement of SPBs has been widely studied for the potential application of lab-on-a-chip.[140] The rotations of SPB chain structures are described by the Manson number, which represents the ratio between the magnetic attraction and hydrodynamic drag. Thus, when the parameter exceeds certain values, the chains of SPBs will be ruptured into small fractures[164-165]. In addition, the shape and length of chains can be modified by the strength of a magnetic field component and the rotation of a chain results in the transport of SPBs in a high volume when a rotating magnetic field is applied[166-167].

When we applied a rotating magnetic field in the *xz*-plane, we frequently observed the formation of chains and movement in the chain shape at a very high ratio between H_{IP} and H_{OOP} components, as shown in Figure 7-1. In addition, these chain structures can be moved or

transported at a high driving f that is above the f_c, and we also observed that chain-structured SPBs can travel together even when the single SPB is just oscillating back and forth. Therefore, it is clear evidence that the chain structure would have a higher f_c and wider range of magnetic field combinations even at extreme values, and these structures would be more easily transported than single SPB.

Furthermore, the movement of SPB chains is different from the 'walking'[166] or 'oscillation'[165] of SPBs that has been reported in previous studies. We assume that this difference results from the roughness of the surface and patterning of the structure. In near future, we hope that the relation between the motion of superparamagnetic chains and the strength of magnetic fields will be demonstrated, thereby determining the critical thresholds of SPB chain structures.

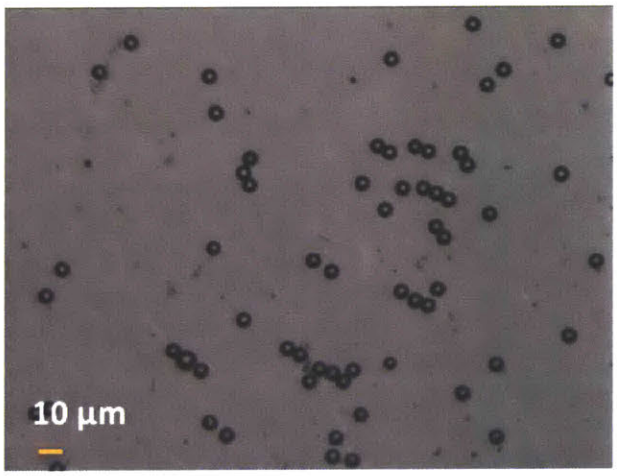

Figure 7-1 The snapshot of the 5.8 µm diameter SPBs movement at H_{IP} = 9.5 Oe and H_{OOP} = 51.5 Oe at 1 Hz.

Appendix

In this chapter, we discuss the several reference experiments to confirm that the movement of superparamagnetic beads (SPBs) was caused by the mechanism which is based on the magnetophoretic transport model. The reference experiments are categorized into two parts: the bead movement on the continuous film and the bead movement on the antidot structures which are composed of Cr instead of Co.

At first, a reference structure was coated with a 40 nm thick Co layer without patterning process, and then 70 nm thick protective SiO_2 layer was deposited by RF magnetron sputtering. Before starting experiments, we measure the hysteresis loops of each structure with a Vibrating sample magnetometer (VSM) under H_{IP} and the results shows square loops with respect to the H_{IP}, confirming that they exhibit in-plane anisotropy. We Other processes for the bead motion experiments are the same parameters and condition including the size of beads, position of samples, and density of bead solution. Appendix Figure 1 shows sequential snapshots taken every 2 seconds on the continuous film without antidot array shown in the case of a rotating field applied in the *xz* plane for 2.8 μm and 4.3 μm, respectively. In both cases, SPBs 2.8 μm and 4.3 μm slightly oscillated back and forth and they could not travel on the film at all.

In addition, to demonstrate the transport of SPBs are resulted from the Co, antidot arrays with square and hexagonal symmetry were patterned onto Si (100) wafers using a standard lift-off technique. A 40 nm thick Cr layer was deposited by DC magnetron sputtering at room temperature at an Ar pressure of 3.0 mTorr. Following liftoff, the wafer was coated with an 80 nm thick protective SiO_2 layer. Appendix Figure 2 represents the ordered pattern of Cr layer with square symmetry and optical microscopy images during a series of 2.8 μm and 4.3 μm SPB movement

snapshots. Even though the magnetic field is applied that is higher than the threshold of both H_{IP} and H_{OOP} which is based on the previous experiments, we could not observe SPB motions and the beads are locally oscillate back and forth. The similar phenomenon is shown on the antidot array with hexagonal symmetry (Appendix Figure 3).

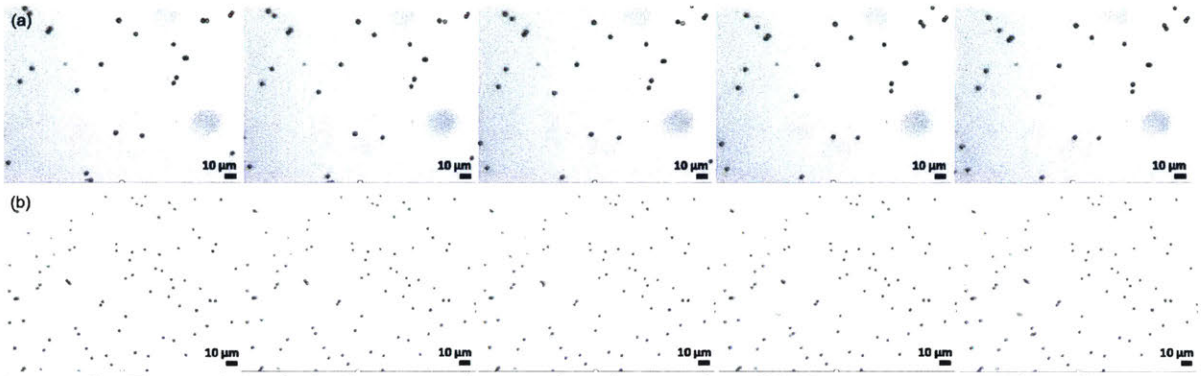

Appendix Figure 1 Optical microscopy images showing a series of SPB movement snapshot taken every 2 seconds with (a) 4.3 μm beads and (b) 2.8 μm beads when the field (H_{IP} = 30 Oe and H_{OOP} = 13. 5 Oe) is rotating clockwise at 1 Hz.

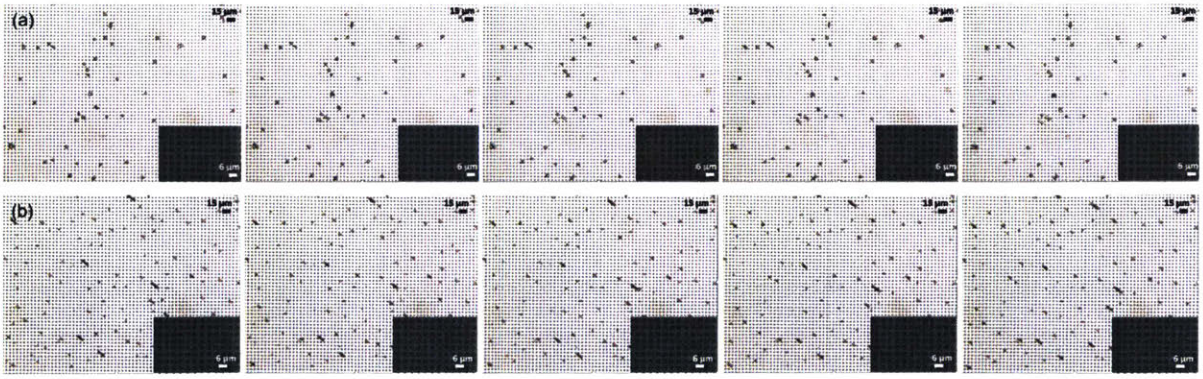

Appendix Figure 2 Optical microscopy images showing a series of SPB movement snapshot taken every 2 seconds with (a) 4.3 μm beads and (b) 2.8 μm beads on antidot arrays with square symmetry when the field (H_{IP} = 67.5 Oe and H_{OOP} = 51. 5 Oe) is rotating clockwise at 0.5 Hz.

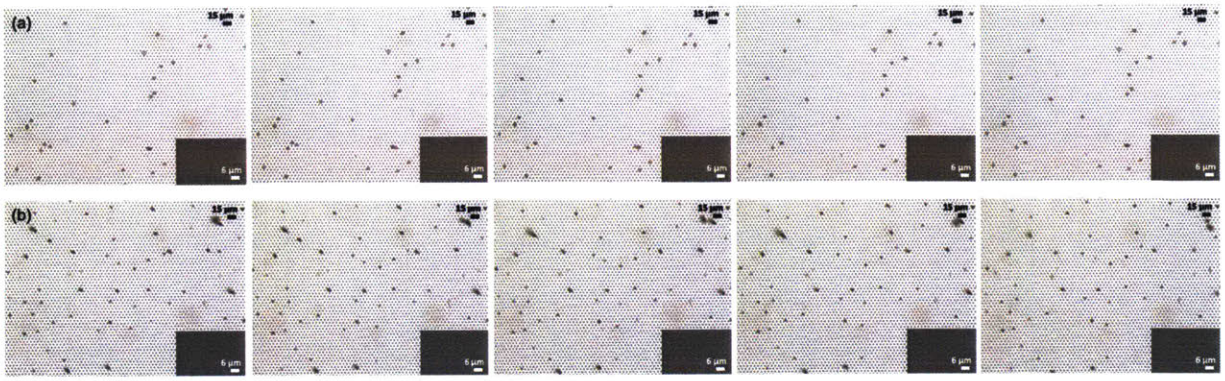

Appendix Figure 3 Optical microscopy images showing a series of SPB movement snapshot taken every 2 seconds with (a) 4.3 μm beads and (b) 2.8 μm beads on antidot arrays with hexagonal symmetry when the field (H_{IP} = 67.5 Oe and H_{OOP} = 51. 5 Oe) is rotating clockwise at 0.5 Hz.

We also discussed the SPB motion on the Co/Pt multilayers and confirmed the movement of SPBs can be explained by the magnetophoretic transport modeling through several reference experiments. At first, the continuous films of Ta(3 nm)/Pt(5 nm)/[Co(1 nm)/Pt(4.5 nm)]$_5$ multilayers were used to bead motion experiments. The hysteresis loops of the multilayers represent the high squareness under the H_{OOP}, confirming that they exhibit the out-of-plane anisotropy. Appendix Figure 4 represent the bead motion on these substrates, where we examine the rotating-field-driven motion of 2.8 μm and 5.8 μm beads. The applying field is higher than the threshold of both H_{IP} and H_{OOP}, and the driving frequency is lower than the critical frequency f_c for both size of beads. As we anticipated, the 2.8 μm (Appendix Figure 4 (b)) and 5.8 μm SPBs (Appendix Figure 4 (a)) cannot move and simply oscillate back and forth on the continuous films even though the structure represent the out-of-plane anisotropy and high stray field. Thus, the bead motion was related to the stray field coming from the edge of antidot structures.

Furthermore, to demonstrate that bead motion was resulted from the periodic potential landscape, several antidot array with hexagonal symmetry and square symmetry were used for the bead motion experiments. Appendix Figure 5 and Appendix Figure 6 represent the sequential snapshots taken every 2 seconds on these antidot arrays shown in the case of a rotating field applied in the *xz* plane. Here, the 2.8 μm or 4.3 μm SPBs were placed on the substrate, and the field amplitudes were chosen to be higher than the transport threshold for these two bead sizes. The frequency of the driving field is about 0.5 Hz, and it is below the f_c of both sizes of SPBs. As

shown in the figures, both SPBs 2.8 μm and 4.3 μm simply represent the back-and-forth oscillation rather than translating across the antidot arrays. This demonstrates that the SPBs can be transported the periodic potential landscape due to the magnetostatic interaction between the beads and the field gradients, which generated by the underlying antidot structures.

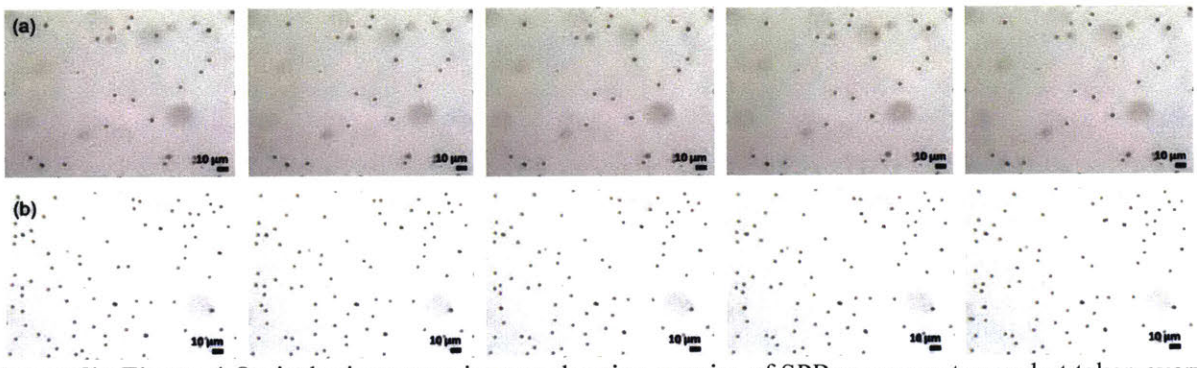

Appendix Figure 4 Optical microscopy images showing a series of SPB movement snapshot taken every 2 seconds with (a) 4.3 μm beads and (b) 2.8 μm beads when the field (H_{IP} = 30 Oe and H_{OOP} = 40. 5 Oe) is rotating clockwise at 0.5 Hz.

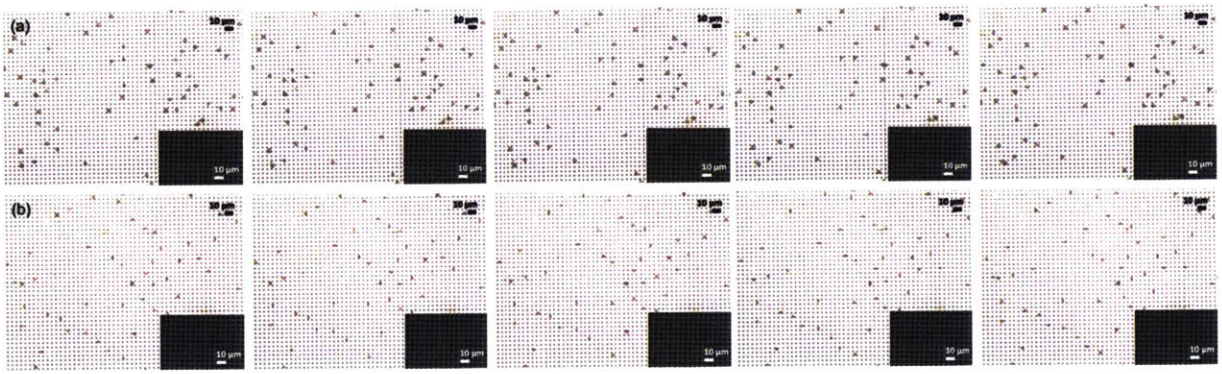

Appendix Figure 5 Optical microscopy images showing a series of SPB movement snapshot taken every 2 seconds with (a) 4.3 μm beads and (b) 2.8 μm beads on antidot arrays, where the antidot array exhibit square symmetry and out-of-plane anisotropy when the field (H_{IP} = 67.5 Oe and H_{OOP} = 51. 5 Oe) is rotating clockwise at 0.5 Hz

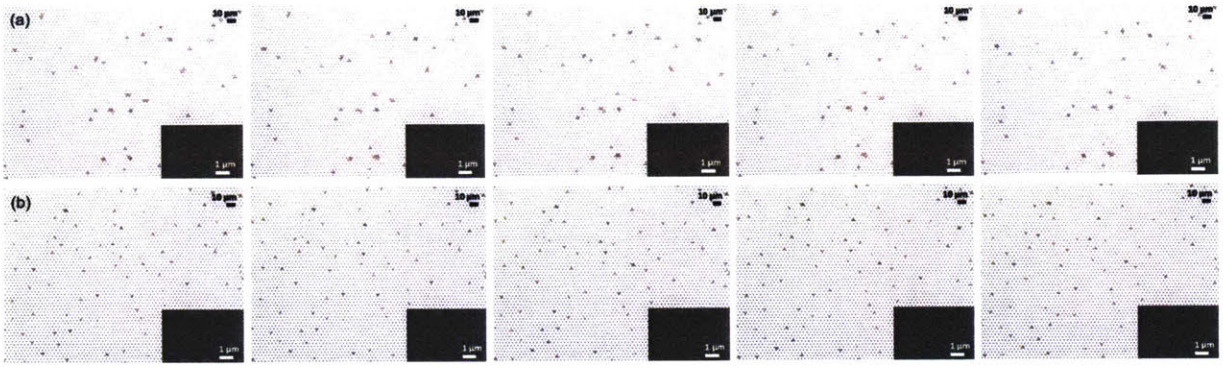

Appendix Figure 6 Optical microscopy images showing a series of SPB movement snapshot taken every 2 seconds with (a) 4.3 μm beads and (b) 2.8 μm beads on antidot arrays, where the antidot array exhibit hexagonal symmetry and out-of-plane anisotropy when the field (H_{IP} = 95 Oe and H_{OOP} = 25 Oe) is rotating clockwise at 0.5 Hz

Bibliography

1 Hertz, H. M. Standing-wave acoustic trap for nonintrusive positioning of microparticles. *Journal of Applied Physics*, *78*(8), 4845–4849 (1995).

2 Zhang, H., Xu, T., Li, C. W., & Yang, M. A microfluidic device with microbead array for sensitive virus detection and genotyping using quantum dots as fluorescence labels. *Biosensors and Bioelectronics*, *25*(11), 2402–2407 (2010).

3 Tennico, Y. H., Hutanu, D., Koesdjojo, M. T., Bartel, C. M., & Remcho, V. T. On-chip aptamer-based sandwich assay for thrombin detection employing magnetic beads and quantum dots. *Analytical Chemistry*, *82*(13), 5591–5597 (2010).

4 Jans, H., Jans, K., Demeyer, P. J., Knez, K., Stakenborg, T., Maes, G., & Lagae, L. A simple double-bead sandwich assay for protein detection in serum using UV-vis spectroscopy. *Talanta*, *83*(5), 1580–1585 (2011).

5 Friend, J., & Yeo, L. Y. Microscale acoustofluidics: Microfluidics driven via acoustics and ultrasonics. *Reviews of Modern Physics*, *83*(2), 647–704 (2011).

6 Wiklund, M., Green, R., & Ohlin, M. Acoustofluidics 14: Applications of acoustic streaming in microfluidic devices. *Lab on a Chip*, *12*(14), 2438–51 (2012).

7 Wiklund, M., & Hertz, H. M. Ultrasonic enhancement of bead-based bioaffinity assays. *Lab on a Chip*, *6*(10), 1279–1292 (2006).

8 Ding, X., Lin, S.-C. S., Kiraly, B., Yue, H., Li, S., Chiang, I.-K., … Huang, T. J. On-chip manipulation of single microparticles, cells, and organisms using surface acoustic waves. *Proceedings of the National Academy of Sciences*, *109*(28), 11105–11109 (2012).

9 Pei Yu, C., Ohta, A. T., & Wu, M. C. Massively parallel manipulation of single cells and microparticles using optical images. *Nature*, *436*(7049), 370–372 (2005).

10 Psaltis, D., Quake, S. R., & Yang, C. Developing optofluidic technology through the fusion of microfluidics and optics. *Nature*, *442*(7101), 381–6 (2006).

11 Yang, A. H. J., Moore, S. D., Schmidt, B. S., Klug, M., Lipson, M., & Erickson, D. Optical manipulation of nanoparticles and biomolecules in sub-wavelength slot waveguides. *Nature*, *457*(7225), 71–75 (2009).

12 Dholakia, K., & Reece, P. Optical micromanipulation takes hold. *Nano Today*, *1*(1), 18–27 (2006).

13 Fan, X., & White, I. M. Optofluidic Microsystems for Chemical and Biological Analysis. *Nature Photonics*, *5*(10), 591–597 (2011).

14 Jonáš, A., & Zemánek, P. Light at work: The use of optical forces for particle manipulation, sorting, and analysis. *Electrophoresis*, *29*(24), 4813–4851 (2008).

15 Xin, H., Bao, D., Zhong, F., & Li, B. Photophoretic separation of particles using two tapered optical fibers. *Laser Physics Letters*, *10*(3), 36004 (2013).

16 Yalikun, Y., Akiyama, Y., & Morishima, K. Multiple microfluidic stream based manipulation for single cell handling. *IEEE International Conference on Intelligent Robots and Systems*, (D), 508–513 (2013).

17 Tanyeri, M., Johnson-Chavarria, E. M., & Schroeder, C. M. Hydrodynamic trap for single particles and cells. *Applied Physics Letters*, *96*(22), 1–4 (2010).

18 Chung, J., Kim, Y. J., & Yoon, E. Highly-efficient single-cell capture in microfluidic array chips using differential hydrodynamic guiding structures. *Applied Physics Letters*, *98*(12) (2011).

19 Yalikun, Y., Akiyama, Y., Asano, T., & Morishima, K. System integration, modelling, and simulation for automation of multiple microfluidic stream based bio-manipulation. *Proceedings - International Conference on Intelligent Systems, Modelling and Simulation, ISMS*, *2015–September*, 209–214 (2015).

20 Chung, A. J., Gossett, D. R., & Di Carlo, D. Three dimensional, sheathless, and high-throughput microparticle inertial focusing through geometry-induced secondary flows. *Small*, *9*(5), 685–690 (2013).

21 Huang, L. R., Cox, E. C., Austin, R. H., & Sturm, J. C. Lateral Displacement, *304*(December 2003), 987–991 (2004).

22 Vigolo, D., Rusconi, R., Stone, H. a., & Piazza, R. Thermophoresis: microfluidics characterization and separation. *Soft Matter*, *6*(15), 3489 (2010).

23 Effenhauser, C. S., Bruin, G. J. M., & Paulus, A. Integrated chip-based capillary electrophoresis. *Electrophoresis*, *18*(12–13), 2203–2213 (1997).

24 Dorfman, K. D. DNA electrophoresis in microfabricated devices. *Reviews of Modern Physics*, *82*(4), 2903–2947 (2010).

25 Bruin, G. J. M. Recent developments in electrokinetically driven analysis on microfabricated devices. *Electrophoresis*, *21*(18), 3931–3951 (2000).

26 Becker, M., Marggraf, U., & Janasek, D. Separation of proteins using a novel two-depth miniaturized free-flow electrophoresis device with multiple outlet fractionation channels. *Journal of Chromatography A*, *1216*(47), 8265–8269 (2009).

27 Hughes, M. P. Strategies for dielectrophoretic separation in laboratory-on-a-chip systems. *Electrophoresis*, *23*(16), 2569–2582 (2002).

28 Iliescu, C., Yu, L., Tay, F. E. H., & Pang, A. J. Bidirectional field-flow particle separation method in a dielectrophoretic chip with 3D electrodes. *TRANSDUCERS and EUROSENSORS '07 - 4th International Conference on Solid-State Sensors, Actuators and Microsystems*, *129*, 1837–1840 (2007).

29 Gascoyne, P. R. C., & Jody Vykoukal. Review Particle separation by dielectrophoresis. *Electrophoresis*, *23*, 1973–1983 (2002).

30 Lapizco-Encinas, B. H., Simmons, B. A., Cummings, E. B., & Fintschenko, Y. Insulator-based dielectrophoresis for the selective concentration and separation of live bacteria in water. *Electrophoresis*, *25*, 1695–1704 (2004).

31 Lapizco-Encinas, B. H., Davalos, R. V., Simmons, B. A., Cummings, E. B., & Fintschenko, Y. An insulator-based (electrodeless) dielectrophoretic concentrator for microbes in water. *Journal of Microbiological Methods*, *62*(3 SPEC. ISS.), 317–326 (2005).

32 Dalslet, B. T., Damsgaard, C. D., Donolato, M., Strømme, M., Strömberg, M., Svedlindh, P., Hansen, MF., M. Bead magnetorelaxometry with an on-chip magnetoresistive sensor. *Lab Chip*, *11*(2), 296–302 (2011).

33 Rapoport, E., & Beach, G. S. D. (2012). Magneto-mechanical resonance of a single superparamagnetic microbead trapped by a magnetic domain wall. *Journal of Applied Physics*, *111*(7), 21–23. https://doi.org/10.1063/1.3672406

34 Rapoport, E., Montana, D., & Beach, G. S. D. Integrated capture, transport, and magneto-mechanical resonant sensing of superparamagnetic microbeads using magnetic domain walls. *Lab on a Chip*, *12*(21), 4433–40 (2012).

35 Yellen, B. B., & Virgin, L. N. Nonlinear dynamics of superparamagnetic beads in a traveling magnetic-field wave. *Physical Review E - Statistical, Nonlinear, and Soft Matter Physics*, *80*(1), 1–6 (2009).

36 Yellen, B. B., Erb, R. M., Son, H. S., Hewlin, Jr., R., Shang, H., & Lee, G. U. Traveling wave magnetophoresis for high resolution chip based separations. *Lab Chip*, *7*(12), 1681–1688 (2007).

37 Gao, L., Gottron, N. J., Virgin, L. N., & Yellen, B. B. The synchronization of superparamagnetic beads driven by a micro-magnetic ratchet. *Lab on a Chip*, *10*(16), 2108–14 (2010).

38 Tahir, M. A., Gao, L., Virgin, L. N., & Yellen, B. B. Transport of superparamagnetic beads through a two-dimensional potential energy landscape. *Physical Review E - Statistical, Nonlinear, and Soft Matter Physics*, *84*(1), 1–8 (2011).

39 Yellen, B. B., Halverson, D. S., & Friedman, G. Arranging matter by magnetic nanoparticle assembly. *INTERMAG 2006 - IEEE International Magnetics Conference*, (Track II), 246 (2006).

40 Castro, C. M., Ghazani, A. A., Chung, J., Shao, H., Issadore, D., Yoon, T.-J., ... Lee, H. Miniaturized nuclear magnetic resonance platform for detection and profiling of circulating tumor cells. *Lab on a Chip*, *14*(1), 14–23 (2013).

41 Kirby, D., Siegrist, J., Kijanka, G., Zavattoni, L., Sheils, O., O'Leary, J., Burger, R., Ducree, J. Centrifugo-magnetophoretic particle separation. *Microfluidics and Nanofluidics*, *13*(6), 899–908 (2012).

42 Issadore, D., Shao, H., Chung, J., Newton, A., Pittet, M., Weissleder, R., & Lee, H. Self-assembled magnetic filter for highly efficient immunomagnetic separation. *Lab on a Chip*, *11*(1), 147–151 (2011).

43 Adams, J. D., Kim, U., & Soh, H. T. Multitarget magnetic activated cell sorter. *Proceedings of the National Academy of Sciences*, *105*(47), 18165–18170 (2008).

44 Nam, J.-M., Thaxton, C. S., & Mirkin, C. A. Nanoparticle-based bio-bar codes for the ultrasensitive detection of proteins. *Science (New York, N.Y.)*, *301*(5641), 1884–6 (2003).

45 Pamme, N., & Wilhelm, C. Continuous sorting of magnetic cells via on-chip free-flow magnetophoresis. *Lab on a Chip*, *6*(8), 974–980 (2006).

46 Thiel, A., Scheffold, A., & Radbruch, A. Immunomagnetic cell sorting-pushing the limits. *Immunotechnology*, *4*(2), 89–96 (1998).

47 Gijs, M. A. M. Magnetic bead handling on-chip: New opportunities for analytical applications. *Microfluidics and Nanofluidics*, *1*(1), 22–40 (2004).

48 Šafařík, I., & Šafaříková, M. Use of magnetic techniques for the isolation of cells. *Journal of Chromatography B: Biomedical Sciences and Applications*, *722*(1–2), 33–53 (1999).

49 Johansson, L., Gunnarsson, K., Bijelovic, S., Eriksson, K., Surpi, A., Göthelid, E., Svedlindh, P., Oscarsson, S. A magnetic microchip for controlled transport of attomole levels of proteins. *Lab on a Chip*, *10*(5), 654–661 (2010).

50 Michael Arnold, W. Positioning and levitation media for the separation of biological cells. *IEEE Transactions on Industry Applications*, *37*(5), 1468–1475 (2001).

51 Pankhurst, Q. a, Connolly, J., Jones, S. K., & Dobson, J. Applications of magnetic nanoparticles in biomedicine. *Journal of Physics D: Applied Physics*, *36*(13), R167–R181 (2003).

52 Krebs, M. D., Erb, R. M., Yellen, B. B., Samanta, B., Bajaj, A., Rotello, V. M., & Alsberg, E. Formation of Ordered cellular structures in suspension via label-free negative magnetophoresis. *Nano Letters*, *9*(5), 1812–1817 (2009).

53 Voldman, J. Electrical Forces for Microscale Cell Manipulation. *Annual Review of Biomedical Engineering*, *8*(1), 425–454 (2006).

54 Karle, M., Miwa, J., Czilwik, G., Auwärter, V., Roth G., Zengerle R., von Stetten F. Continuous microfluidic DNA extraction using phase-transfer magnetophoresis. *Lab on a Chip*, *10*(23), 3284–90 (2010).

55 Pamme, N., & Manz, A. On-chip free-flow magnetophoresis: Continuous flow separation of magnetic particles and agglomerates. *Analytical Chemistry*, *76*(24), 7250–7256 (2004).

56 Forbes, T. P., & Forry, S. P. Microfluidic magnetophoretic separations of immunomagnetically labeled rare mammalian cells. *Lab on a Chip*, *12*(8), 1471–9 (2012).

57 Rida, A., & Gijs, M. A. M. Dynamics of magnetically retained supraparticle structures in a liquid flow. *Applied Physics Letters*, *85*(21), 4986–4988 (2004).

58 Ranzoni, A., Schleipen, J. J. H. B., Van Ijzendoorn, L. J., & Prins, M. W. J. Frequency-selective rotation of two-particle nanoactuators for rapid and sensitive detection of biomolecules. *Nano Letters*, *11*(5), 2017–2022 (2011).

59 McNaughton, B. H., Agayan, R. R., Wang, J. X., & Kopelman, R. Physiochemical microparticle sensors based on nonlinear magnetic oscillations. *Sensors and Actuators, B: Chemical*, *121*(1), 330–340 (2007).

60 Lee, C. S., Lee, H., & Westervelt, R. M. Microelectromagnets for the control of magnetic nanoparticles. *Applied Physics Letters*, *79*(20), 3308–3310 (2001).

61 Smistrup, K., Hansen, O., Bruus, H., & Hansen, M. F. Magnetic separation in microfluidic systems using microfabricated electromagnets - Experiments and simulations. *Journal of Magnetism and Magnetic Materials*, *293*(1), 597–604 (2005).

62 Zheng, Y., Mannai, A., & Sawan, M. A BioMEMS chip with integrated micro electromagnet array towards bio-particles manipulation. *Microelectronic Engineering*, *128*, 1–6 (2014).

63 Ramadan, Q., Yu, C., Samper, V., & Poenar, D. P. Microcoils for transport of magnetic beads. *Applied Physics Letters*, *88*(3), 1–3 (2006).

64 Ramadan, Q., & Ting, L. T. Reconfigurable translocation of microbeads using micro-engineered locally controlled magnetic fields. *Journal of Microelectromechanical Systems*, *20*(6), 1310–1323 (2011).

65 Rida, A., Fernandez, V., & Gijs, M. A. M. Long-range transport of magnetic microbeads using simple planar coils placed in a uniform magnetostatic field. *Applied Physics Letters*, *83*(12), 2396–2398 (2003).

66 Gunnarsson, K., Roy, P. E., Felton, S., Pihl, J., Svedlindh, P., Berner, S., Lidbaum, H., Oscarsson, S. Programmable motion and separation of single magnetic particles on patterned magnetic surfaces. *Advanced Materials*, *17*(14), 1730–1734 (2005).

67 Warnicke, P., Felton, S., Gunnarsson, K., & Svedlindh, P. Simulations of magnetic microstructure in thin film elements used for programmable motion of magnetic particles. *Journal of Magnetism and Magnetic Materials*, *303*(2 SPEC. ISS.), 294–298 (2006).

68 Lim, B., Jeong, I., Anandakumar, S., Kim, K. W., & Kim, C. G. Programmable magnetic actuation of biomolecule carriers using NiFe stepping stones. *Journal of Magnetics*, *16*(4), 363–367 (2011).

69 Anandakumar, S., Rani, V. S., Oh, S., Sinha, B. L., Takahashi, M., & Kim, C. Translocation of bio-functionalized magnetic beads using smart magnetophoresis. *Biosensors and Bioelectronics*, *26*(4), 1755–1758 (2010).

70 Venu, R., Lim, B., Hu, X. H., Jeong, I., Ramulu, T. S., & Kim, C. G. On-chip manipulation and trapping of microorganisms using a patterned magnetic pathway. *Microfluidics and Nanofluidics*, *14*(1–2), 277–285 (2013).

71 Lim, B., Reddy, V., Hu, X., Kim, K., Jadhav, M., Abedini-Nassab, R., ... Kim, C. Magnetophoretic circuits for digital control of single particles and cells. *Nature Communications*, *5*(May), 3846 (2014).

72 Abedini-Nassab, R., Murdoch, D. M., Kim, C., & Yellen, B. B. Optimization of magnetic switches for single particle and cell transport. *Journal of Applied Physics*, *115*(24) (2014).

73 Henighan, T., Chen, A., Vieira, G., Hauser, A. J., Yang, F. Y., Chalmers, J. J., & Sooryakumar, R. Manipulation of magnetically labeled and unlabeled cells with mobile magnetic traps. *Biophysical Journal*, *98*(3), 412–417 (2010).

74 Chen, A., & Sooryakumar, R. Patterned time-orbiting potentials for the confinement and assembly of magnetic dipoles. *Scientific Reports*, *3*, 3124–3125 (2013).

75 Katsikis, G., Cybulski, J. S., & Prakash, M. Synchronous universal droplet logic and control. *Nature Physics*, *11*(7), 588–596 (2015).

76 Tierno, P., Reimann, P., Johansen, T. H., & Sagues, F. Giant transversal particle diffusion in a longitudinal magnetic ratchet. *Physical Review Letters*, *105*(23), 1–4 (2010).

77 Tierno, P., Golestanian, R., Pagonabarraga, I., & Sagues, F. Controlled swimming in confined fluids of magnetically actuated colloidal rotors. *Physical Review Letters*, *101*(21), 1–4 (2008).

78 Tierno, P., Johansen, T. H., & Fischer, T. M. Fast and rewritable colloidal assembly via field synchronized particle swapping. *Applied Physics Letters*, *104*(17) (2014).

79 Tierno, P. Depinning and collective dynamics of magnetically driven colloidal monolayers. *Physical Review Letters*, *109*(19), 4–8 (2012).

80 Tierno, P., Reddy, S. V., Jing, Y., Johansen, T. H., & Fischer, T. M. Transport of loaded and unloaded microcarriers in a colloidal magnetic shift register. *Journal of Physical Chemistry B*, *111*(48), 13479–13482 (2007).

81 Tierno, P., Sagues, F., Johansen, T. H., Fischer, T. M., Sagués, F., Johansen, T. H., ... Fischer, T. M. Colloidal transport on magnetic garnet films. *Phys. Chem. Chem. Phys.*, *11*(42), 9615–9625 (2009).

82 Chen, A., Vieira, G., Henighan, T., Howdyshell, M., North, J. A., Hauser, A. J., Yang, F.Y., Poirier, M.G., Jayaprakash, C., Sooryakumar, R. Regulating Brownian fluctuations with tunable microscopic magnetic traps. *Physical Review Letters*, *107*(8), 1–4 (2011).

83 Bryan, M. T., Smith, K. H., Real, M. E., Bashir, M. A., Fry, P. W., Fischer, P., Im, Mi-young, Schrefl, T., Allwood, D.A., Haycock, J. W. Switchable cell trapping using superparamagnetic beads. *IEEE Magnetics Letters*, *1*, 3–6 (2010).

84 Donolato, M., Vavassori, P., Gobbi, M., Deryabina, M., Hansen, M. F., Metlushko, V., Ilic, B., Cantoni, M., Petti, D., Brivio, S., Bertacco, R. On-chip manipulation of protein-coated magnetic beads via domain-wall conduits. *Advanced Materials*, *22*(24), 2706–2710 (2010).

85 Donolato, M., Torti, A., Kostesha, N., Deryabina, M., Sogne, E., Vavassori, P., Hansen, M.F., Bertacco, R. Magnetic domain wall conduits for single cell applications. *Lab on a Chip*, *11*(17), 2976–2983 (2011).

86 Donolato, M., Lofink, F., Hankemeier, S., Porro, J. M., Oepen, H. P., & Vavassori, P. Characterization of domain wall-based traps for magnetic beads separation. *Journal of Applied Physics*, *111*(7) (2012).

87 Donolato, M., Dalslet, B. T., & Hansen, M. F. Microstripes for transport and separation of magnetic particles. *Biomicrofluidics*, *6*(2) (2012).

88 Sohn, H., Nowakowski, M. E., Liang, C., Hockel, J. L., Wetzlar, K., Keller, S., Mclellan, BM., Marcus, MA., Doran A., Young, A., Klaui, M., Carman, GP., Bokor, J., Candler, R. N. Wall Rotation in Multiferroic Heterostructures to Manipulate Suspended On-Chip Magnetic Particles. *ACS Nano*, *9*(5), 4814–4826 (2015).

89 Rapoport, E., & Beach, G. S. D. Dynamics of superparamagnetic microbead transport along magnetic nanotracks by magnetic domain walls. *Applied Physics Letters*, *100*(8) (2012a).

90 Sarella, A., Torti, A., Donolato, M., Pancaldi, M., & Vavassori, P. Two-dimensional programmable manipulation of magnetic nanoparticles on-chip. *Advanced Materials*, *26*(15), 2384–2390 (2014).

91 Yellen, B. B., & Virgin, L. N. Nonlinear dynamics of superparamagnetic beads in a traveling magnetic-field wave. *Physical Review E - Statistical, Nonlinear, and Soft Matter Physics*, *80*(1), 1–6 (2009).

92 Gao, L., Tahir, M. A., Virgin, L. N., & Yellen, B. B. Multiplexing superparamagnetic beads driven by multi-frequency ratchets. *Lab Chip*, *11*(24), 4214–4220 (2011).

93 Nicola A. Spaldin, Magnetic Materials: Fundamentals and device applications, (Cambridge university press, 2003)

94 O'Handley, R.C. Modern magnetic materials: principles and applications. (John Wiley & Sons, Inc., 2000).

95 Abo, G. S., Hong, Y. K., Park, J., Lee, J., Lee, W., & Choi, B. C. Definition of magnetic exchange length. *IEEE Transactions on Magnetics*, *49*(8), 4937–4939 (2013).

96 Jiles D, Introduction to Magnetism and Magnetic Materials (London: Chapman and Hall) (1991)

97 Weiss, P. La variation du ferromagnétisme avec la température. *Comptes Rendus*, *143*, 1136 (1906).

98 Williams, H. J., Bozorth, R. M., & Shockley, W. Magnetic domain patterns on single crystals of silicon iron. *Physical Review*, *75*(1), 155–178 (1949).

99 Zhang, S., & Li, Z. Roles of nonequilibrium conduction electrons on the magnetization dynamics of ferromagnets. *Physical Review Letters*, *93*(12), 127204 (2004).

100 Den Broeder, F. J. A., Kuiper, D., Van De Mosselaer, A. P., & Hoving, W. Perpendicular magnetic anisotropy of Co-Au multilayers induced by interface sharpening. *Physical Review Letters*, *60*(26), 2769–2772 (1988).

101 Carcia, P. F., Meinhaldt, A. D., & Suna, A. Perpendicular magnetic anisotropy in Pd/Co thin film layered structures. *Applied Physics Letters*, *47*(2), 178–180 (1985).

102 Carcia, P. F. Perpendicular magnetic anisotropy in Pd/Co and Pt/Co thin-film layered structures. *Journal of Applied Physics*, *63*(10), 5066–5073 (1988).

103 den Broeder, F. J. A., Kuiper, D., Donkersloot, H. C., & Hoving, W. A comparison of the magnetic anisotropy of [001] and [111] oriented Co/Pd Multilayers. *Applied Physics A Solids and Surfaces*, *49*(5), 507–512 (1989).

104 Ikeda, S., Miura, K., Yamamoto, H., Mizunuma, K., Gan, H. D., Endo, M., Kanai, S., Hayakawa, J., Matsukura, F., Ohno, H. A perpendicular-anisotropy CoFeB–MgO magnetic tunnel junction. *Nature Materials*, *9*(9), 721–724 (2010).

105 Baldrati, L., Tan, A. J., Mann, M., Bertacco, R., & Beach, G. S. D. Magneto-ionic effect in CoFeB thin films with in-plane and perpendicular-to-plane magnetic anisotropy. *Applied Physics Letters*, *110*(1), 12404 (2017).

106 Greaves, S. J., Petford-Long, A. K., Kim, Y. H., Pollard, R. J., Grundy, P. J., & Jakubovics, J. P. A magnetic and high resolution structural investigation of Pt/Co multilayers. *Journal of Magnetism and Magnetic Materials*, *113*(1–3), 63–71 (1992).

107 Draaisma, H. J. G., de Jonge, W. J. M., & den Broeder, F. J. A. Magnetic interface anisotropy in Pd/Co and Pd/Fe multilayers. *Journal of Magnetism and Magnetic Materials*, *66*(3), 351–355 (1987).

108 Johnson, M. T., Bloemen, P. J. H., Broeder, F. J. a Den, & Vries, J. J. De. Magnetic anisotropy in metallic multilayers. *Reports on Progress in Physics*, *59*(11), 1409–1458 (1999).

109 Louis, N. Anisotropie magnetique superficielle et surstuctures d'orientation. *J. Phys.* 225–239 (1954).

110 Nakajima, N., Koide, T., Shidara, T., Miyauchi, H., Fukutani, H., Fujimori, A., Iio, K., Katayama, T., Nyvlt, M., Suzuki, Y. Perpendicular Magnetic Anisotropy Caused by Interfacial Hybridization via Enhanced Orbital Moment in Co/Pt Multilayers: Magnetic Circular X-Ray Dichroism Study. *Physical Review Letters*, *81*(23), 5229–5232 (1998).

111 Hashimoto, S., Ochiai, Y., & Aso, K. Perpendicular magnetic anisotropy and magnetostriction of sputtered Co/Pd and Co/Pt multilayered films. *Journal of Applied Physics*, *66*(10), 4909–4916 (1989).

112 Huang, J. C. A., Lee, C. H., & Yu, K. L. Structure and magnetism in Co/Pt multilayers. *Journal of Applied Physics*, *89*(11 II), 7059–7061 (2001).

113 Weller, D., Folks, L., Best, M., Fullerton, E. E., Terris, B. D., Kusinski, G. J., Krishnan, K. M., Thomas, G. Growth, structural, and magnetic properties of high coercivity Co/Pt multilayers. *Journal of Applied Physics*, *89*(11 II), 7525–7527 (2001).

114 Sbiaa, R., Meng, H., & Piramanayagam, S. N. Materials with perpendicular magnetic anisotropy for magnetic random access memory. *Physica Status Solidi (B)*, *5*(12), 413–419 (2011).

115 Emori, S., Bono, D. C., & Beach, G. S. D. Time-resolved measurements of field-driven domain wall motion in a submicron strip with perpendicular magnetic anisotropy. *Journal of Applied Physics*, *111*(7), 7–10 (2012).

116 Judy, J. H. Advancements in PMR thin-film media. *Journal of Magnetism and Magnetic Materials*, *287*(SPEC. ISS.), 16–26 (2005).

117 Safarik, I., & Safarikova, M. Magnetic techniques for the isolation and purification of proteins and peptides. *Biomagnetic Research and Technology*, *2*(1), 7 (2004).

118 Natalie A. Frey, Sheng Peng, Kai Cheng, and S. S. Magnetic nanoparticles: synthesis, functionalization, and applications in bioimaging and magnetic energy storage. *Chem. Soc. Rev.*, *38*(9), 2532–2542 (2009).

119 Gijs, M. A. M., Lacharme, F., & Lehmann, U. Microfluidic applications of magnetic particles for biological analysis and catalysis. *Chemical Reviews*, *110*(3), 1518–1563 (2010).

120 Ruffert, C. Magnetic bead-magic bullet. *Micromachines*, *7*(2) (2016).

121 Thanh, N. T. Magnetic Nanoparticles from Fabrication to Clinical Applications. *CRC Press*, 243–276 (2012).

122 Pamme, N. Magnetism and microfluidics. *Lab on a Chip*, *6*(1), 24–38 (2006).

123 Zhang, L., Qiao, S., Jin, Y., Yang, H., Budihartono, S., Stahr, F., Yan, Z., Wang, X., Hao, Z., Lu, G. Q. Fabrication and size-selective bioseparation of magnetic silica nanospheres with highly ordered periodic mesostructure. *Advanced Functional Materials*, *18*(20), 3203–3212 (2008).

124 Na, H. Bin, Song, I. C., & Hyeon, T. Inorganic nanoparticles for MRI contrast agents. *Advanced Materials*, *21*(21), 2133–2148 (2009).

125 Young, A. G., McQuillan, A. J., & Green, D. P. In situ IR spectroscopic studies of the avidin-biotin bioconjugation reaction on CdS particle films. *Langmuir*, *25*(13), 7416–7423 (2009).

126 Jordan, A., Scholz, R., Maier-Hauff, K., Johannsen, M., Wust, P., Nadobny, J., Schirra, H., Schmidt, H., Deger, S., Loening, S., Lanksch, W., Felix, R. Presentation of a new magnetic field

therapy system for the treatment of human solid tumors with magnetic fluid hyperthermia. *Journal of Magnetism and Magnetic Materials*, *225*(1–2), 118–126 (2001).

127 Papaefthymiou, G. C. Nanoparticle magnetism. *Nano Today*, *4*(5), 438–447 (2009).

128 L. Néel, Ann. Geophys. 5, 99 (1949); L. Néel, J. Phys. Radium 20, 215 (1959)

129 Brown, W. F. Thermal fluctuations of a single-domain particle. *Physical Review*, *130*(5), 1677–1686 (1963).

130 Aharoni, A. Thermal agitation of single domain particles. *Physical Review*, *135*(2A) (1964).

131 Young H. Freedman R University physics, 9th edition. Addison-Wesley Publishing Company, Reading. ISBN 0- 201-31132-1 (1996)

132 Jackson J. *Classical electrodynamics*, 3rd edition. Wiley, New York. ISBN 0-471-30932 (1998)

133 Sommerfeld, A. Ein beitrag zur hydrodynamischen erklaerung der turbulenten fluessigkeitsbewegungen. *Proceedings of the 4th International Congress of Mathematicians III*, *174*(1883), 116–124 (1908).

134 White FM, Fluid mechanics, 4th edition. McGraw-Hill, New York (1999)

135 Jones, T.B., *Electromechanisc of Particles,* Cambridge University Press, Cambridge (1995)

136 Derks, R. J. S., Dietzel, A., Wimberger-Friedl, R., & Prins, M. W. J. Magnetic bead manipulation in a sub-microliter fluid volume applicable for biosensing. *Microfluidics and Nanofluidics*, *3*(2), 141–149 (2007).

137 Liuliesbet, C., & Borghs, L. W. On-chip separation of magnetic particles with different magnetophoretic mobilities, *J. Appl. Phys. 101*, 024913. (2007).

138 Sing, C. E., Schmid, L., Schneider, M. F., Franke, T., & Alexander-Katz, A. Controlled surface-induced flows from the motion of self-assembled colloidal walkers. *Proceedings of the National Academy of Sciences of the United States of America*, *107*(2), 535–540 (2010).

139 Weddemann, A., Wittbracht, F., Eickenberg, B., & Hütten, A. Magnetic field induced assembly of highly ordered two-dimensional particle arrays. *Langmuir*, *26*(24), 19225–19229 (2010).

140 Petousis, I., Homburg, E., Derks, R., & Dietzel, A. Transient behavior of magnetic micro-bead chains rotating in a fluid by external fields. *Lab on a Chip*, *7*(12), 1746–1751 (2007).

141 Vieira, G., Henighan, T., Chen, A., Hauser, A. J., Yang, F. Y., Chalmers, J. J., & Sooryakumar, R. Magnetic Wire Traps and Programmable Manipulation of Biological Cells. *Physical Review Letters*, *103*(12), 16–19 (2009).

142 Bryan, M. T., Dean, J., Schrefl, T., Thompson, F. E., Haycock, J., & Allwood, D. A. The effect of trapping superparamagnetic beads on domain wall motion. *Applied Physics Letters*, *96*(19) (2010).

143 M.J. Donahue, D.G. Porter, OOMMF user's guide, version 1.0. Interagency Report NISTIR 6376, National Institute of Standards and Technology, Gaithersburg, MD, (1999)

144 Vansteenkiste, A., & De Wiele, B. Van. MUMAX: A new high-performance micromagnetic simulation tool. *Journal of Magnetism and Magnetic Materials*, *323*(21), 2585–2591 (2011).

145 Heyderman, L. J., Nolting, F., Backes, D., & Czekaj, S. Magnetization reversal in cobalt antidot arrays, *73,* 1–12 (2006).

146 Abert, C., Exl, L., Selke, G., Drews, A., & Schrefl, T. Numerical methods for the stray-field calculation: A comparison of recently developed algorithms. *Journal of Magnetism and Magnetic Materials*, *326*, 176–185 (2013).

147 Amazon Web Services, http://aws.amazon.com/.

148 J.C. Hulteen, Nanosphere lithography: A materials general fabrication process for periodic particle array surfaces, *J. Vac. Sci. Technol. A Vacuum, Surfaces, Film. 13* 1553 (1995).

149 A. A. Zhukov, A. V. Goncharov, P.N. Bartlett, M. A. Ghanem, Magnetic antidot arrays from self-assembly template methods, J. Appl. Phys., *93* 2003–2005 (2003).

150 C.C. Ho, T.W. Hsieh, H.H. Kung, W.T. Juan, K.H. Lin, W.L. Lee, Reduced saturation magnetization in cobalt antidot thin films prepared by polyethylene oxide-assisted self-assembly of polystyrene nanospheres, *Appl. Phys. Lett. 96* 3–5 (2010).

151 J. Kim, J. Kim, S.G. Cho, Y.H. Choa, G.J. Shin, Microstructures and the corresponding magnetic properties of antidot arrays, *Thin Solid Films. 520* 3013–3016 (2012).

152 X. Ye, L. Qi, Two-dimensionally patterned nanostructures based on monolayer colloidal crystals: Controllable fabrication, assembly, and applications, *Nano Today. 6* (2011) 608–631.

153 F. Burmeister, C. Schäfle, T. Matthes, M. Böhmisch, J. Boneberg, P. Leiderer, Colloid Monolayers as Versatile Lithographic Masks, *Langmuir. 13* 2983–2987 (1997).

154 Z. Tian, B. Ren, D. Wu, Nanosphere Lithography: A versatile Nanofabrication Tool for Studies of Size-Dependent Nanoparticle Optics, *J. Phys. Chem. B, 105* 5599–5611 (2001).

155 K. Nagayama, Two-dimensional self-assembly of colloids in thin liquid films, *Colloids Surfaces A: Physicochem. Eng. Aspects 109* (1996) 363-374

156 Elizabeth Rapoport, Magnetic domain walls for on-chip transport and detection of superparamagnetic beads, Massachusetts Institute of Technology, Cambridge, Massachusetts.

157 Gao, L., Tahir, M. A., Virgin, L. N., & Yellen, B. B. Multiplexing superparamagnetic beads driven by multi-frequency ratchets. *Lab Chip*, *11*(24), 4214–4220 (2011).

158 Vavassori, P., Metlushko, V., Osgood, R., Grimsditch, M., Welp, U., Crabtree, G., Fan, W., Brueck, S.R.J., Ilic, B., Hesketh, P. Magnetic information in the light diffracted by a negative dot array of Fe. *Physical Review B*, *59*(9), 6337–6343 (1999).

159 Wang, C. C., Adeyeye, A. O., & Singh, N. Magnetic antidot nanostructures: effect of lattice geometry. *Nanotechnology*, *17*(6), 1629 (2006).

160 Yu, C. T., Jiang, H., Shen, L., Flanders, P. J., & Mankey, G. J. The magnetic anisotropy and domain structure of permalloy antidot arrays. *Journal of Applied Physics*, *87*(9), 6322 (2000).

161 Welp, U., Vlasko-Vlasov, V. K., Crabtree, G. W., Thompson, C., Metlushko, V., & Ilic, B. Magnetic domain formation in perforated permalloy films. *Applied Physics Letters*, *79*(9), 1315–1317 (2001).

162 Vavassori, P., Gubbiotti, G., Zangari, G., Yu, C. T., Yin, H., Jiang, H., & Mankey, G. J. Lattice symmetry and magnetization reversal in micron-size antidot arrays in Permalloy film. *Journal of Applied Physics*, *91*(10 I), 7992–7994 (2002).

163 Piramanayagam, S. N., Ranjbar, M., Tan, H. K., Allen Poh, W. C., Sbiaa, R., & Chong, T. C. Magnetic properties of antiferromagnetically coupled antidots of Co/Pd multilayers. *Journal of Applied Physics*, *111*(7), 113–116 (2012).

164 Melle, S., & Martin, J. E. Chain model of a magnetorheological suspension in a rotating field. Journal of Chemical Physics, 118(21), 9875–9881 (2003).

165 Li, Y. H., Chen, C. Y., Sheu, S. T., & Pai, J. M. Dynamics of a microchain of superparamagnetic beads in an oscillating field. Microfluidics and Nanofluidics, 13(4), 579–588 (2012).

166 Sing, C. E., Schmid, L., Schneider, M. F., Franke, T., & Alexander-Katz, A. Controlled surface-induced flows from the motion of self-assembled colloidal walkers. Proceedings of the National Academy of Sciences of the United States of America, 107(2), 535–540 (2010).

167 Karle, M., Wöhrle, J., Miwa, J., Paust, N., Roth, G., Zengerle, R., & Von Stetten, F. Controlled counter-flow motion of magnetic bead chains rolling along microchannels. Microfluidics and Nanofluidics, 10(4), 935–939 (2011).